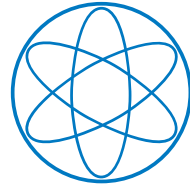


PHYSIK - DEPARTMENT



Optical Beam Diagnostics for  
High Intensity Heavy Ion  
Beams

DISSERTATION

VON

RAPHAEL HAMPF



TECHNISCHE UNIVERSITÄT  
MÜNCHEN



TECHNISCHE UNIVERSITÄT MÜNCHEN  
Fakultät für Physik

# Optical Beam Diagnostics for High Intensity Heavy Ion Beams

Raphael Hampf

Vollständiger Abdruck der von der Fakultät für Physik der Technischen Universität München zur Erlangung eines

Doktors der Naturwissenschaften (Dr. rer. nat.)

genehmigten Dissertation.

Vorsitzender: Prof. Dr. Alejandro Ibarra

Prüfer der Dissertation:

1. apl. Prof. Dr. Andreas Ulrich
2. Prof. Dr. Reinhard Kienberger

Die Dissertation wurde am 28.09.2020 bei der Technischen Universität München eingereicht und durch die Fakultät für Physik am 18.03.2021 angenommen.



## Abstract

Particle accelerators are used in a wide range of applications in fundamental research, technology, and medical science and therapy. They transport particles from a source to a so-called target. The transport is accomplished via a beam guiding system. This works analog to beam guidance in optical imaging with lenses. In the case of particle accelerators these lenses act via electric and magnetic fields deflecting the particles and focusing the beam. In order to achieve the desired redirection as well as the focusing of the beam it is critical to know the position and profile of the beam. This knowledge is gained by beam profile measurements. So far, wires, grids, and scintillators are used for beam profile measurements. However, these methods interfere with the beam and can have destructive effects for the beam profile monitors. Due to the trend of using higher beam currents and better focusing those conventional beam profile measurements are getting increasingly problematic. An alternative to these invasive methods is optical beam profile diagnostics. For optical beam diagnostics a suitable target gas is led into the beamline in certain locations. The light emission in the gas is then detected by a camera. This way the location and focusing of the beam can be observed with negligible influence on the beam.

In accelerator experiments a great variety of projectiles is used. This work has been performed in a research group which has studied the light emission induced by particle excitation for a very long time. During this time a collaboration with the Helmholtz Centre for Heavy Ion Research (GSI) in Darmstadt was established.

Here, exemplary studies of ion-beam profile diagnostics are presented. The experiments were performed with intermediate beam currents and particle energies rather than high energies and currents. The light emission from gas targets induced by heavy ion beams was first observed at almost atmospheric pressures and then also down to very low target gas densities.

The experiments described were conducted at the Munich Tandem van de Graaff accelerator in Garching near Munich, Germany. Mainly, a sulfur ion beam ( $^{32}\text{S}$ ) with a particle energy of 87MeV was used. Further experiments were performed with a proton beam of 14MeV particle energy. Goal of the experiments was the identification of suitable target materials and optical transitions for beam diagnostics. Therefore, spectral studies were performed, as well as exemplary beam profile measurements with three different cameras. The images recorded by the camera systems were used to analyze the beam profiles and to determine effective emission cross-sections. The sensitivity of the cameras was measured in off-line experiments for that purpose.

The results are discussed with particular focus on the mechanisms of light

emission. An important issue is the influence of secondary electrons on the results for both the spectra and the beam profiles. Secondary electrons were also simulated using an electron gun in a separate experiment. In previous studies of the research group it had been predicted that optical transitions of neutral target atoms are excited in single collisions both by heavy ions as well as electrons. In comparison to that, single collisions by electrons rarely lead to ionization combined with immediate excitation. However, this is possible for single collisions with heavy ions. This phenomenon allows to distinguish between light emission induced by secondary electrons and light emission induced by heavy ions.

Optical transmissions were studied both in rare gases, mainly neon and argon, as well as in nitrogen. Suitable lines for beam profile measurements were identified (Ar I: 738.40nm, Ar II: 476.49nm, Ne I: 585.25nm, Ne II: 337.82nm). The intensities of a selection of spectral lines was analyzed over a wide pressure range. At higher pressures ( 100mbar) the light emission from optical transitions of neutral atoms appeared with several orders of magnitude higher intensity than those of ionized target species. This changed towards lower pressures, where the intensities became comparable.

The spectral measurements were recorded using a vacuum spectrometer ( $f = 30\text{cm}$ ), which can be used for wavelengths from 120nm up to the near infrared region. A wavelength resolution of up to 0.06nm was achieved. Light collection was accomplished via mirror optics.

The exemplary beam profile measurements were performed using three different cameras, a pure CCD camera, a CCD camera with an image intensifier (iCCD) and an electron-multiplying CCD camera (EMCCD). The target gas pressure was varied over almost 8 orders of magnitude (between 300mbar and  $10^{-5}\text{mbar}$ ). At pressures above 1mbar the target chamber was separated from the beamline by a titanium entrance foil and the target gas was purified in a purification circuit. Below 1mbar no separation foil was used and differential pumping was used between the beamline and the target cell. Absolute calibration of the camera systems allowed to determine absolute emission rates from the images recorded. Effective emission cross-sections were calculated from these absolute emission rates. For argon and neon excited by a sulfur ion beam the effective emission cross-sections are in the range between  $10^{-18}\text{cm}^2$  and  $10^{-16}\text{cm}^2$ , for nitrogen between  $8 \cdot 10^{-19}\text{cm}^2$  and  $2 \cdot 10^{-16}\text{cm}^2$ . For the excitation in neon by a proton beam, cross-sections around  $10^{-21}\text{cm}^2$  were measured. The results of this works should help to evaluate the possibilities for optical beam diagnostics for different experimental situations. The measured effective emission cross-sections can help to scale photon emission rates, and thereby exposure times, to different target gas pressures, beam currents, camera systems and different projectiles

and particles energies.



## Zusammenfassung

Teilchenbeschleuniger finden vielfache Verwendung, sowohl in der Grundlagenforschung, als auch in Anwendungen in Technik und Medizin. Ein Teilchenbeschleuniger transportiert Teilchen von einer Quelle zu einem sogenannten Target. Der Transport der Teilchen wird durch ein Strahlführungssystem gewährleistet, welches analog zur Strahlführung in der Optik mithilfe von Linsen funktioniert. Im Falle von Teilchenbeschleunigern wirken diese Linsen durch elektrische und magnetische Felder und lenken so die geladenen Teilchen ab oder fokussieren den Strahl aus Teilchen. Um die gewünschte Ablenkung, sowie auch die benötigte Fokussierung des Strahles zu erreichen, ist es wichtig das Strahlprofil an bestimmten Stellen zu kennen. Diese Kontrolle des Strahles wird durch Strahlprofilmessungen ermöglicht. Bisher erfolgte die Strahlprofilmessung hauptsächlich mit Drähten, Gittern und Szintillatoren. Diese Methoden interferieren jedoch mit dem Strahl. Aufgrund immer höherer Strahlströme werden Strahlprofilmessungen mit konventionellen Methoden zunehmend problematisch, da sie nicht zerstörungsfrei ablaufen. Eine Alternative zu diesen invasiven Methoden ist die optische Strahlprofilmessung. Hierbei werden geeignete Gase an bestimmten Stellen in das Strahlrohr geleitet und mit einer Kamera wird die Lichtemission im Gas detektiert. So kann beobachtet werden wo sich der Strahl befindet und wie dieser fokussiert ist.

An Teilchenbeschleunigern gibt es eine Vielzahl an möglichen Projektilen, von Elektronen bis hin zu hochenergetischen Schwerionen. Die hier beschriebene Arbeit entstand im Rahmen einer Arbeitsgruppe, die schon lange Zeit die Lichtemission bei Schwerionenstrahlanregung studiert. Dabei entstand auch eine langjährige Zusammenarbeit mit dem GSI Helmholtzzentrum für Schwerionenforschung in Darmstadt.

In dieser Arbeit werden exemplarische Studien zur Strahlprofilmessung präsentiert. Die Experimente wurden nicht mit hohen Strömen oder Energien durchgeführt, sondern bei mittleren Strahlströmen und Teilchenenergien. Die Lichtemission von Gastargets angeregt durch Schwerionenstrahlen wurde bei fast atmosphärischen Drucken bis hin zu niedrigen Gastargetdichten beobachtet.

Die Experimente im Rahmen dieser Arbeit fanden am Tandem-van de Graaff Beschleuniger des Maier-Leibnitz-Laboratorium in Garching statt. Verwendet wurde hauptsächlich ein Schwefelstrahl (32S) mit einer Teilchenenergie von 87MeV. Überdies wurde ein Experiment mit Protonen als Projektil (14MeV) durchgeführt. Zielsetzung ist es geeignete Targetmaterialien und geeignete optische Übergänge für die Strahldiagnose zu finden. Hierzu wurden im Rahmen dieser Arbeit spektrale Studien durchgeführt. Weit-

erhin wurden exemplarische Strahlprofilmessungen mit drei verschiedenen Kameras ausgeführt, um Strahlprofile auszuwerten und effektive Emissionswirkungsquerschnitte bestimmen zu können.

Die Ergebnisse werden im Hinblick auf die Mechanismen der Lichtemission diskutiert. Ein wichtiges hierbei auftretendes Problem sind Sekundärelektronen. Diese wurden in getrennten Experimenten mit einer Elektronenkanone (12keV) simuliert und studiert. In vorausgegangenen Arbeiten der Gruppe wurde vorhergesagt, dass optische Übergänge neutraler Targetatome im Einzelstoß sowohl von Schwerionen als auch von Elektronen angeregt werden. Im Vergleich dazu kommt es kaum zu Ionisation und sofortiger Anregung im Einzelstoß durch Elektronen. Dies ist jedoch durch Schwerionen möglich. Dieses Phänomen lässt zwischen Lichtemission induziert durch Sekundärelektronen und Lichtemission induziert durch Schwerionen unterscheiden.

Studiert wurden optische Übergänge sowohl in Edelgasen, hauptsächlich Neon und Argon, sowohl als auch in Stickstoff. Dabei wurden für die Strahlprofilmessungen geeignete Linien identifiziert (Ar I: 738.40nm, Ar II: 476.49nm, Ne I: 585.25nm, Ne II: 337.82nm). Die Intensitäten ausgewählter Spektrallinien wurden über einen weiten Druckbereich analysiert. Hierbei zeigte sich, dass bei höheren Drucken (100mbar) die Lichtemission aus optischen Übergängen neutraler Targetatome in der Intensität mehrere Größenordnungen über den optischen Übergängen ionisierter Targetteilchen liegt. Dies ändert sich hin zu niedrigen Drucken, bei denen sich die Intensitäten angleichen. Die spektralen Messungen wurden mit einem Vakuumspektrometer ( $f=30\text{cm}$ ) durchgeführt, welches für Wellenlängen von 120nm bis hin ins nahe Infrarot ausgelegt ist und Auflösungen von 0.06nm ermöglicht. Die Abbildung der Lichtemission erfolgte über eine Spiegeloptik.

Die exemplarischen Strahlprofilmessungen erfolgten mit drei verschiedenen Kameras, einer reinen CCD-Kamera, einer CCD-Kamera mit Bildverstärker (iCCD) und einer Elektronenmultiplizierten CCD-Kamera (EMCCD) und wurden über einen weiten Druckbereich (300mbar bis  $10^{-5}\text{mbar}$ ) durchgeführt. Bei Drucken höher als 1mbar wurde die Targetzelle durch eine Titanfolie vom Strahlrohr getrennt und das Targetgas durch die einen Reinigungskreislauf ständig gereinigt. Bei Drucken niedriger als 1mbar wurde die Eintrittsfolie entfernt und gereinigtes Gas durch differentielles Pumpen durch die Targetzelle geleitet und im Strahlrohr abgepumpt.

Die Messung der absoluten Emissionsraten wurde durch Absolutkalibrierung der verwendeten Kamerasysteme ermöglicht. Aus den absoluten Emissionsraten, die aus den Bildaufnahmen erhalten wurden, konnten effektive Emissionswirkungsquerschnitte berechnet werden. Für Argon und Neon bei Anregung mit einem Schwefelstrahl liegen die effektiven Emissionswirkungsquer-

schnitte zwischen  $10^{-17} \text{cm}^2$  und  $10^{-16} \text{cm}^2$ , bei Stickstoff zwischen  $10^{-18} \text{cm}^2$  und  $6 \cdot 10^{-16} \text{cm}^2$ . Für die Anregung in Neon durch einen Protonenstrahl wurden Wirkungsquerschnitte im Bereich  $10^{-21} \text{cm}^2$  gemessen.

Die Ergebnisse dieser Arbeit sollen dabei helfen die Möglichkeiten der optischen Strahldiagnostik für verschiedene Beschleunigerexperimente zu evaluieren. Mithilfe der gemessenen effektiven Emissionswirkungsquerschnitten können Photonenemissionsraten und damit Belichtungszeiten zu verschiedenen Gasdrücken, Strahlströmen, Kamerasystemen und sogar anderen Strahlarten und Teilchenenergien des Strahls skaliert werden.



# Contents

<b>1</b>	<b>Introduction</b>	<b>1</b>
<b>2</b>	<b>Experimental setup</b>	<b>5</b>
2.1	Tandem Van-de-Graaff accelerator . . . . .	5
2.2	Target chamber . . . . .	8
2.3	Gas system . . . . .	8
2.4	Impurities . . . . .	12
2.5	Spectroscopic setup . . . . .	12
2.5.1	Mirror optics box . . . . .	13
2.5.2	Monochromator . . . . .	13
2.5.3	Photomultiplier tube and photon counting (PMT) . . .	15
2.6	Beam profile monitors . . . . .	16
2.6.1	ATIK 383L+ . . . . .	16
2.6.2	PI-Max4 1024f . . . . .	16
2.6.3	Pro EM+ 512 B . . . . .	17
2.6.4	Calibration of the cameras . . . . .	18
2.6.5	Spatial resolution of the camera systems . . . . .	23
2.6.6	Objective lens . . . . .	26
2.6.7	Bandpass filters . . . . .	28
2.7	Electron gun . . . . .	31
<b>3</b>	<b>Results</b>	<b>35</b>
3.1	Spectroscopic results . . . . .	35
3.1.1	Spectroscopic results with heavy ion beam excitation .	38
3.1.2	Spectroscopic results with electron beam excitation . .	51
3.1.3	Choice of bandpass filters . . . . .	59
3.2	Time resolved measurements . . . . .	59
3.3	Beam profiles . . . . .	60
3.4	Effective emission cross-sections in argon and neon . . . . .	70
3.4.1	Charge state of the ion projectiles . . . . .	71
3.4.2	Region of interest and image processing . . . . .	71

3.4.3	Absolute light intensity measurement . . . . .	73
3.4.4	Calculated effective emission cross-section . . . . .	76
3.4.5	Effective emission cross-sections in nitrogen . . . . .	80
3.5	Effective emission cross-sections with a proton beam . . . . .	82
<b>4</b>	<b>Conclusion</b>	<b>85</b>
<b>A</b>	<b>Energy loss in the Ti-foil and the target gas</b>	<b>89</b>

# Chapter 1

## Introduction

The goal of optical beam profile measurements is to determine the intensity distribution of the particle flux in a particle beam. This can be necessary to optimize focusing of the beam. The optical determination of the beam profile is achieved by exciting gas atoms by a particle beam and detecting the induced light emission spatially resolved. Particle beams from the Munich Tandem-van de Graaff accelerator were used for the excitation, mostly a sulfur ion beam of particle energies between 87MeV and 100MeV. Spectroscopic studies served to identify proper target gases and optical transitions, that are suited for beam diagnostics.

A specific goal of these studies is to develop techniques for determining beam profiles of very intense ion beams. The motivation for purely optical beam profile measurements is based on the fact, that alternative beam profile monitors such as solid-state scintillators, grids or wires would be destroyed by the beam. The optical beam profile measurement uses a gas target which is observed by appropriate camera systems. Various experimental studies have already been performed in that direction [1] [2] [3] [4] [5] [6] [7]. Optical systems and detectors for beam profile measurements and their application over a wide pressure range ( $10^{-5}mbar < p < 10^3mbar$ ) were therefore tested. The detector systems were absolutely calibrated in order to determine the absolute light emission and thus the emission cross-sections from the images taken of the beam [8]

One of several possible applications of these studies relating to the collaboration partners at GSI/FAIR is the High Luminosity (HL) upgrade of the Large Hadron Collider (LHC). The luminosity is a measure of the number of expected events in dependence of the collision cross-section and therefore a critical parameter of accelerator experiments. A high luminosity is desired.

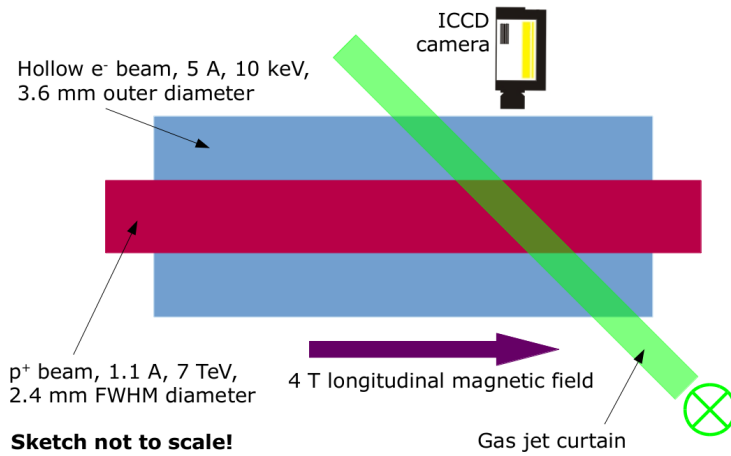


Figure 1.1: Schematic drawing of the e-lens collimator featuring an iCCD camera as beam profile monitor. Figure taken from [10]

The HL upgrade is a project, to increase its instantaneous luminosity (rate of collisions) by a factor of 5 and the integrated luminosity (total collisions) by a factor of 10. [9]

One part of this upgrade is the development of a collimator for the ion beam in form of a hollow electron beam, a so-called "hollow electron lens system" (e-Lens) [10] [11]. The hollow electron beam is laid around the ion beam as can be seen in Figure 1.1. Ions that are too far from the beam axis are either removed from the beam by collisions with the electrons or directed back into the bulk of the beam. In order to achieve the desired collimation, both the high-energetic ion beam and the low-energy electron beam have to be aligned with great accuracy. Therefore a beam profile monitor is necessary, which on the one hand is not destroyed by the beam and on the other hand does not interfere with it. Thus, an optical beam profile monitor is best suited for the task. In order to make the ion beam visible in ultra-high vacuum ( $10^{-9}$ mbar), a gasjet is sent transversely from one side through the beam line and is pumped away on the other side. It crosses both the hollow electron beam and the ion beam. Light emission is induced by the collisions of the ions with the gas particles and can be detected by the beam profile monitor.

Fundamental studies about optical beam profile measurements are performed in this study. A critical question is the distinction between electron and ion beam as can be seen from the example discussed above. Furthermore an ion beam produces secondary electrons through collisions with the atoms of the target gas. This modifies the visible form of the actual beam and can make it appear widened. It has to be studied under which circumstances this widen-

ing appears and what role the target gas pressure plays. It is predicted in [12] that electrons almost exclusively excite neutral target gas atoms, which is a possibility to locate the actual beam by looking at emission lines from transitions from ionized target gases. This has to be tested as well.

Studies were performed using different target gases that are possibly suitable for applications in accelerator experiments. The possibilities of a beam profile monitor shall be tested, for example if the spatial resolution is sufficient and if the necessary exposure times are short enough for real time applications like the alignment.

The knowledge of the spectral emission lines of the different target gases and their behavior with varying pressure is important since some spectral lines almost completely disappear at low pressures. Furthermore, it is critical to know which transitions are more likely to be excited by secondary electrons and which ones almost exclusively by ion projectiles. This allows to select the preferable emission lines for the later monitoring of the beam with an optical beam profile monitor.

The calculation of effective emission cross-sections from the data obtained from imaging the beam helps to design beam profile monitors for various accelerator and beam parameters.



# Chapter 2

## Experimental setup

A heavy ion beam from the Munich Tandem accelerator is sent into a target chamber filled with a rare gas or nitrogen. The heavy ions lead to excitation of the target gas, which then leads to light emission in various emission lines. The intensity of these emission lines is studied for different pressures. First optical spectroscopy is performed with a spectroscopic setup consisting of a mirror optics box, a monochromator and a photomultiplier tube. Furthermore optical images are recorded with three different camera systems using various wavelength filters. Gas pressure is controlled by highly accurate dosing valves and several measuring devices. A gas purifier was used to work with perfectly clean rare gases. Differential pumping was performed for pressures below 1mbar.

The target chamber is shown in Figure 2.1 with one of the cameras (ATIK 383L+) mounted in the front. Images are recorded through the fused silica front window. Opposite to the fused silica front window is a  $MgF_2$ -window leading to the spectroscopic setup visible in Figure 2.2.

### 2.1 Tandem Van-de-Graaff accelerator

Light emission was induced by a heavy ion beam accelerated by the Tandem-van de Graaff accelerator at the Maier-Leibnitz-Laboratorium (MLL) in Garching. A portrait of the laboratory was published by Günther Dollinger and Thomas Faestermann in April 2018 [14]. In most experiments described here a dc-beam of  $^{32}\text{S}$  ions was used. The particle energy was chosen between 87MeV and 100MeV. For target gas pressures of 1mbar and higher the beam entered the target chamber through a  $1.1\text{mg}/\text{cm}^2$  titanium-foil. By passing through this foil the ions loose 13MeV and have an energy of 87MeV when reaching into the target gas. In the case of an energy of 87MeV of the incid-

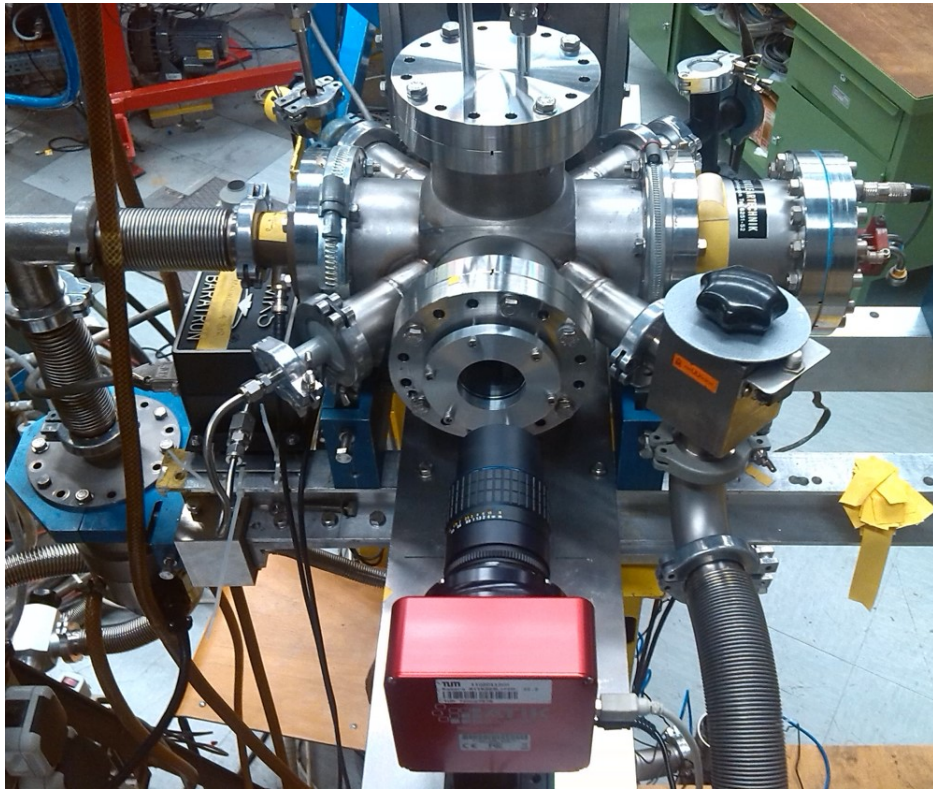


Figure 2.1: Target chamber with ATIK camera mounted in front. The heavy ion beam comes from the left hand side through the beam line. Several turbomolecular pumps are used for differential pumping. The “Baratron” capacitive pressure measuring device can be seen underneath the beamline (black box). The “endcup”, a faraday cup measuring the beam current is at the end of the beamline on the right hand side.

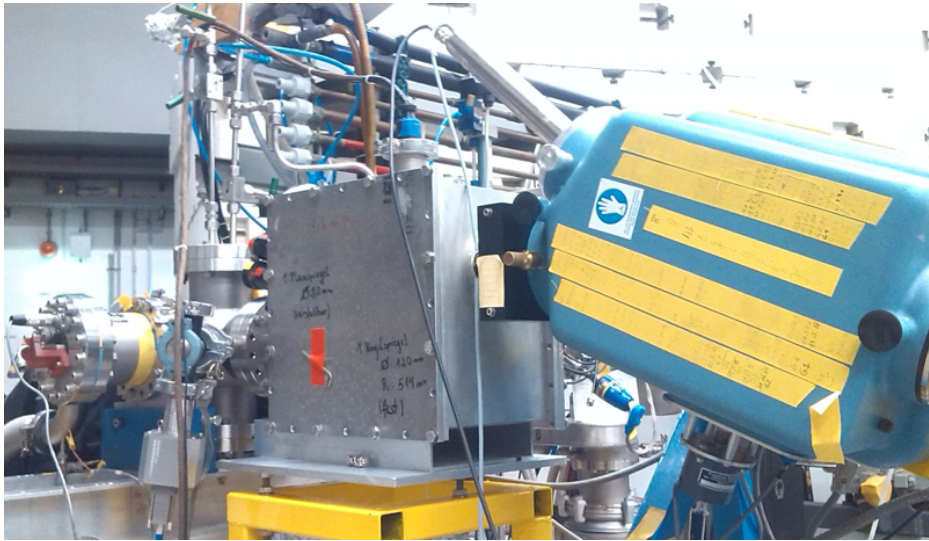


Figure 2.2: Spectroscopic setup consisting of a mirror optics box (metal box), a filter wheel (little black box between mirror optics boax and monochromator), a monochromator (in blue with yellow tape) and a PMT mounted at the exit slit of the monochromator.

ent ions the remaining energy behind the foil is calculated to 74MeV (Energy loss was calculated using reference [16]). Throughout this energy range from 74 to 100MeV the energy loss per unit length ( $dE/dx$ ) stays roughly constant for at least several centimeters behind the foil even in the extreme case of a pressure of 1000mbar (see Appendix A). During the experiments the pressure was always below this value. The width of the energy distribution is less than 50keV [15].

An advantage of the Tandem accelerator facility was the possibility to perform 10 beam times in only 2 years. A particle energy between 87MeV and 100MeV (2.7MeV/u and 3.1MeV/u resp.) is a good intermediate energy between highly energetic beams with GeV or even TeV energies and low energy experiments in the low MeV and keV range. Also the mainly used  $^{32}\text{S}$  ion beam has an intermediate projectile mass and allows scaling to different projectiles both in higher and lower mass regions.

Furthermore, in this accelerator various projectiles can be used, so that one beam time was performed with a proton beam with a particle energy of 14MeV.

## 2.2 Target chamber

The target chamber is schematically drawn in Figure 2.3. The ion beam enters the target chamber from the beamline through a cylindrical tube (“Nasenbär”, see Figure 2.3) with a mount for the titanium entrance foil at its end pointing towards the target chamber. Alternatively a disk with an aperture of 1.0mm diameter was mounted. At the opposite end towards the beamline a tantalum aperture with a 5mm hole was mounted. When the beam was unfocused or misaligned an electrical current was measured on that aperture.

The main part of the target chamber itself is a CF100 standard double-cross piece (diameter: 25cm) with a volume of roughly 10l. On the front side of the target chamber is a fused silica window through which photographs of the light emission can be taken. The fused silica window enables to detect light down to wavelengths of  $\sim 200\text{nm}$ . The camera with its objective lens and bandpass filters was mounted in front of the window. Background is reduced by covering the window, objective and front part of the camera with a black box.

On the opposite side of the chamber is a  $MgF_2$  window. Through this window the emitted light is focused by mirror optics into a grating monochromator and is detected by a photo multiplier tube (PMT).

The ion beam is stopped at the “Endcup”, a Faraday cup designed to measure the beam current. It has to be considered that the beam current measurement is only accurate at pressures below  $10^{-4}\text{mbar}$  and also that a suppression voltage has to be applied to keep secondary electrons from distorting the beam current measurement. At higher pressures several effects lead to a completely distorted measurement. Therefore the beam current measurements were performed at low pressures before and after each data taking.

## 2.3 Gas system

The gas system of the experiment serves to lead the gas through the target chamber and to circulate the gas. It was also modified in a way that enabled to regulate the pressure in the cell towards very low pressures ( $p = \sim 10^{-5}\text{mbar}$ ) by differential pumping. A schematic drawing is shown in Figure 2.4. The gases used in the experiment were mainly the rare gases neon and argon, which are most relevant for the studies. A few measurements were performed with krypton and xenon as well as with nitrogen for comparison. The target gas enters the purification circuit through a pressure regulator. A metal bellows pump (Ansyco MB-41E) circulates the gas through the circuit

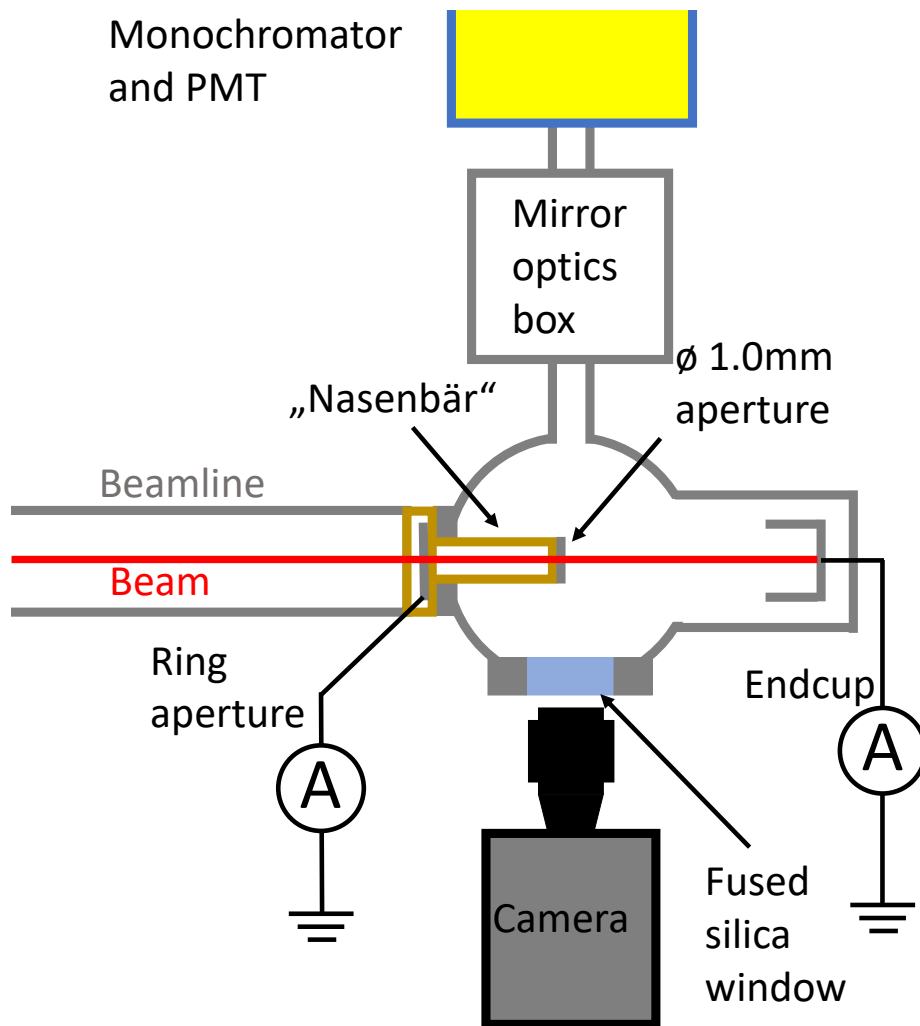


Figure 2.3: Schematic drawing of the target chamber. The ion beam enters the target chamber from the beamline through an aperture of 1.0mm diameter, alternatively through a titanium entrance foil. From the one side imaging of the light emission with a camera can be performed, from the other side wavelength spectra can be recorded with the spectroscopic setup (mirror optics box, monochromator and PMT). The electrical current of the beam is measured at the “Endcup”.

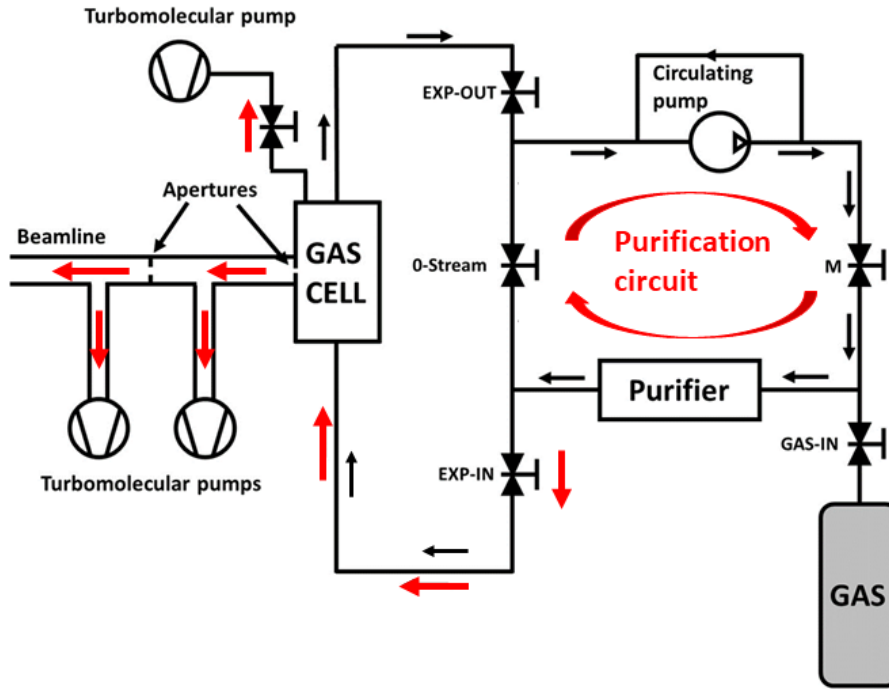


Figure 2.4: Schematic drawing of the gas system. The operation of the gas system is described in the text. The black arrows show the gas flux when the gas cell is separated from the beamline by the Ti entrance foil: the gas circulates through the gas cell and back to the purifier. The red arrows show the gas flux in the case of differential pumping: the gas circulates in the purification circuit. A small gas flux leaves this circuit and flows through the gas cell into the beamline where it is pumped by turbomolecular pumps.

and leads it through the rare gas purifier (Mono Torr PS4-MT3). The rare gas purifier reduces the abundance of impurities ( $H_2O$ ,  $CO$ ,  $CO_2$ ,  $CH_4$  and  $N_2$ ) to a few parts per billion [17]. The purification process can be visualized by recording the intensity of the  $OH^*$  emission versus time at  $\sim 300$ mbar target gas pressure (see Figure 2.5 and ref. [18]). The intensity is reduced significantly within 8 minutes. The  $OH^*$  ( $A^2\Sigma^+ \rightarrow X^2\Pi$ ) transition shows a strong emission from light noble gases if water vapor is an impurity present in the target gas.

At pressures higher than 200mbar the “0-Stream” (Figure 2.4) valve is kept closed and both valves “EXP-IN” and “EXP-OUT” as well as “M” are opened, so that the gas is led through the target chamber. Since the circulating pump cannot be used for pressures lower than 200mbar, the purification circuit has to be run separately for lower pressures. The valves “0-Stream” and “M” are kept open in that case. Via “EXP-IN” and a dosing valve following it, an exactly regulated flow of gas is led into the target chamber

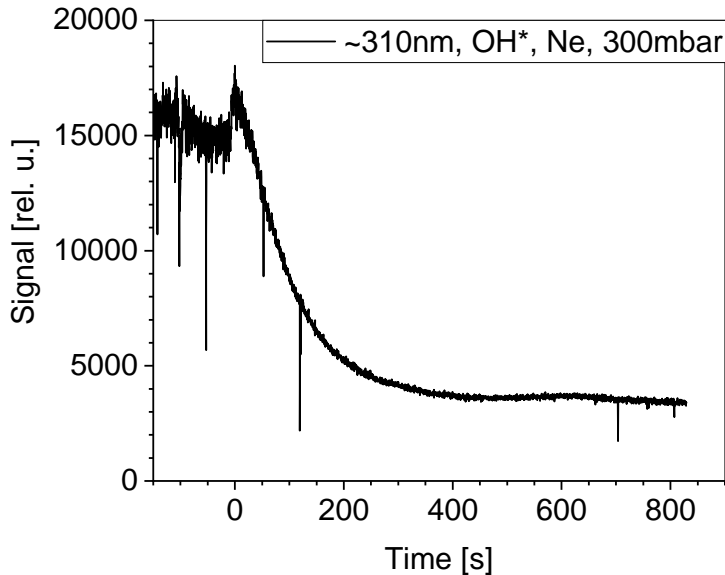


Figure 2.5: Test of the rare gas purifier. The monochromator was set to a wavelength of 310nm and photon counting was started. The light emission from the 310nm OH\* impurity was recorded in dependence of time when the purifier was started [18]. After roughly 7 minutes a constant level is reached. The short time losses in intensity is due to instabilities of the accelerator beam.

and pumped by a turbomolecular pump (TMP) on the other side of the target chamber. For 1mbar and below the titanium entrance foil for the ion beam is removed and only an aperture of 1.0mm diameter serves as entrance into the chamber. In this case differential pumping towards the beamline is performed: two additional TMPs were mounted to the beamline close to the target chamber with another aperture (diameter: 4.5mm) as differential pumping stage in between. With this setup pressures in the target chamber from 1mbar maximum down to  $10^{-5}$ mbar can be realized without disturbing the upstream beamline vacuum.

For pressures between 100mbar and 0.020mbar monitoring is performed by a MKS Baratron Type 390H-01000 capacitive absolute pressure manometer with a MKS Type 270 Signal conditioner. The accuracy of the pressure measurement is  $\pm 0.1\%$ . The value of the last of four digits of the display varies by  $\pm 2$ . This leads to a maximum reading error of  $\sim 10\%$  at 0.020mbar and lower reading errors for higher pressures.

For pressures below 0.020mbar a BARION-atm manufactured by VACOM is used. The display and controlling device is a BARION-MultiGraph. The BARION-atm is a wide range vacuum meter. It consists of a hot-cathode ionization gauge and a Pirani gauge and can therefore cover a pressure range

from  $5 \cdot 10^{-10}$ mbar up to 1000mbar. The accuracy of the measured value is  $\pm 20\%$  and the measurement is gas dependent. The pressure values obtained from the hot-cathode ionization gauge have to be multiplied with a factor for the gas used (nitrogen: 1, neon: 3.8, argon: 0.8, krypton: 0.5, xenon: 0.4). The gas dependence of the Pirani gauge is also pressure dependent. Coming down from higher pressures the BARION atm switches at 0.01mbar from Pirani to hot-cathode and coming up from low pressures switches at 0.1mbar from hot-cathode to Pirani. By using the MKS Baratron for pressures of 0.02mbar and higher, the complicated gas dependence of the Pirani can be avoided. Also a higher accuracy is achieved with the MKS Baratron.

## 2.4 Impurities

Switching between target gases, opening the target chamber to insert or remove the Ti entrance-foil or modifying the gas system and the target chamber leads to various impurities in the target gas. As mentioned above in section 2.3 a rare gas purifier was used to purify the gas from impurities like  $H_2O$ ,  $CO$ ,  $CO_2$ ,  $CH_4$  and  $N_2$ . However this might not be sufficient in certain cases. Leaving the target chamber open for a longer time leads to attachment of vapor on the walls of the target chamber. Thus, precautions were taken that the target chamber was never left open or filled with air for a long time and it was sufficiently flushed with the target gas before starting the experiments. Furthermore, heating bands were wrapped around the target chamber to let the walls outgas for a few days before the experimental runs. Nevertheless, impurities appeared sporadically. Especially the vapor from the walls could never be removed completely and always left a slightly visible  $OH^*$  emission in the spectrum at about 310nm. Certain xenon and krypton lines were also visible in a few spectra taken after having used those gases previously. Xe and Kr are easily excited by light emission from argon and neon and lead to a distinct emission of typical xenon and krypton lines even if the concentration of these atoms in the system is extremely small. On top of that especially xenon is difficult to remove from the target chamber and the gas system once it has been in it.

## 2.5 Spectroscopic setup

The spectroscopic setup consists of three main parts: mirror optics box, monochromator and photomultiplier tube (PMT). The mirror optics box serves the role of an objective lens, collecting incoming light and enabling

focusing on the desired position. The monochromator selects light of certain wavelengths and leads it towards the photomultiplier tube in which the light is detected.

### 2.5.1 Mirror optics box

The mirror optics box (Figure 2.6) was designed and built by M. Salvermoser as part of his PhD thesis [19]. The spectroscopic setup was designed to detect light with wavelengths down to 110nm. Regular glass absorbs light at wavelengths below 300nm, thus, focusing and imaging with glass lenses is not an option. Therefore, focusing and imaging was achieved using  $MgF_2$  coated aluminum mirrors. The light emitted from the ion beam region reaches the mirror optics box through a  $MgF_2$ -window. A collimating mirror is used to focus the light onto the entrance slit of the monochromator. The ratio between the diameter of the light beam and the focal length is  $d/f = 1/5$ . A plain mirror featuring adjusting screws is used for steering and adjusting the image to the right location. A metal bellow between the mirror optics box and the monochromator prevents tension between the two heavy boxes. The mirror optics box is evacuated through a flange on top of the box where a turbomolecular pump can be mounted. Before entering the monochromator the light passes through a filter wheel. The filter wheel gives the possibility to switch between filters to suppress second and higher order spectra of the grating monochromator.

### 2.5.2 Monochromator

Spectra were recorded with a “Model 218 0.3-Meter Scanning Monochromator” manufactured by McPHERSON INSTRUMENTS. It features a 1200 lines/mm grating with a blaze wavelength of 300nm, a ruled width of 52.8mm and groove lengths of 52.8mm. It has a special coating of Al and  $MgF_2$ . The monochromator can be operated both in vacuum and at atmospheric pressure. In the presented experiments it was only evacuated for a few special measurements at wavelengths below 300nm. By design, wavelengths in the range from 105nm up to  $16\mu m$  can be investigated. The spectral resolution at a slit width of  $10\mu m$  is 0.03nm. Figure 2.7 shows a schematic drawing of the light path. The light enters through the entrance slit and is collimated onto the grating by a collimating mirror [20]. The grating splits the incoming light into its various wavelengths due to constructive interference and different angles. This light is then focused onto the exit slit by a focusing mirror. It can be seen that the entrance slit determines the intensity of the light that gets into the monochromator and is later detected by the photomultiplier

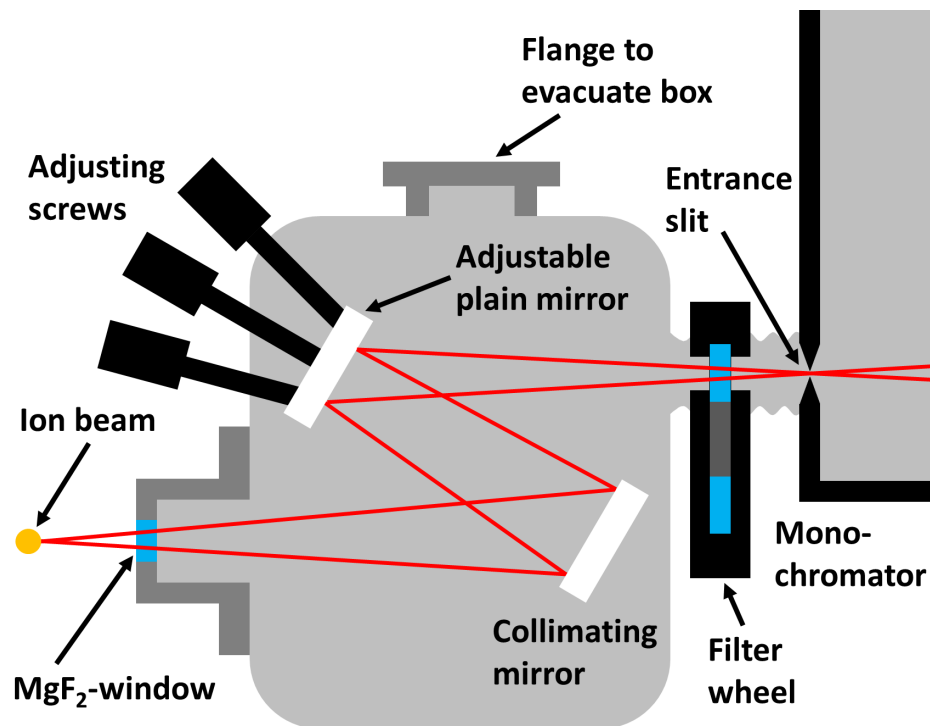


Figure 2.6: Schematic drawing of the mirror optics box designed and built by M. Salvermoser during his work for his PhD thesis [19]. With the help of the adjustable plain mirror the focus can be shifted in all three dimensions. The whole box can be evacuated through the flange on top. All the  $d/f$  values are  $1/5$ , adapted to the value of the monochromator:  $d/f = 1/5$ .

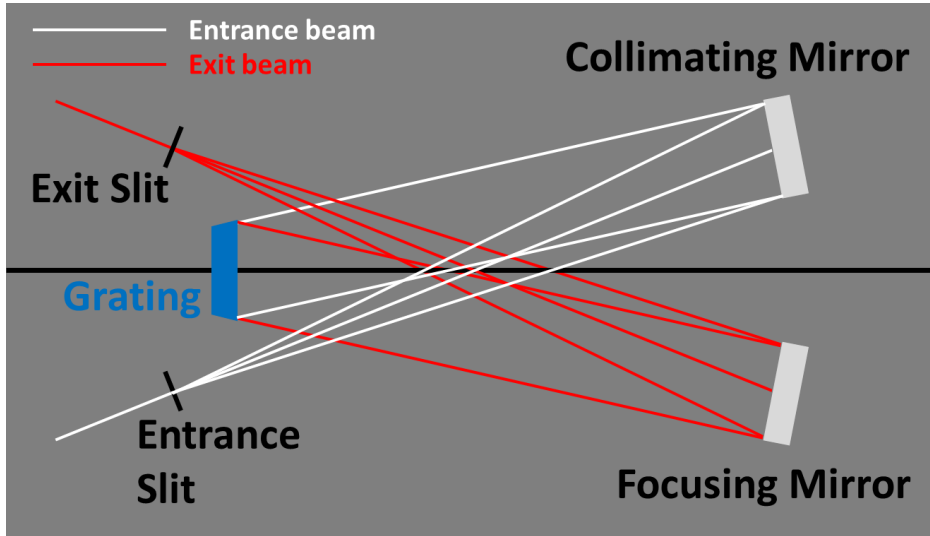


Figure 2.7: Schematic drawing of the inside of the monochromator. A light beam enters the monochromator through the entrance slit and is collimated by a collimating mirror and directed onto the grating. Depending on the angle of the grating monochrome light of a certain wavelength reaches the focusing mirror that focuses the monochrome light onto the exit slits through which it gets into the photomultiplier tube (PMT). In this monochromator  $d/f = 1/5$  applies.

tube (PMT). Through the exit slit the light reaches the PMT. The slit width of both slits determines the wavelength resolution.

A Model 788 Scan Controller with a  $1.8^\circ$  stepping motor is connected to the monochromator. This stepping motor rotates the grating so that different wavelengths are selected. The stepping motor has a step width that corresponds to  $1/144\text{nm}$  ( $\approx 0.0069\text{nm}$ ) [21].

### 2.5.3 Photomultiplier tube and photon counting (PMT)

The photomultiplier tube (PMT) was custom built by ET Enterprises Ltd on the base of a 9130/350B photomultiplier featuring a  $MgF_2$  entrance window of 30mm diameter in a QL30-04 PMT housing with integrated constant fraction discriminator (cfd). The photocathode is a S20 cathode with an active diameter of 9mm and is still sensitive down to 110nm. The PMT housing can be mounted to a vacuum system. The cfd was not used in this experiment. Datasheets are available for more detailed information [24] [25].

Time resolved measurements are possible as well: the single electron rise time is 3.5ns, the single electron FWHM is 5ns and the transit time is 30ns. An afterpulse time window between 50 and 3500ns has to be considered.

The signal from the anode of the PMT was sent to a Canberra 1428A Con-

stant Fraction Discriminator. The photon counting is done using a LeCroy 2551 Scaler and a Wiener CC32 CAMAC crate controller in a LeCroy 8025 CAMAC Rackmount Mainframe. The data is sent to a computer and processed with a LabView spectroscopy program developed by the group for earlier experiments.

## 2.6 Beam profile monitors

Three different types of beam profile monitors were used during the beam-times: one CCD-camera, one iCCD and one EMCCD. First the CCD-camera (ATIK 383L+) was used as a preliminary solution, since it was already used by the research group in several experiments before and was available. Due to very long exposure times especially at very low target gas pressures it was necessary to improve the beam profile monitor. During one beamtime (beam-time with proton beam) an EM CCD camera (ProEm+ 512B) was borrowed from our colleagues from GSI Darmstadt. Later on, an iCCD camera (PI-Max4) was purchased and used for the final beamtimes. All beam profile monitors were calibrated absolutely and further tests were performed (see section 2.6.4 and 2.6.4).

### 2.6.1 ATIK 383L+

The ATIK 383L+ is a CCD camera which is mainly used in amateur astronomy-applications. The following and further information can be found in [26] for the camera and [27] for the sensor. A Broad-Band Anti-Reflection (BBAR) coated quartz window serves as entrance window behind which a KAF-8300 CCD sensor is located. The KAF-8300 sensor consists of 3448x2574 pixels (3326x2504 active pixels) with a pixel size of  $5.4\mu\text{m} \times 5.4\mu\text{m}$ . The CCD is read out by a 16 bit analog to digital converter (ADC) and the pictures can be downloaded via USB 2.0 to a computer. The downloading takes roughly 10s. This long download time makes this camera a very inconvenient choice for real time applications. Furthermore a minimum exposure time of 200ms is required due to a mechanical shutter, which otherwise produces vignetting effects. The spatial resolution at the position of the beam was determined to  $(61 \pm 5)\mu\text{m}$ .

### 2.6.2 PI-Max4 1024f

The final solution as a beam profile monitor in this project is the PI-Max4 1024f. It is an intensified CCD camera (iCCD) manufactured by Princeton

Instruments. The following information is excerpted from [29]. The CCD chip is a full frame, back illuminated e2v CCD 47-10 with 1024 x 1024 pixels with a size of  $13.0\mu\text{m} \times 13.0\mu\text{m}$  (active area: 13.3mm x 13.3mm). The image intensifier is a micro-channel plate (MCP) with a minimum gating time of 2.94ns. The intensifier is coupled via fiber optics to the CCD array. The Gain of the intensifier can be varied in relative units between 1 and 100. For low light applications On-CCD accumulation is possible to reduce readout noise. Dark noise is lowered by using cooling with a Peltier device combined with internal fans. Without additional coolant circulation a temperature of  $-25^\circ\text{C}$  can be reached. Higher sensitivity can be gained by hardware binning. Due to the already not so great spatial resolution of  $(220 \pm 25)\mu\text{m}$  at the position of the beam, this was not done in this project.

For pulsed applications, like a pulsed ion beam, an external as well as an internal trigger can be used. Additional to exposure time and readout time, the delay due to the decay-time of the phosphor of the phosphor on the fluorescence screen has to be considered for determining the dead-time. The readout is accomplished by shifting the charge of the pixels to the shift register, where it is amplified and digitized. Download and remote control is done via a Gigabit Ethernet (GigE) interface. At 10MHz a transfer rate of 7.89 frames per second is possible. The entrance window of the camera consists of fused silica. An objective can be mounted to the front of the camera via a C-Mount.

### 2.6.3 Pro EM+ 512 B

The ProEM+ 512B is a Electron Multiplying CCD (EMCCD) camera manufactured by Princeton Instruments. The following information is excerpted from [28]. It features a back illuminated EMCCD (CCD-sensor: e2v CCD 97B) with 512 x 512 pixels, where the pixel size is  $16\mu\text{m} \times 16\mu\text{m}$  and low noise readout electronics. The on-chip multiplication gain is used in low light applications to lift the signal out of the readout noise. The image is transferred to a frame transfer area and read out via a multiplication gain register. In this register the charge is amplified from pixel to pixel by a clock voltage and impact ionization leads to the multiplication of electrons. This gain lifts the signal far above the readout noise. A downside of the EMCCD is the clock induced charge (CIC): with a certain probability additional charge is induced in this process and will be multiplied just the same as the signal. An increase of the sensitivity of the CCD hardware is possible by binning. This, however, results in a decrease of the spatial resolution. The spatial resolution without hardware binning is  $(170 \pm 15)\mu\text{m}$ . The minimum exposure time was measured to 30ms.

Both, a high speed EM mode for fast kinetics and a low speed normal CCD mode with very low read out noise is available. To reduce dark noise the CCD can be cooled down to below  $-90^{\circ}\text{C}$ . For temperature stability reasons a temperature of  $-70^{\circ}\text{C}$  is recommended by the manufacturer. Alternatively to a fan liquid coolant circulation is available. Remote operation and download of images is possible over a single cable due to a Gigabit Ethernet (GigE) interface.

The entrance window of the camera is a UV grade fused silica window and therefore still transmissive for light of wavelengths below 200nm. An objective can be mounted to the C-Mount at the front.

## 2.6.4 Calibration of the cameras

An important goal of the experiment is to determine the absolute value of the effective emission cross-sections of certain emission lines that are of special interest. Therefore it is necessary to absolutely calibrate the sensitivity of the camera systems used. This was performed with the selected bandpass filters in a series of measurements, which is also described in more detail in reference [22].

A Wi17/G tungsten-strip calibration lamp manufactured by OSRAM was used as light source. The spectral radiance distribution for the lamp was given by a test report from the manufacturer for a certain region of interest (ROI) on the strip of the lamp. The transmission curves of the bandpass filters used had been measured before and was therefore well known (see Figure 2.15 to Figure 2.19 in section 2.6.7) as well as the transmission of the objective lens (see Figure 2.13 in section 2.6.6). The distance of the cameras to the lamp was chosen to be the same as in the beamline experiments. Thus a direct comparison of the values was possible.

However, for the absolute calibration the solid angle had to be measured as well. For that purpose a circular aperture of 10.0mm diameter was put in front of a point-like light source exactly on the optical axis. The position of the aperture was shifted towards the camera. The knowledge of the position at which a reduction of the measured intensity occurs enables to calculate the solid angle that is captured by the camera system.

The linearity of the signal with exposure time is given for all three cameras within the dynamic range (up to a grey value of  $\sim 45,000$  of 65,535 maximum) used in this work [22]. The results for the sensitivity of the three cameras are shown in Figure 2.8. As expected the iCCD camera (PI-Max4) with its S20 cathode is more sensitive towards the shorter wavelength region, while the silicon based CCD cameras (ATIK and ProEM+) are more sensitive in the longer wavelengths region.

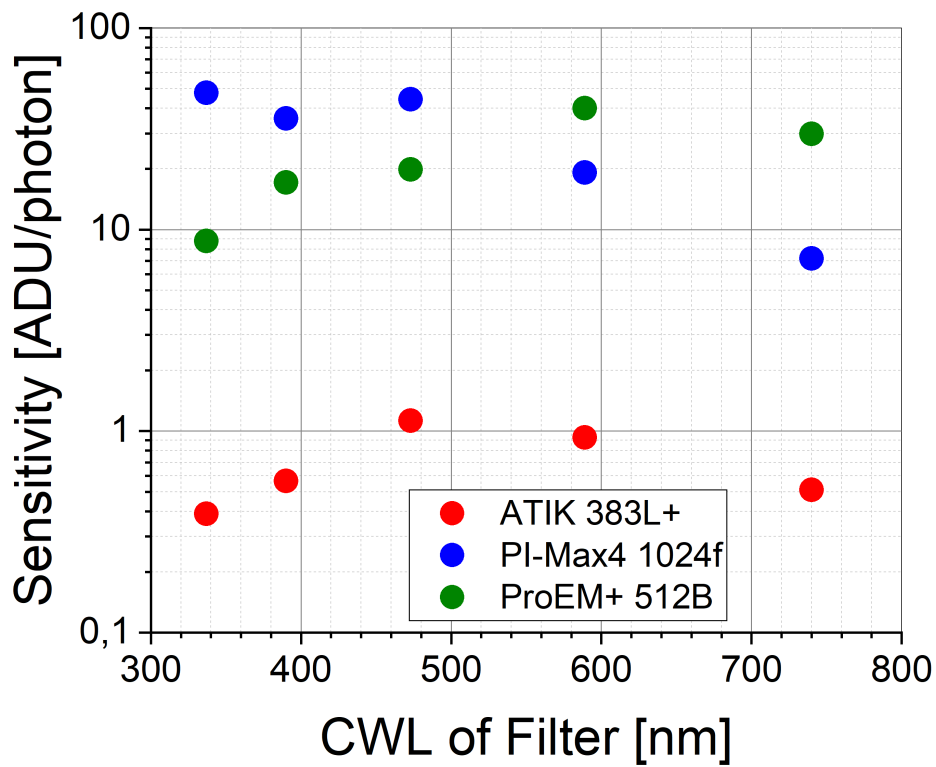


Figure 2.8: Sensitivity of the three cameras plotted versus the central wavelength (CWL) of the bandpass filters used. The ATIK and the ProEM+ have silicon CCD chips and are therefore more sensitive towards longer wavelengths in comparison to the PI-Max4 camera that has a S20 cathode in the intensifier and is designed to detect light with shorter wavelengths.

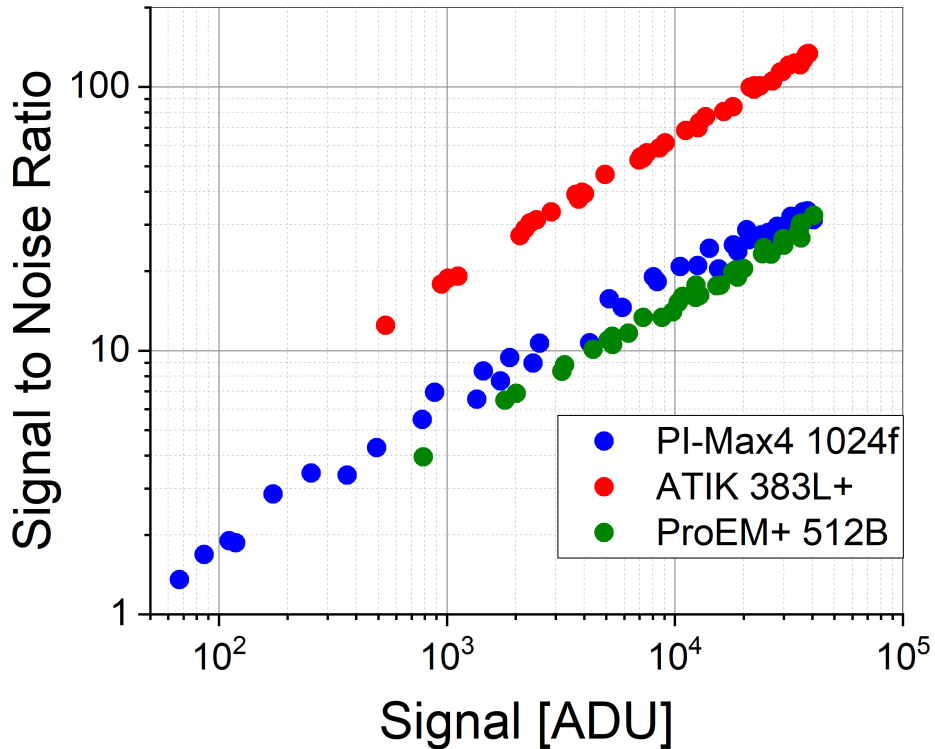


Figure 2.9: Signal to Noise Ratio (SNR) for each of the cameras plotted versus signal. Intensification (PI-Max4) and multiplication (ProEM+) of the signal leads to more noise and thus to a lower SNR. The signal was varied by varying the exposure time.

Furthermore the signal to noise ratio (SNR) was calculated and is shown for each camera in Figure 2.9 versus signal strength. With the ATIK 383L+ a SNR of roughly 100 can be reached and the SNR is generally a factor 3 or 4 higher than in case of the PI-Max4 or the ProEM+. However, more incoming photons per pixel are necessary to reach such a high SNR compared to the intensified CCD camera (PI-Max4) as can be seen in Figure 2.10. The number of pixels receiving light from the ROI differs for the different cameras due to the different pixel sizes. A comparison of the active pixel number and sizes is shown in Table 2.1 as well as the gain setting used. The ATIK 383L+ has 2400 pixels in the ROI, the PI-Max4 has 396, and the ProEM+ 270. It is interesting to note that the electron multiplied CCD (ProEM+) has almost the same SNR for a given exposure per pixel as the pure CCD (ATIK). Hence, the electron multiplication does not improve the SNR for a given exposure significantly. The total exposure of the ROI is proportional to the exposure time. Thus, the SNR can be calculated for a relative exposure time. Here it is normalized to an attenuation of the calibration lamp by neutral density filters by a factor of 10<sup>4</sup>. It can be seen in Figure 2.11 that the exposure

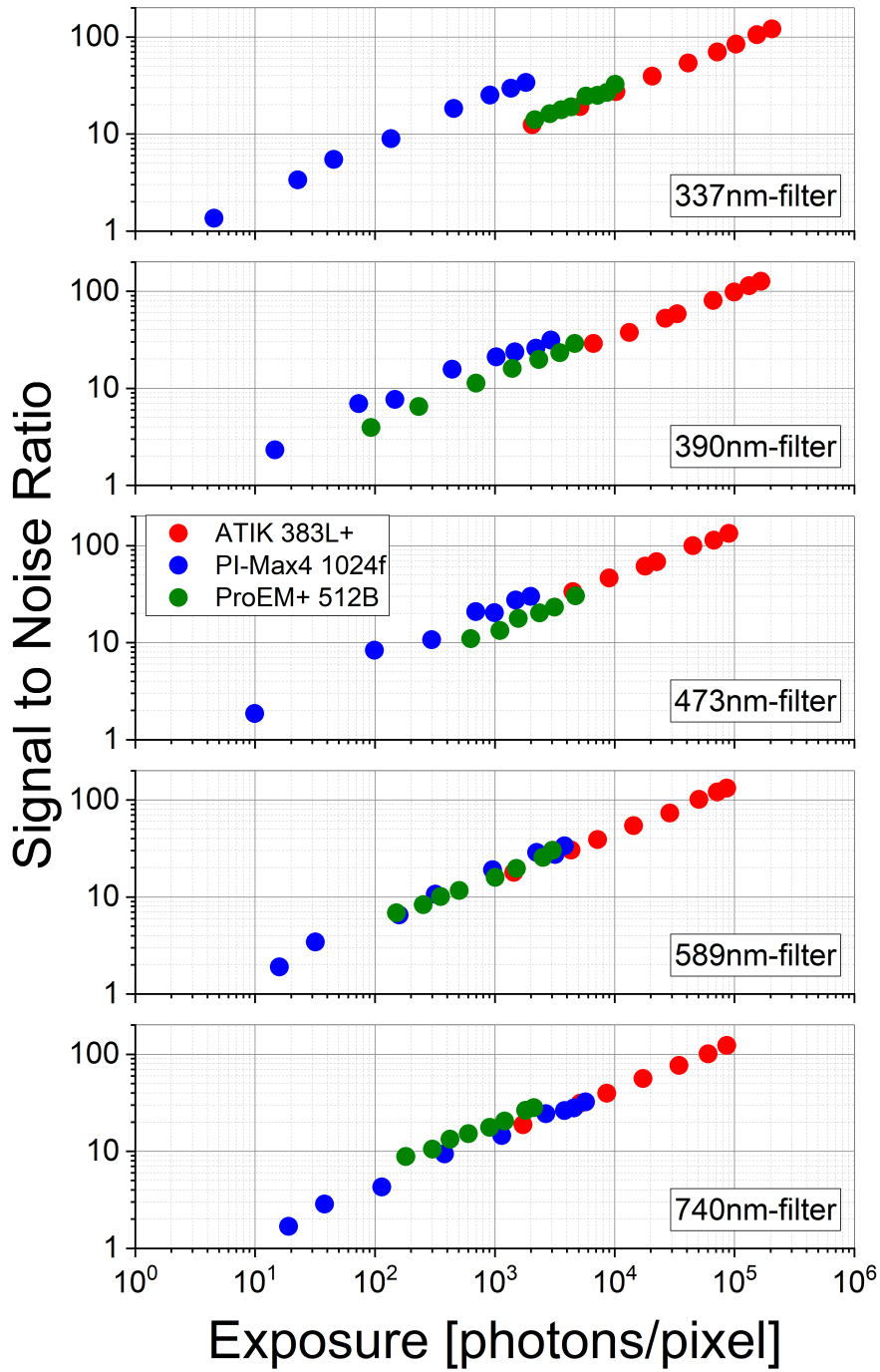


Figure 2.10: Signal to Noise Ratio (SNR) plotted versus exposure per pixel. In case of the PI-Max4 camera the full dynamic range of exposure times of the chip was used, while in case of the ATIK camera the minimum exposure time is 200ms due to its mechanical shutter and for the ProEM+ camera the minimum exposure time is 30ms. This limited the minimum exposure to the measured values.

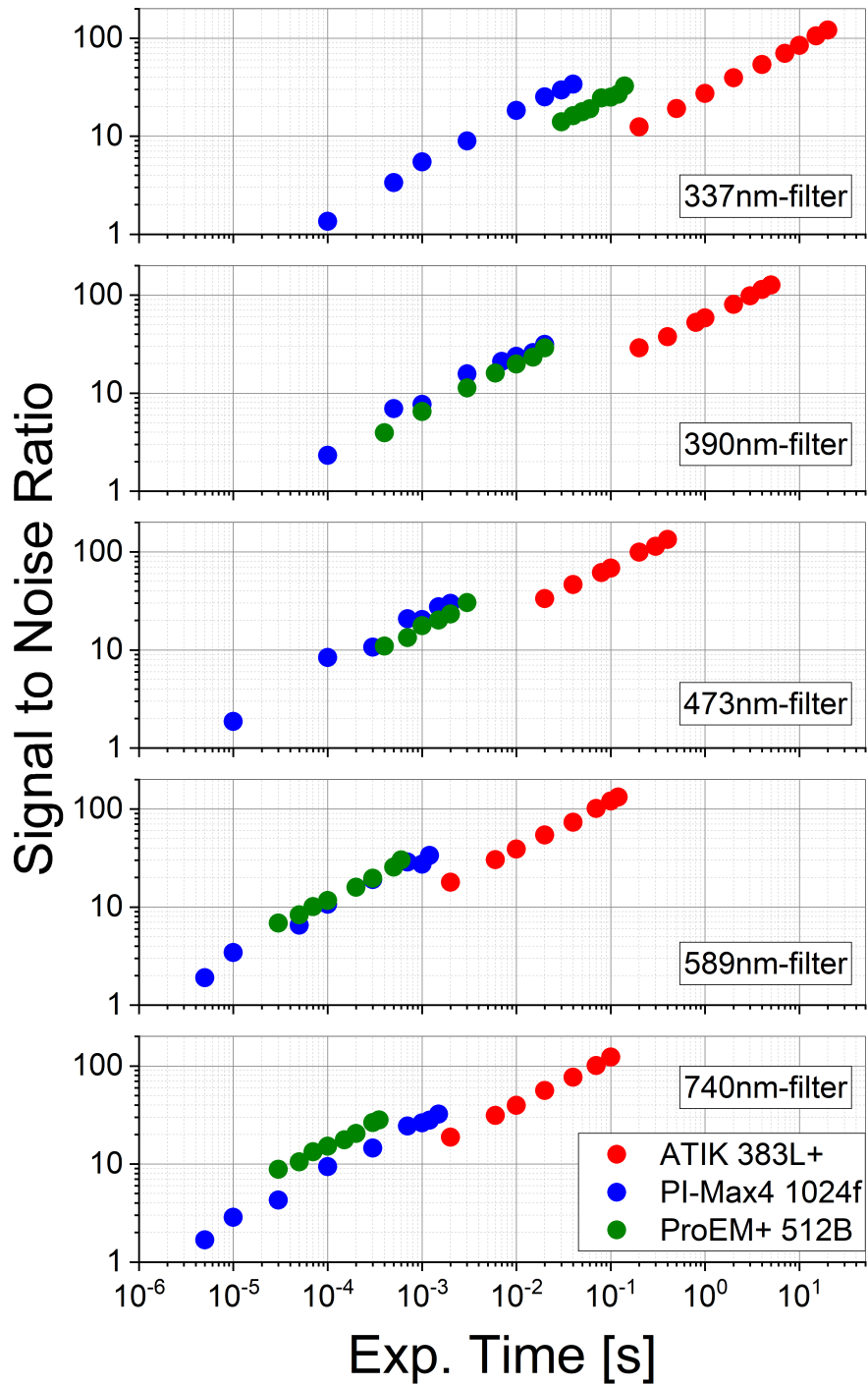


Figure 2.11: SNR plotted vs exposure time. The exposure time is normalized to an attenuation by neutral density filters by a factor of  $10^4$  and therefore serves more for relative comparison than for absolute values of exposure times. The measurement was performed using the Wi17/G tungsten-strip lamp.

times are generally much higher for the ATIK 383L+ with its pure silicon CCD chip. For low light applications the intensified CCD (PI-Max4) or the electron multiplied CCD (ProEM+) are much better suited if a SNR of up to 25 is sufficient. The exposure time for the same SNR is almost 2 orders of magnitude shorter than for the ATIK 383L+ in case of short wavelengths (337nm). For longer wavelengths (740nm) it is still roughly one order of magnitude. The advantage of the ProEM+ over the ATIK 383L+ is mainly due to its larger pixels on the chip, resulting in more photons detected per pixel during a given exposure time.

Whether choosing the PI-Max4 or the ProEM+ depends on the wavelength of the light that is to be detected. Another aspect to be considered is gating. Out of the three cameras only the PI-Max4 can be operated in a gated mode. A minimum gating time of  $\sim 3\text{ns}$  is possible (as mentioned in section 2.6.2).

No.	Name	Pixel size [ $\mu\text{m} \times \mu\text{m}$ ]	Active pixels	Gain setting
1	ATIK	$5.4\mu\text{m} \times 5.4\mu\text{m}$	3326 x 2504	x
2	PI-Max4	$13\mu\text{m} \times 13\mu\text{m}$	1024 x 1024	90
3	ProEm+	$16\mu\text{m} \times 16\mu\text{m}$	512 x 512	100

Table 2.1: Information about the CCD chips of the cameras used in the experiments [26] [29] [28]. The last column shows the setting of the gain throughout all experiments.

### 2.6.5 Spatial resolution of the camera systems

The spatial resolution was measured in a separate experiment. For this experiment the same objective lens was used as for the ion beam experiments and the focusing was kept at the same position as well. The distance to the object was also the same. An adjustable slit with an illuminated white sheet of paper behind the slit was photographed (see Figure 2.12). The sharp edge is imaged with all three camera systems. Measurements with and without bandpass filters were performed but no significant difference between measurements was observed. The spatial resolution was determined using pixel distance for the 10% to the 90% intensity value. The results are listed in Table 2.2 and also discussed in reference [22].

When considering the spatial resolution in pixel units the pure CCD camera (ATIK 383L+) and the EMCCD camera (ProEM+ 512B) have the best spatial resolution. Their spatial resolution in pixel size units is in fact very

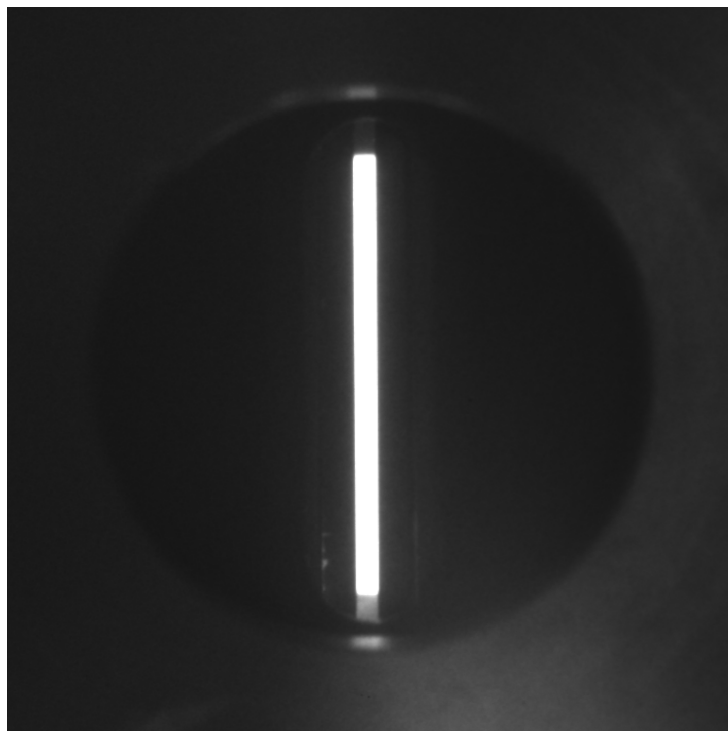


Figure 2.12: Photograph of the slit used to determine the spatial resolution of the camera systems used.

similar. The pixel size of the ProEM+ 512B is just much larger ( $5.4\mu\text{m} \times 5.4\mu\text{m}$  vs.  $16\mu\text{m} \times 16\mu\text{m}$ ). This result is expected since both camera have no amplification or multiplication of the incoming signal before reaching the chip. In the EMCCD camera the charge that is deposited in the chip is multiplied prior to readout (see section 2.6.3).

Significantly worse is the spatial resolution of the iCCD camera (PI-Max4). This is due to the intensifier in front of the CCD. The conversion of photons into electrons on the cathode of the intensifier, the acceleration of the produced electrons and finally the conversion of the electrons back into photons in the phosphor clearly reduces the possible spatial resolution. Since this is the main limiting factor of the spatial resolution, smaller pixel sizes would most probably not improve the spatial resolution.

Imaging objects with known dimensions make it possible to determine the magnification of the camera systems. The width of a pixel at the position of the object can be calculated (Column (**F**) of Table 2.2) and absolute spatial scaling in the images is possible. Hence, the spatial resolution at the position of the object (in our case the ion beam) is calculated (Column (**D**)).

The spatial resolution of the optical system depends on the objective lens, the sensor of the camera and the optics in the camera in front of the sensor. As mentioned above an image intensifier in front of the CCD can significantly worsen the spatial resolution. The resolution of the objective lens is limited due to diffraction. The limit of the resolution for a given diameter  $D$  of the aperture can be calculated with the Rayleigh criterion

$$\alpha \approx 1.22 \frac{\lambda}{D}. \quad (2.1)$$

The diameter of the aperture was  $D = f/k = 60\text{mm}/4 = 15\text{mm}$ . The distance of the aperture from the object was roughly 330mm. This leads to a limit of the spatial resolution of  $9\mu\text{m}$  for light of the wavelength  $\lambda = 337\text{nm}$ , and  $20\mu\text{m}$  for light of the wavelength  $\lambda = 740\text{nm}$ . In the measurements no significant differences between the spatial resolution with the different wavelength filters were observed. Another contribution to the spatial resolution is cross-talk in the chip. Crosstalk is diffusion of charge between pixels of the CCD chip. Furthermore, non-ideal focusing of the objective lens may lead to a decrease of the spatial resolution as well. The depth of field was measured to be roughly 5mm, while the chromatic aberration of the apochromatic lens is well below  $60\mu\text{m}$  for the wavelengths of interest. Thus, the chromatic aberration has no significant impact on the spatial resolution.

<b>A</b>	<b>B</b>	<b>C</b>	<b>D</b>	<b>E</b>	<b>F</b>
No.	Name	Spatial Resolution [pixels]	Exp. Spatial Resolution [ $\mu m$ ]	Magnification	Pixel width (at pos. of beam) [ $\mu m$ ]
1	ATIK	$2.9 \pm 0.2$	$61 \pm 5$	1 : 3.9	21.0
2	PI-Max4	$4.5 \pm 0.5$	$220 \pm 25$	1 : 3.7	48.4
3	ProEm+	$2.7 \pm 0.2$	$170 \pm 15$	1 : 4.0	64.1

Table 2.2: Parameters specific for this experiment. The spatial resolution is the measured resolution which is achieved in the beamline experiments. (C) shows the spatial resolution in pixel units in the camera. It was calculated using the 10% to 90% condition. (D) represents the resolution achieved in the experiment given in  $\mu m$ . (E) is the magnification of the optical setup with the given setting. (F) is the width of an object at the position of the beam in the experiment that maps exactly one pixel on the chip.

### 2.6.6 Objective lens

A “*UV-VIS-IR 60mm 1:4 APO Macro*” lens manufactured by JENOPTIK was used as objective lens, with  $f=60mm$  focal length. The lens has an apochromatic waveband from 315nm to 1100nm and a transmission waveband from 290 up to 1500nm. This is especially important for the experiments, since light emission from emission lines around 337nm are imaged as well as from emission lines around 740nm (see Section 3.1). The transmission curve of the objective lens is shown in Figure 2.13 and zoomed into the shorter wavelength region in Figure 2.14. The very small chromatic aberration of below  $\Delta f = 0.05mm$  in the wavelength region of interest is very convenient since the optical setup needs not to be changed when the filters are exchanged. This makes the experiments better reproducible.

The aperture can be varied from  $f/4$  to  $f/45$ , where in this experiment an aperture width of  $f/4$  is used. Only one single measurement with very bright light had to be performed with an aperture of  $f/45$ . This was accounted for by scaling the obtained values to an aperture of  $f/4$ .

The lens features a Nikon F Mount and was mounted to the cameras using appropriate adapters. It has to be noted that the Nikon F Mount is not lightproof, thus, additional opaque cloth was wrapped around the mount. The stated information and further details about the objective lens can be found in [23].

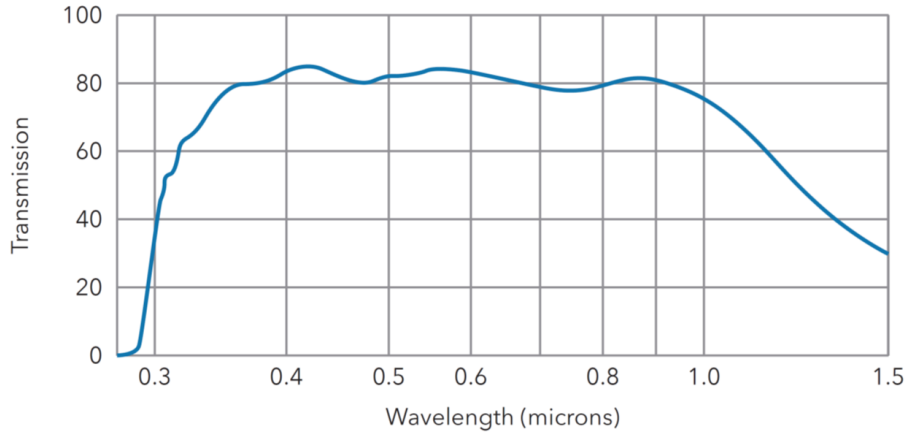


Figure 2.13: Transmission curve of the *UV-VIS-IR 60mm 1:4 APO Macro* objective lens for a wavelength range from below 300nm up to 1500nm. The transmission values are important to determine the sensitivity of the cameras. Plot taken from [23]

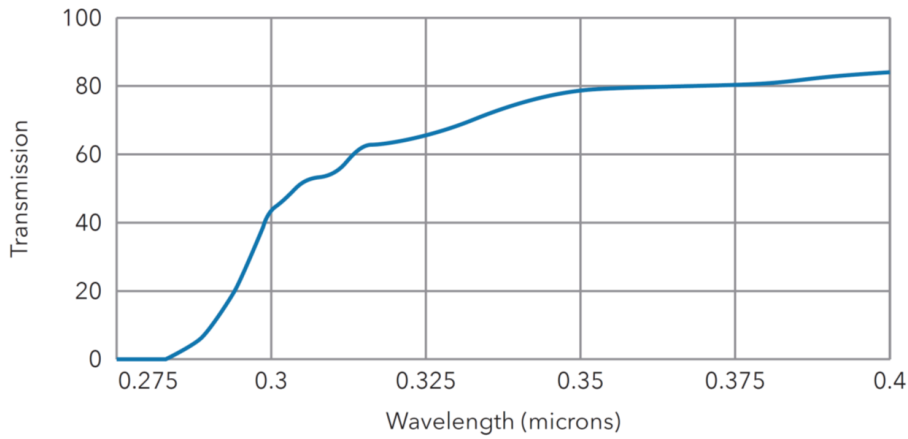


Figure 2.14: Transmission curve of the *UV-VIS-IR 60mm 1:4 APO Macro* objective lens for the shorter wavelengths region between 275nm and 400nm. The objective lens is still well transmissive at 337nm, which is the lowest center wavelength (CWL) of the filters used. Note the logarithmic scale of the wavelength axis. Plot taken from [23]

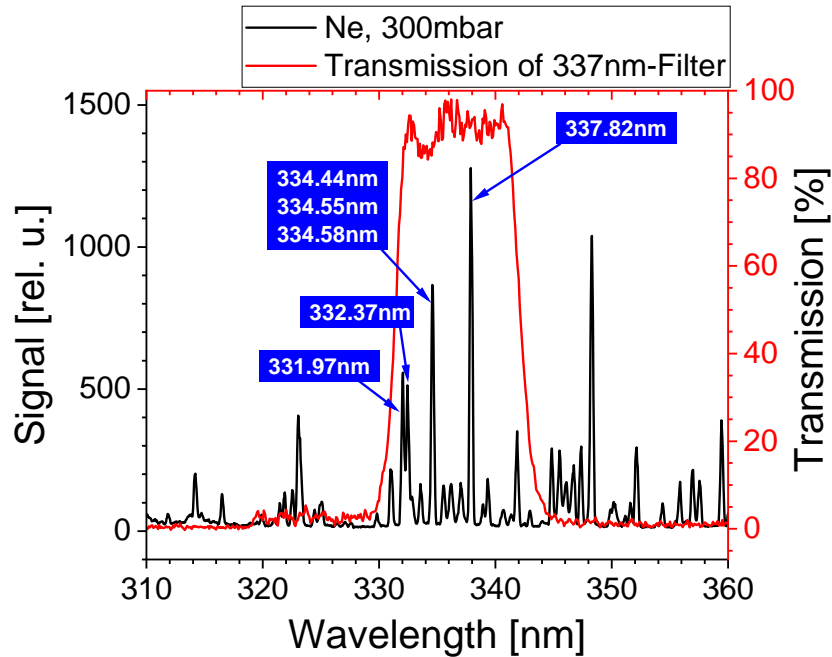


Figure 2.15: Transmission curve of the bandpass filter with 337nm CWL laid over the wavelength spectrum of the light emission from neon at 300mbar.

## 2.6.7 Bandpass filters

Filters with a high transmission in a short wavelength region were required to image the light emission of certain spectral lines with the camera. As will be described in more detail in section 3.1.3, filters with central wavelengths (CWL) of 337nm, 390nm, 473nm, 589nm and 740nm were used. The 337nm-, the 473nm- and the 589nm-filters are hard coated filters, with one hard coating on an optical glass substrate. The advantages are a longer lifetime and a higher transmission in comparison to the traditional coated filters, that consist of three layers. The remaining two filters (390nm and 740nm) are traditional coated filters. The filters were bought from Edmund Optics. The technology and further details are described in reference [30], reference [31] and reference [32].

The transmission curves of the filters are plotted in Figure 2.15 to Figure 2.19 together with corresponding wavelength spectra relevant for the experiment. This visualizes, which spectral lines can pass the filters and which intensity and is detected by the camera. This is important for the interpretation of the results of the beam profile measurements in section 3.3 and the emission cross-sections in section 3.4.

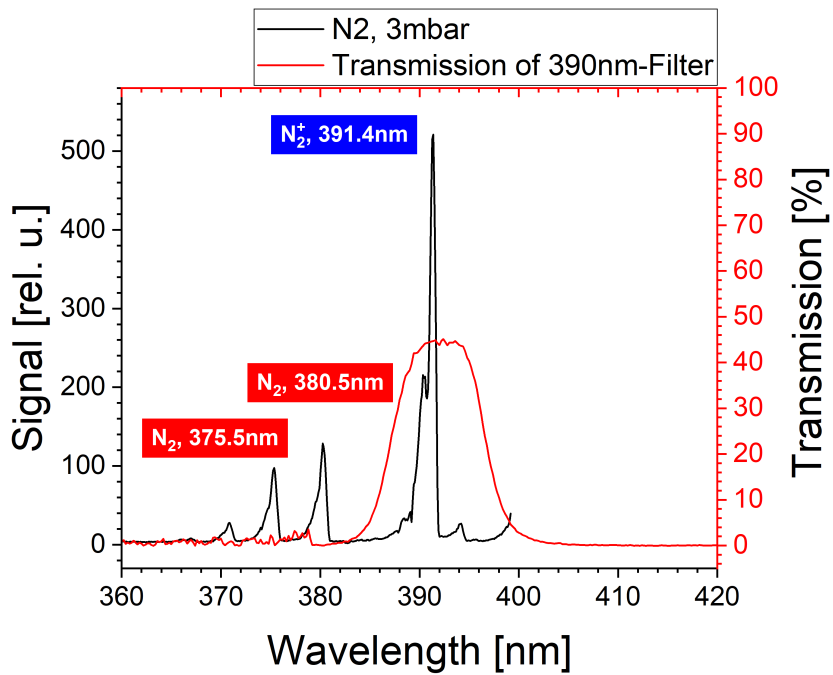


Figure 2.16: Transmission curve of the bandpass filter with 390nm CWL laid over the wavelength spectrum of the light emission from molecular nitrogen at 3mbar.

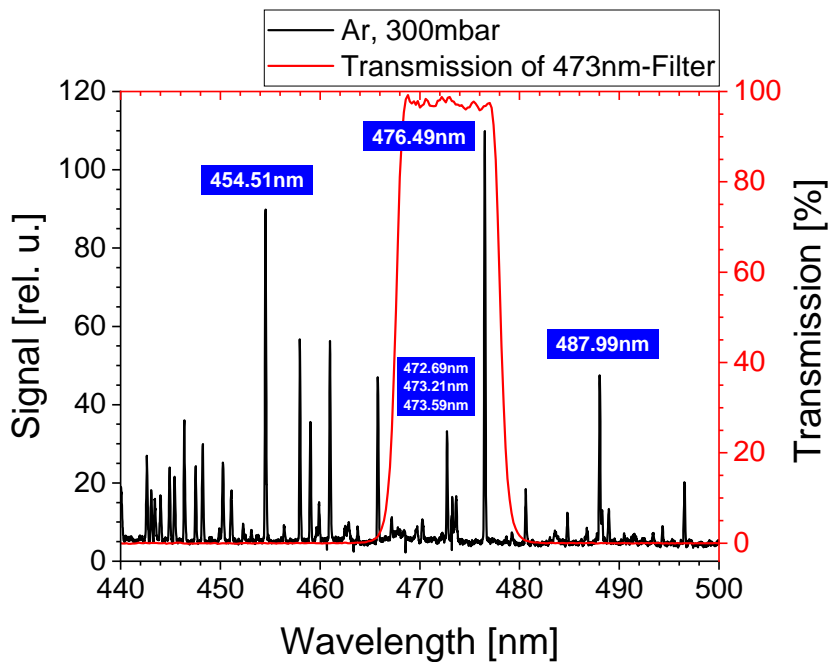


Figure 2.17: Transmission curve of the bandpass filter with 473nm CWL laid over the wavelength spectrum of the light emission from argon at 300mbar.

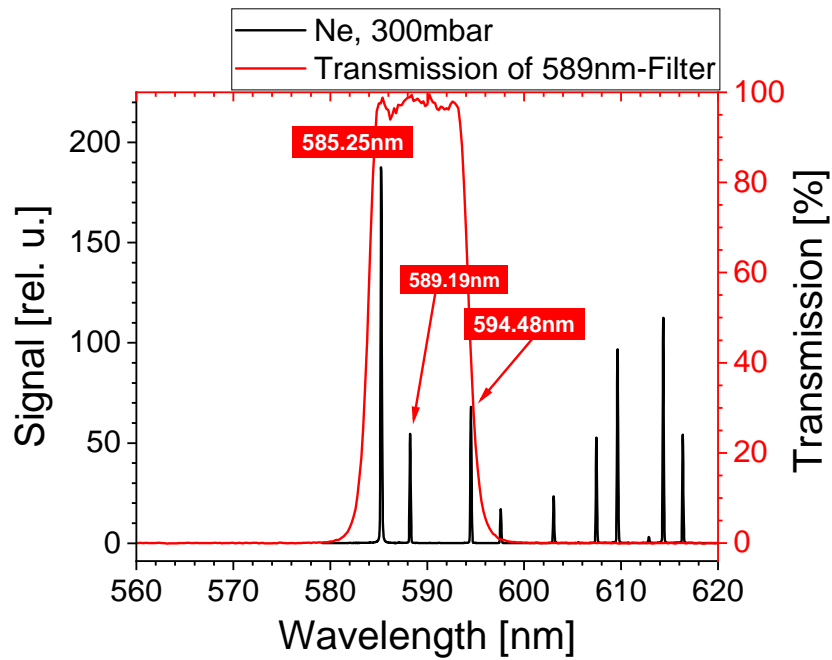


Figure 2.18: Transmission curve of the bandpass filter with 589nm CWL laid over the wavelength spectrum of the light emission from neon at 300mbar.

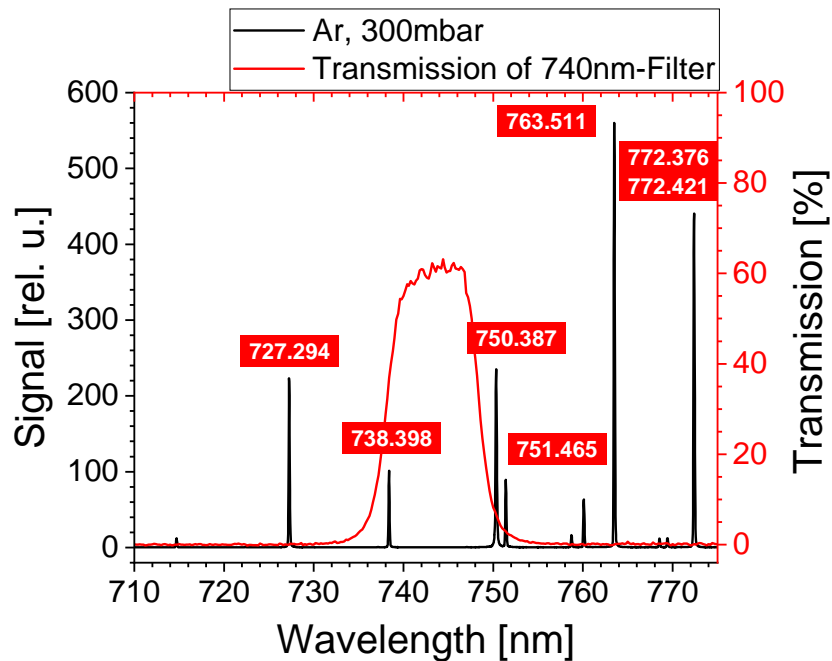


Figure 2.19: Transmission curve of the bandpass filter with 740nm CWL laid over the wavelength spectrum of the light emission from argon at 300mbar.

## 2.7 Electron gun

The high intensity heavy ion beam not only excites the ions and atoms in the target but also produces secondary electrons which excite the target gas as well. While the ion projectiles of the beam interact with the target gas within the trajectory of the beam, the secondary electrons are emitted with a certain angular and energy distribution including transverse emission. So they can travel a certain distance according to their range in the target gas [35]. This is expected to lead to a deviation of the light emission compared to the shape of the original heavy ion beam. Thus, it is of great importance to be able to distinguish excitation due to secondary electrons from the excitation due to ion projectiles. Therefore wavelength spectra were recorded using an electron gun to simulate the secondary electrons. The results will be described in section 3.1.2.

The electron gun used was custom-built by excitech GmbH for this experiment. It can be seen in Figure 2.20. It is based on devices described in reference [36], [37] and [38]. The long tube with the exit foil at the end was necessary so that the electron beam enters the target cell in its center where it can be detected by the spectroscopic setup. The exit foil, a 300nm thick silicon nitride ( $Si_3N_4/SiO_2$ ) foil, with an area of 0.7mm x 0.7mm serves to separate the vacuum inside the electron gun from the gas in the target cell. The energy of the produced electrons can be as high as 12keV and a beam current of up to  $10\mu A$  can be reached [39]. Steering of the beam is accomplished with four magnetic steering coils that are controlled, as well as the other parameters, by software. Figure 2.21 shows the electron gun in operation (mounted from below) in the target cell filled with neon as target gas. The orange NeI light emission can be seen in the center of the target cell.

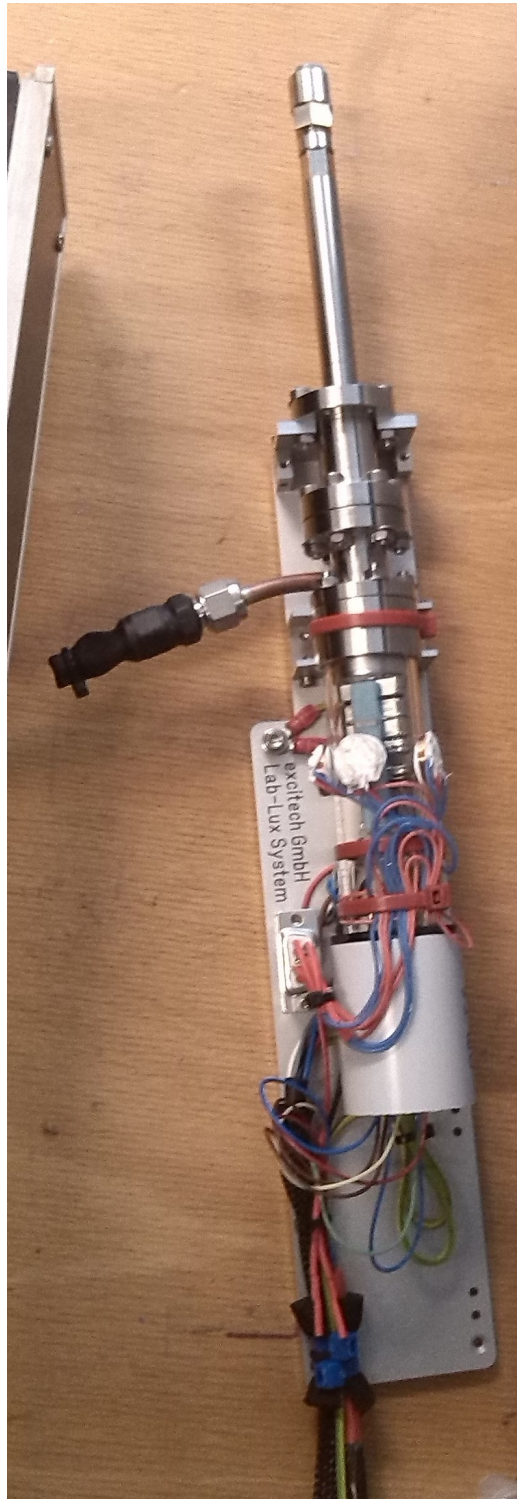


Figure 2.20: Electron gun before being mounted into the target cell. The long tube on the left hand side is the beam line for the electron beam with an exit window.

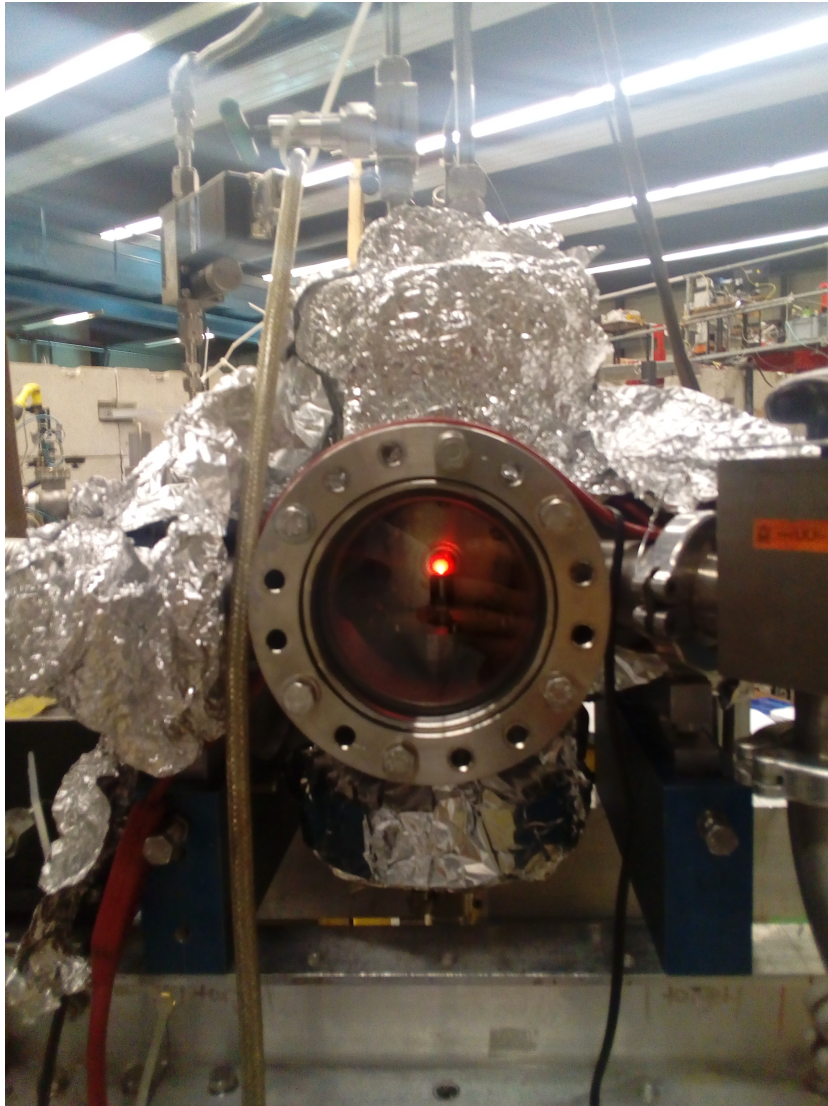


Figure 2.21: Electron gun mounted inside the target cell filled with neon at  $\sim 100$  mbar. Orange NeI light emission can be seen in the center of the cell. It can also be seen that the light emission has a spherical shape due to the scattering of the low energy of the electrons.



# Chapter 3

## Results

Various methods were used to obtain the results of the experiments. The first experiments were performed using the spectroscopic setup described in section 2.5. Spectroscopic results were obtained and the behavior of the wavelength spectra of the respective target gas with varied pressure could be studied. This allowed to find emission lines useful for beam diagnostics both in the region of ionic and neutral emission lines. These emission lines were found to remain well visible even for lower pressures. For these emission lines bandpass filters were bought. With the help of the bandpass filters photographs of the light emission from the excited target gas were recorded. Due to the narrow FWHM ( $\sim 10\text{nm}$ ) of the bandpass filters, certain lines could be selected. From the photographs beam profiles were obtained. After an absolute calibration of the camera systems used, effective emission cross-sections were calculated. The cross-section should be useful for future applications for optical beam diagnostics by scaling the results from the following sections to the particle energy, beam current and even particle species of the respective accelerator experiment.

### 3.1 Spectroscopic results

Wavelength spectra of light emission from a certain target gas depend on the excitation. The spectral lines are typical for the gas. However, the intensity of certain emission lines depends on the projectile that induces excitation. Furthermore, not only excitation of atoms occurs when hitting a target gas with a particle beam. Ionization as well as excitation of the created ions can take place. This is where a big difference between heavy ion beam excitation and electron beam excitation is observed. Figure 3.1 shows typical excitation cross-sections for heavy ion projectiles and electrons in single col-

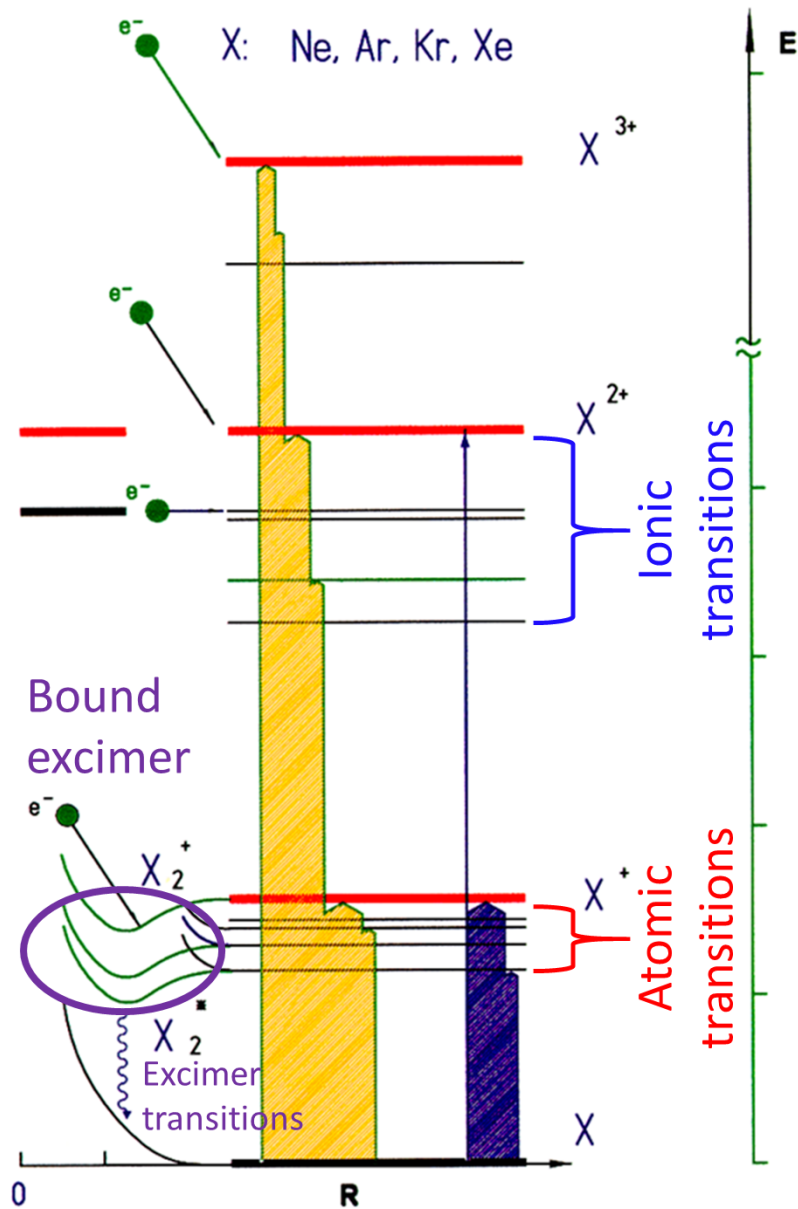


Figure 3.1: This graph shows the excitation cross-sections for the excitation by heavy ion projectiles and electrons in single collisions. The width of the yellow bar represents the excitation by heavy ion projectiles, while the width of the purple bar stands for the excitation by electrons. Electrons almost exclusively excite atoms, the excitation cross-section for excitation of ions is negligible. Heavy ion projectile excite both atoms and ions. Figure taken from [12].

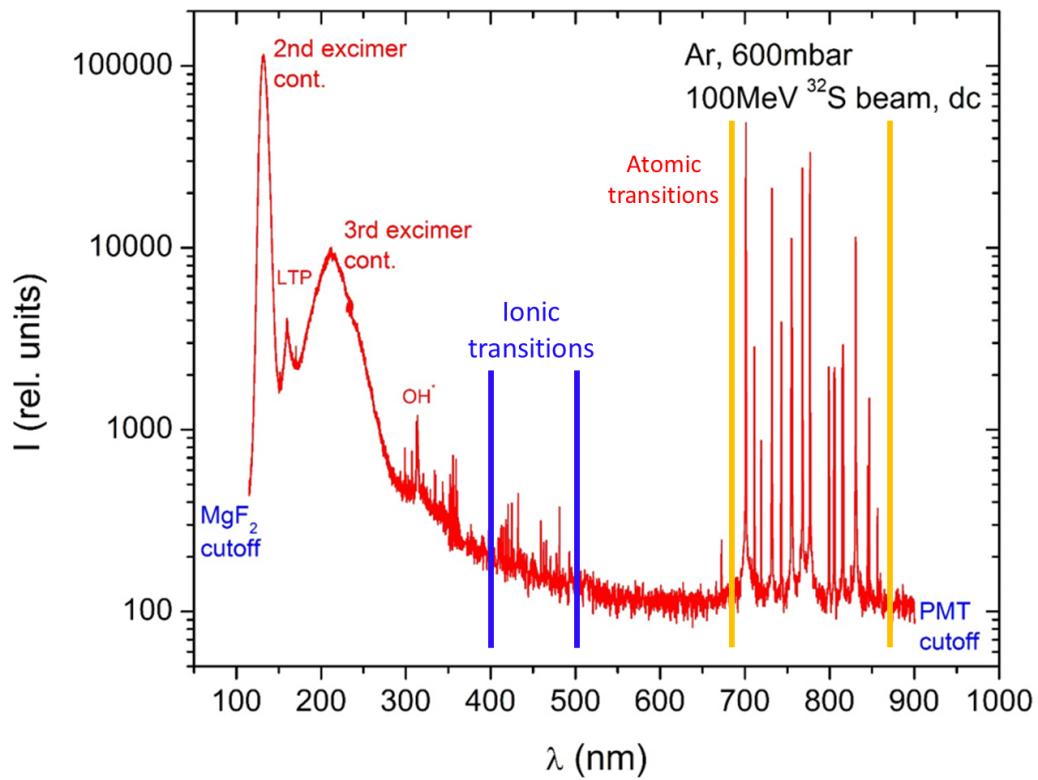


Figure 3.2: Wavelength spectrum over a wide wavelength range recorded in experiments prior to this work [13]. The 2nd and 3rd excimer continuum is visible below 300nm. Furthermore, light emission from impurities ( $OH^-$  at  $\sim 310$ nm) were detected as well. In blue bars the wavelength region where mostly light emission from ionic transitions occur is marked. The orange bars mark the region of atomic light emission.

lisionstypical for the case of a 100MeV sulfur ion and the secondary electrons produced by this projectile. The energy levels are typical for the rare gases neon, argon, krypton and xenon (see also reference [12]). The left side of Figure 3.1 schematically indicates secondary processes such as recombination, charge transfer and the formation of so called excimer molecules. In a collision of heavy ion projectiles with the target atom the ion projectile can both ionize the target atom and excite this newly created ion in the same collision. Due to the high charge of the ion projectile and its co-propagating electrons that get inside the atomic shell it can eject electrons while exciting other electrons in the shell (Fano-Lichten-Model). Here secondary electrons have typical energies in the keV range, thus they can excite target atoms and even ionize them but rarely ionize and additionally excite the created ion. Therefore, the ionic light emission is mostly due to excitation by heavy ion projectiles from the beam. The wavelengths regions in which most light emission from ionic transitions (blue bars) and from atomic transitions (orange bars) occur are marked in Figure 3.2. This spectrum covers a very wide wavelength range and thus shows the 2nd and 3rd excimer continuum as well. It was recorded in experiments prior to this work [13].

Figure 3.3 shows an ion beam induced wavelength spectrum in argon compared to an electron beam induced wavelength spectrum. Between 400 and 500nm mostly emission lines from ionic transitions are visible. Here the relative intensity is much weaker in the case of electron beam excitation (see the zoom into this region in Figure 3.4). This is different in the wavelength region between 690 and 780nm, where mostly emission lines from atomic transitions appear. The intensities are very similar. This will be discussed in more detail in section 3.1.2.

### 3.1.1 Spectroscopic results with heavy ion beam excitation

A heavy ion beam with  $^{32}\text{S}$  ions of charge 8+ was directed into the target chamber. The target chamber was filled with different rare gases as target gas. Wavelength spectra were recorded using the spectroscopic setup described in section 2.5. First, wavelength spectra at relatively high pressures (300mbar) were recorded (see neon and argon in Figure 3.5 and krypton and xenon in Figure 3.6). Two spectra of nitrogen are shown in Figure 3.7. The nitrogen transitions are molecular vibrational-rotational transitions and therefore lead to much wider emission bands than the atomic and ionic rare gas lines.

The overview spectra shown in Figure 3.5 serve as a general overview over

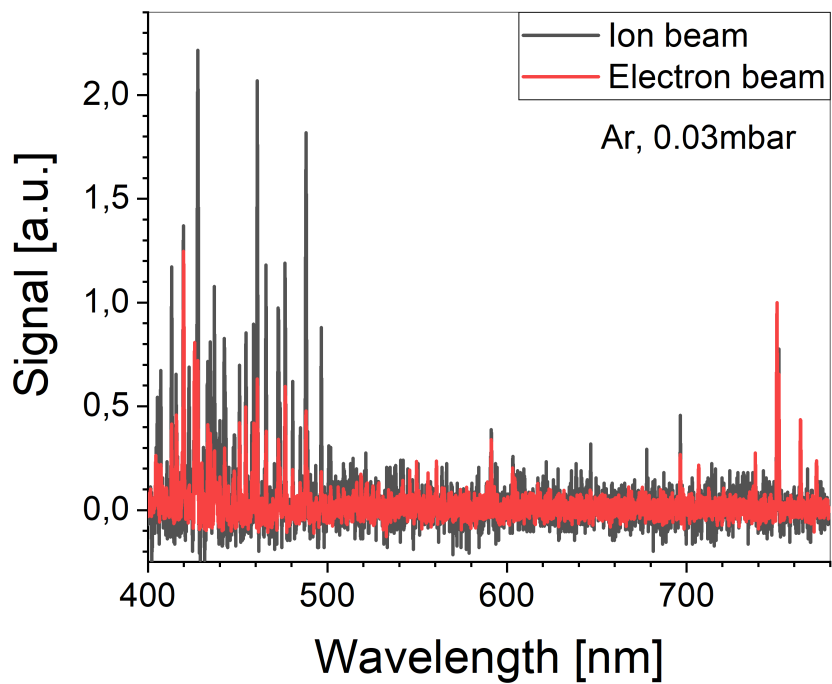


Figure 3.3: Comparison of wavelength spectra in argon at a pressure of 0.03mbar. In black the emission spectrum induced by a sulfur ion beam (87MeV particle energy) and in red the emission spectrum induced by an electron beam (10keV particle energy) is shown. The differences in the relative intensities in the region of ionic transitions (400 to 500nm) are clearly visible.

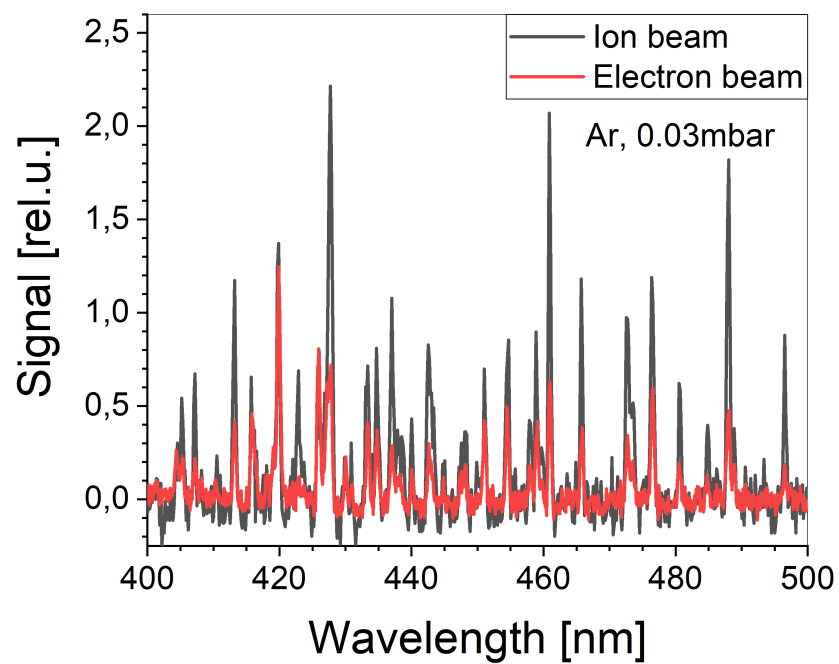


Figure 3.4: Zoom into the wavelength between 400 and 500nm of Figure 3.3. This shows the region in which mostly ionic light emission occurs. It is clearly visible that the relative intensities are much larger in the case of ion beam excitation compared to the excitation by electron beam.

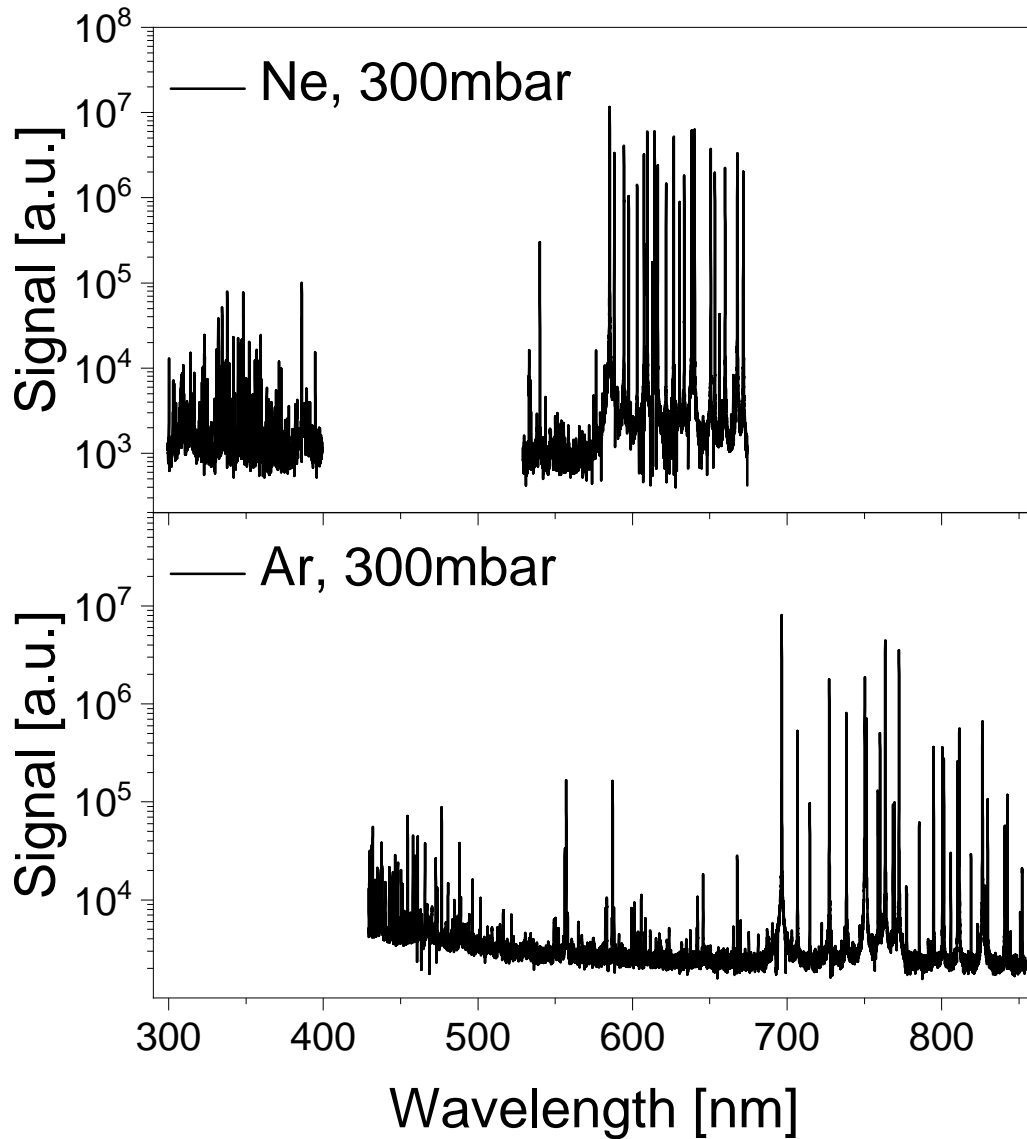


Figure 3.5: Overview spectra of the sulfur ion beam induced light emission for the target gases neon and argon at a pressure of 300mbar. The signal is plotted logarithmically. In both cases the wavelength resolution is  $\Delta\lambda = 0.15nm$ . A bunch of ionic lines can be seen in the shorter wavelength region, the atomic emission lines in the region of longer wavelength. The signal is the count rate of the PMT. The wavelength dependence of the sensitivity is not included in the spectra.

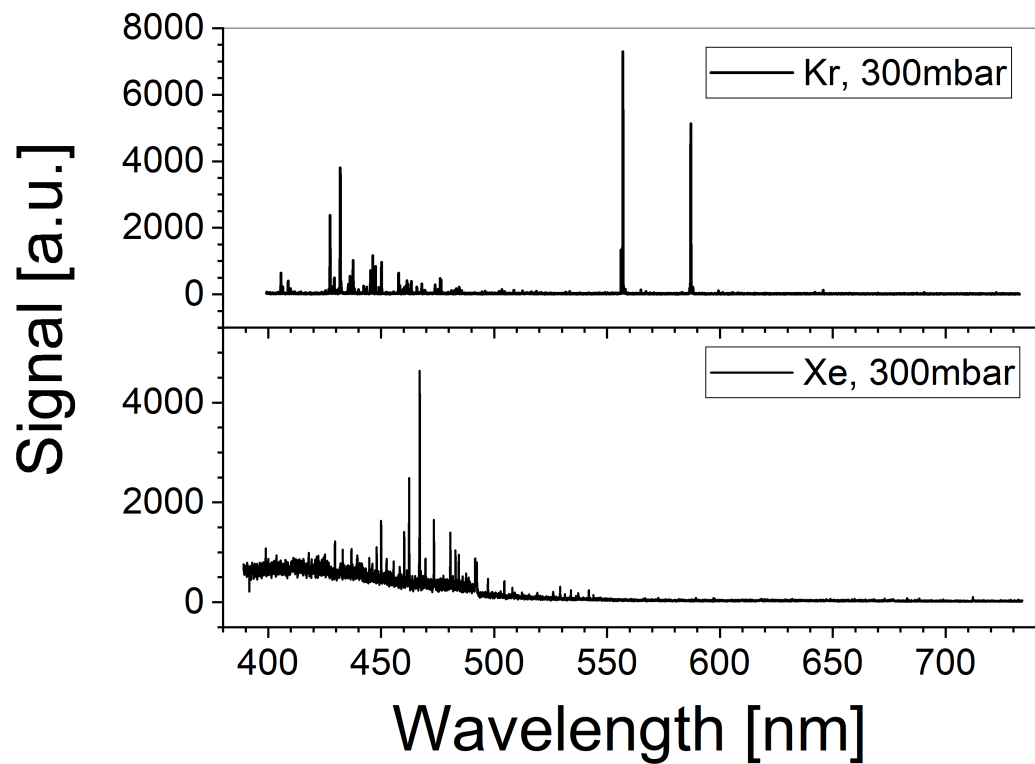


Figure 3.6: Overview spectra of the sulfur ion beam induced light emission for the target gases krypton and xenon at a pressure of 300mbar. In both cases the wavelength resolution is  $\Delta\lambda = 0.15nm$ .

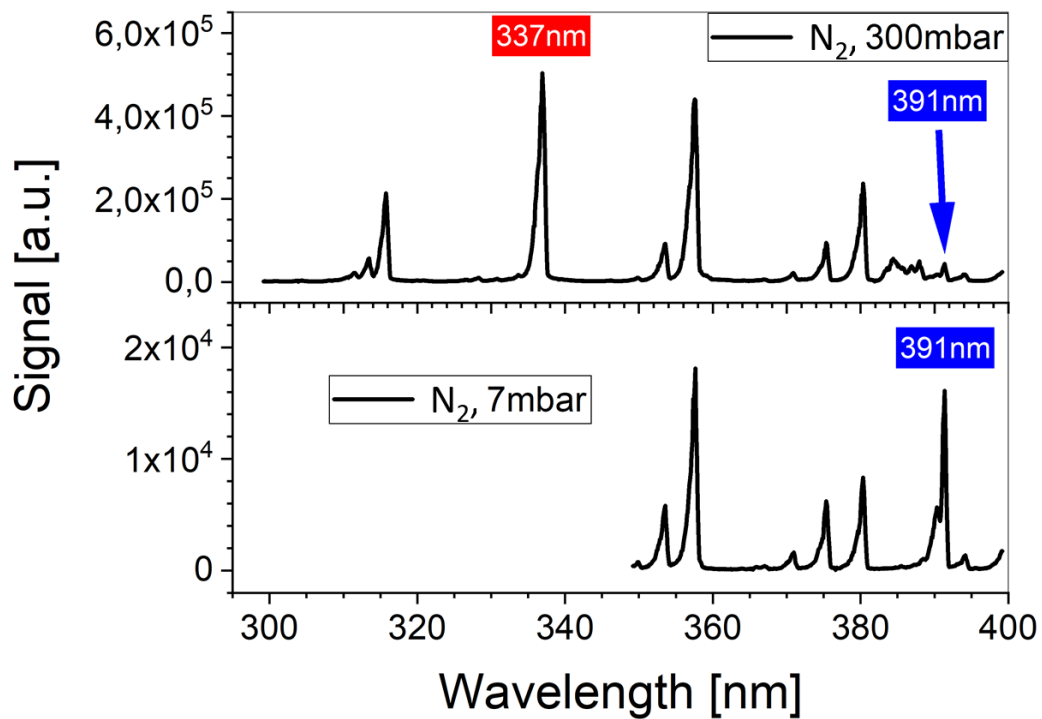


Figure 3.7: Overview spectra of the sulfur ion beam induced light emission from nitrogen at 300mbar and 7mbar. The 337nm C-B emission band (red box) from the neutral molecules is well visible at 300mbar. The ionic molecular emission band around 391nm (blue box) is suppressed but becomes relatively stronger at lower pressures (here 7mbar). In both cases the wavelength resolution is  $\Delta\lambda = 0.6nm$ .

the emission lines in the respective target gas. Emission from neutral and ionic target species can be found in the spectra. Here we worked only with lines emitted from neutral and singly ionized atoms. They will be called atomic lines and ionic lines, respectively. The ionic lines can be seen in the shorter wavelength region between 300 and 400nm for neon and between 400 and 500nm in the case of argon, while the atomic lines appear at longer wavelengths between 580 and 680nm for neon and between 695 and 850nm in the case of argon. At this pressure of 300mbar the ionic lines are two orders of magnitude weaker compared to the atomic lines. Hence, the light emission is dominated by the atomic lines.

### Identification of emission lines

Figure 3.8 and 3.9 show a zoom into the wavelength regions of ionic and atomic light emission in argon, respectively. Due to the good resolution of the spectroscopic setup of 0.06nm, the emission lines can clearly be identified. A selection of lines are shown with their respective wavelength values in Figure 3.8 and 3.9. The blue boxes denote ionic emission lines the red boxes atomic emission lines. An assignment of these lines is shown in Table 3.1. The selected ionic argon lines in Figure 3.8 are all  $3s^23p^44p \rightarrow 3s^23p^44s$  transitions. The two atomic lines labeled in this figure are both  $5p \rightarrow 4s$  transitions. Figure 3.9 shows only  $3s^23p^54p \rightarrow 3s^23p^54s$  transitions. In Figure 3.10 the region of the mainly ionic emission lines of neon can be seen. The ionic lines labeled (blue boxes) are all  $2s^22p^43p \rightarrow 2s^22p^43s$  transitions, the only atomic line labeled (red box) is a  $2s^22p^54p \rightarrow 2s^22p^53s$  transition. The region of atomic emission lines is shown in Figure 3.11. All lines are emitted by  $2s^22p^53p \rightarrow 2s^22p^53s$  transitions. Table 3.2 lists the main emission lines and the respective transitions.

### Pressure dependence of the wavelength spectra

Figure 3.12 shows how the spectra evolve towards lower pressures. At 3mbar the intensity of the light emission from ionic lines is comparable with the emission from the atomic lines. At a pressure of 0.03mbar the ionic lines already dominate the spectra for both target gases.

At a pressure of 300mbar secondary electrons in argon deposit 66% of their energy within a  $23\mu m$  radius and within  $42\mu m$  in neon (derived from calculations by M. Toulemonde and A. Himpsl [42] and [40] by scaling with density from liquid rare gases to the gas phase, see section 3.3). Thus the electrons deposit their energy mostly within the shape of the original ion beam. Since the excitation via secondary electrons dominates, almost only light emission

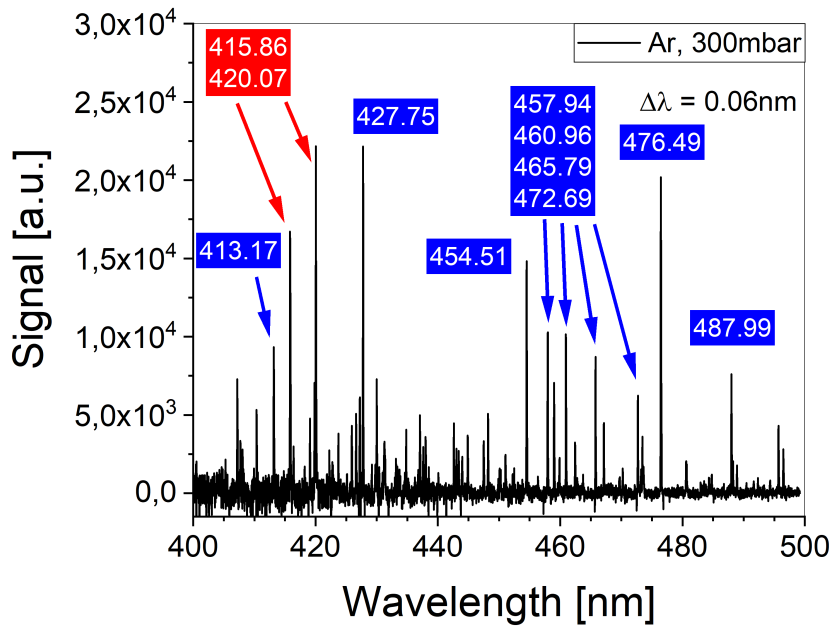


Figure 3.8: More detailed view of the wavelength region of mostly ionic emission lines from argon. The selected ionic argon lines (blue boxes) are all  $3s^23p^44p \rightarrow 3s^23p^44s$  transitions. The two atomic lines (red boxes) in this figure are both  $5p \rightarrow 4s$  transitions. The selected lines are listed in Table 3.1.

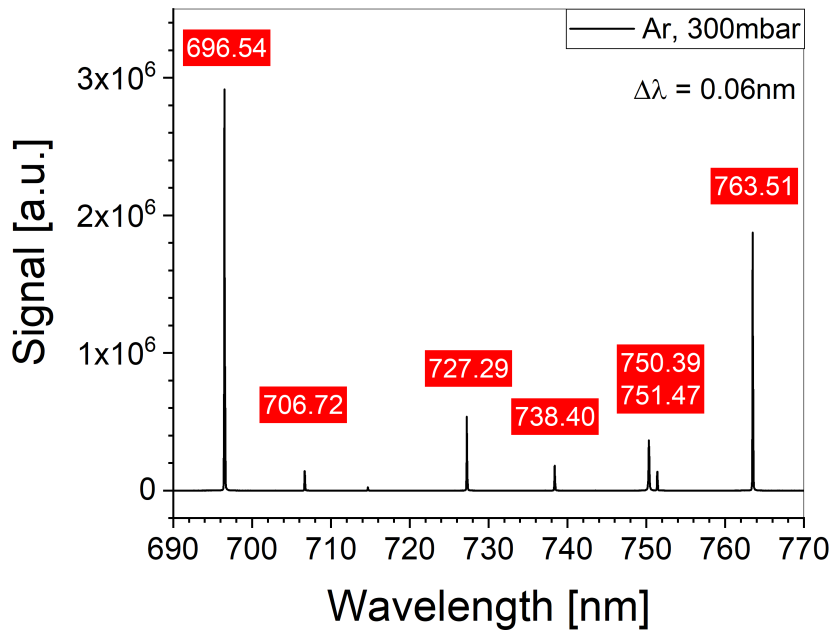


Figure 3.9: Wavelength region of the atomic emission from argon. The spectrum shows only atomic emission (red boxes) from  $3s^23p^54p \rightarrow 3s^23p^54s$  transitions. The selected lines are listed in Table 3.1.

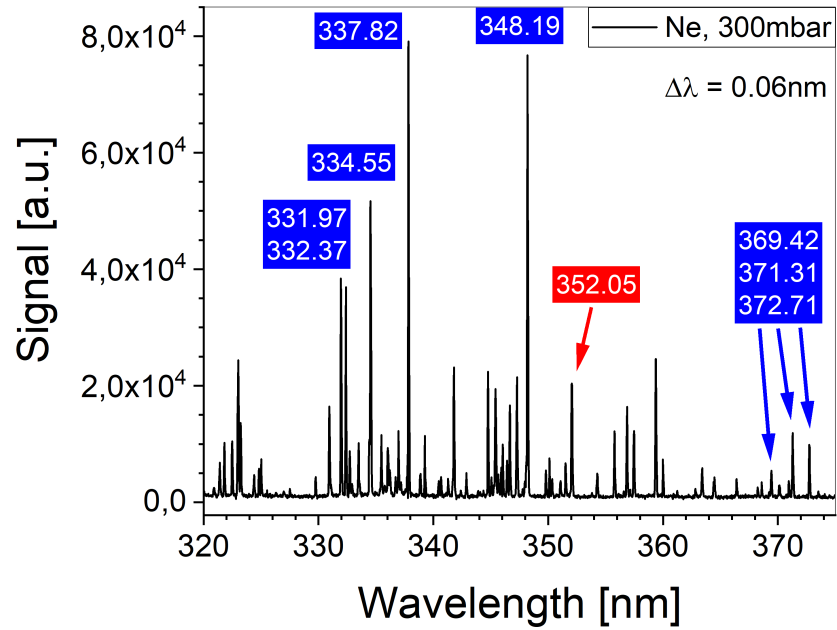


Figure 3.10: Wavelength region of the ionic emission from neon. The ionic lines labeled (blue boxes) are all  $2s^22p^43p \rightarrow 2s^22p^43s$  transitions, the only atomic line labeled (red box) is a  $2s^22p^54p \rightarrow 2s^22p^53s$  transition. The selected lines are listed in Table 3.2.

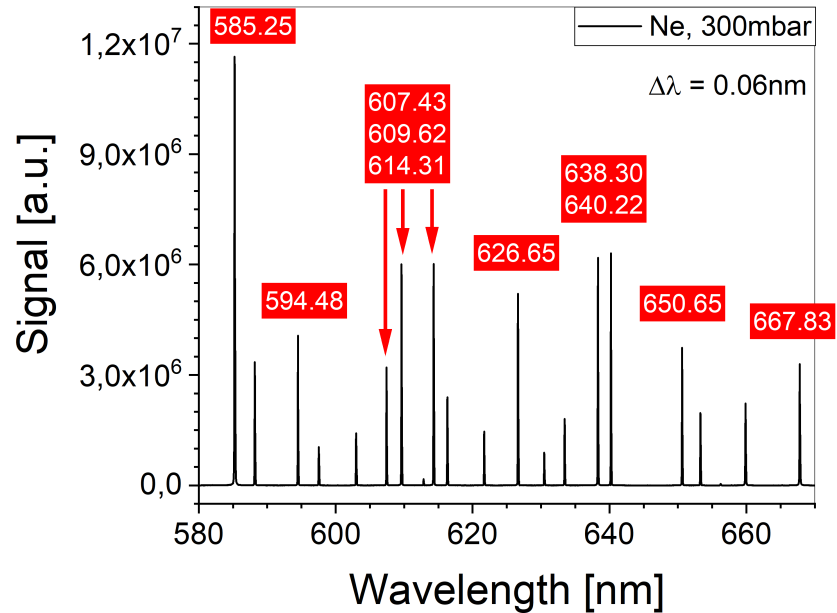


Figure 3.11: Wavelength region of the atomic emission from neon. All selected lines (red boxes) are emitted from  $2s^22p^53p \rightarrow 2s^22p^53s$  transitions. The selected lines are listed in Table 3.2.

$\lambda$	Lower Level [eV]	Higher Level [eV]	Transition	J	Resonance Line [nm]
407.20	18.45	21.50	$4s' \ ^2D - 4p' \ ^2D^0$	5/2 - 5/2	67.185
410.38	19.68	22.70	$4p \ ^2D^0 - 5s \ ^2P$	5/2 - 3/2	x
410.39	19.49	22.51	$4p \ ^4D^0 - 5s \ ^4P$	7/2 - 5/2	x
413.17	18.43	21.43	$4s' \ ^2D - 4p' \ ^2P^0$	3/2 - 1/2	67.286
415.86	11.55	14.53	$4s [1 \ ^1/2]^0 - 5p [1 \ ^1/2]$	2 - 2	x
420.07	11.55	14.50	$4s [1 \ ^1/2]^0 - 5p [2 \ ^1/2]$	2 - 3	x
427.75	18.45	21.35	$4s' \ ^2D - 4p' \ ^2P^0$	5/2 - 3/2	67.185
454.50	17.14	19.87	$4s \ ^2P - 4p \ ^2P^0$	3/2 - 3/2	72.336
457.93	17.26	19.97	$4s \ ^4P - 4p \ ^2S^0$	1/2 - 1/2	71.809
460.96	18.45	21.14	$4s' \ ^2D - 4p' \ ^2F^0$	5/2 - 7/2	67.185
465.79	17.14	19.80	$4s \ ^2P - 4p \ ^2P^0$	3/2 - 1/2	72.336
472.69	17.14	19.76	$4s \ ^2P - 4p \ ^2D^0$	3/2 - 3/2	72.336
476.49	17.26	19.87	$4s \ ^2P - 4p \ ^2P^0$	1/2 - 3/2	71.809
487.99	17.14	19.68	$4s \ ^2P - 4p \ ^2D^0$	3/2 - 5/2	72.336
495.68	13.08	15.58	$4p [2 \ ^1/2] - 9d [3 \ ^1/2]$	3 - 4	72.336
496.51	17.26	19.76	$4s \ ^2P - 4p \ ^2D^0$	1/2 - 3/2	71.809
696.54	11.55	13.33	$4s [1 \ ^1/2]^0 - 4p' [1/2]$	2 - 1	x
706.72	11.55	13.30	$4s [1 \ ^1/2]^0 - 4p' [1 \ ^1/2]$	2 - 2	x
727.29	11.62	13.33	$4s [1 \ ^1/2]^0 - 4p' [1/2]^0$	1 - 1	106.67
738.40	11.62	13.30	$4s [1 \ ^1/2]^0 - 4p' [1 \ ^1/2]$	1 - 2	106.67
750.39	11.83	13.48	$4s' [1/2]^0 - 4p' [1/2]$	1 - 0	104.82
751.47	11.62	13.27	$4s [1 \ ^1/2]^0 - 4p [1/2]$	1 - 0	106.67
763.51	11.55	13.17	$4s [1 \ ^1/2]^0 - 4p [1 \ ^1/2]$	2 - 2	x

Table 3.1: The main emission lines in argon observed in the experiment[33] [34].

$\lambda$	Lower Level [eV]	Higher Level [eV]	Transition	J	Resonance Line [nm]
330.97	27.78	31.53	$3s \ ^2P - 3p \ ^2P^0$	3/2 - 1/2	44.626
331.97	30.55	34.28	$3s' \ ^2D - 3p' \ ^2P^0$	3/2 - 1/2	40.584
332.37	27.78	31.51	$3s \ ^2P - 3p \ ^2P^0$	3/2 - 3/2	44.626
334.55	30.55	34.25	$3s' \ ^2D - 3p' \ ^2P^0$	5/2 - 3/2	44.585
337.82	27.86	31.53	$3s \ ^2P - 3p \ ^2P^0$	1/2 - 1/2	44.504
348.19	27.78	31.34	$3s \ ^2P - 3p \ ^2S^0$	3/2 - 1/2	44.626
352.05	16.85	20.37	$3s' \ [1/2]^0 - 4p' \ [1/2]$	1 - 0	73.590
356.85	30.55	34.02	$3s' \ ^2D - 3p' \ ^2F^0$	5/2 - 7/2	44.585
359.42	31.36	34.81	$3p \ ^4S^0 - 3d \ ^4P$	3/2 - 1/2	x
369.42	27.17	30.52	$3s \ ^4P - 3p \ ^4P^0$	5/2 - 5/2	45.635
371.31	27.78	31.12	$3s \ ^2P - 3p \ ^2D^0$	3/2 - 5/2	44.626
372.71	27.86	31.18	$3s \ ^2P - 3p \ ^2D^0$	1/2 - 3/2	44.504
585.25	16.85	18.96	$3s' \ [1/2]^0 - 3p' \ [1/2]$	1 - 0	73.590
594.48	16.62	18.70	$3s \ [1 \ ^1/2]^0 - 3p' \ [1 \ ^1/2]$	2 - 2	x
607.43	16.67	18.71	$3s \ [1 \ ^1/2]^0 - 3p \ [1/2]$	1 - 0	74.372
609.62	16.67	18.70	$3s \ [1 \ ^1/2]^0 - 3p' \ [1 \ ^1/2]$	1 - 2	74.372
614.31	16.62	18.63	$3s \ [1 \ ^1/2]^0 - 3p \ [1 \ ^1/2]$	2 - 2	x
626.65	16.71	18.69	$3s' \ [1/2]^0 - 3p' \ [1 \ ^1/2]$	0 - 1	x
630.48	16.67	18.63	$3s \ [1 \ ^1/2]^0 - 3p \ [1 \ ^1/2]$	1 - 2	74.372
633.44	16.62	18.57	$3s \ [1 \ ^1/2]^0 - 3p \ [2 \ ^1/2]$	2 - 2	x
638.30	16.67	18.61	$3s \ [1 \ ^1/2]^0 - 3p \ [1 \ ^1/2]$	1 - 1	74.372
640.22	16.62	18.55	$3s \ [1 \ ^1/2]^0 - 3p \ [2 \ ^1/2]$	2 - 3	x
650.65	16.67	18.57	$3s \ [1 \ ^1/2]^0 - 3p' \ [2 \ ^1/2]$	1 - 2	74.372
667.83	16.85	18.70	$3s' \ [1/2]^0 - 3p' \ [1 \ ^1/2]$	1 - 2	73.590

Table 3.2: The main emission lines in neon observed in the experiment [33] [34].

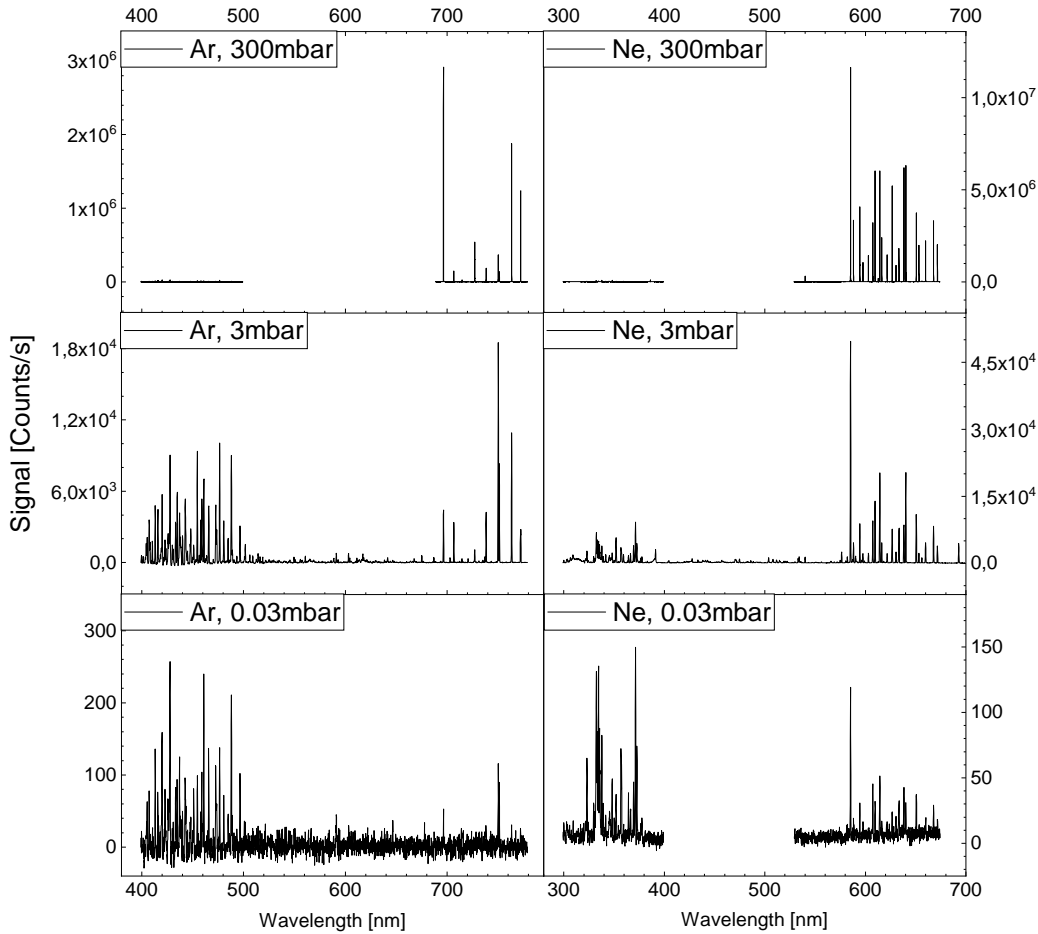


Figure 3.12: Wavelength spectra of Argon (left) and Neon (right) at three different pressures. For both target gases the neutral emission lines dominate at 300mbar. At lower pressures like 0.03mbar the ionic lines dominate. Excitation induced by 87 MeV sulfur ions. See text for an interpretation.

induced by electron excitation can be observed in the spectra.

At 3mbar the Himpsl-Radius is 2.3mm for argon and 4.2mm for neon. This means that many of the secondary electrons can leave the region of the ion beam (radius 0.5mm). With further decreased pressure of 0.03mbar the Himpsl-Radius for argon is 23cm and for neon it is 42cm. Here the excitation by secondary electrons in the region of the ion beam, on which the spectrometer is focused on, is negligibly small.

For several selected lines the integrated intensity values under the emission lines is plotted versus pressure in order to get a quantitative picture of the pressure dependence of those lines. Figure 3.13 shows this for argon. As

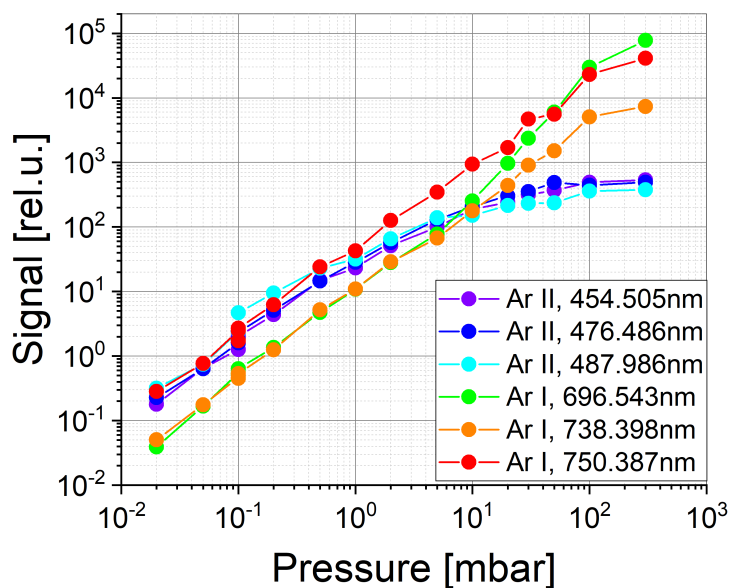


Figure 3.13: Signal from various spectral lines of argon in dependence of pressure. The data is excerpted from the wavelength spectra. The lines in purple, blue and light blue show ionic emission lines, in green, orange and red atomic emission lines are shown. Both types of lines show similar behavior for pressures below 10mbar. Above 10mbar the ionic lines are suppressed due to quenching effects while the atomic lines increase further.

it was already observed in the wavelength spectra the atomic emission lines dominate for higher pressures. For pressures below 10mbar both types of emission lines, ionic and atomic, show a similar behavior with pressure. From 10mbar upwards the signal of the atomic lines increases much stronger than the increase of the signal of the ionic lines. The ionic lines are suppressed by quenching effects due to radiationless de-excitation such as de-excitation in collisions. Recombination mostly occurs when singly charged ions trap a free electron resulting in an excited atom. The de-excitation of those atoms leads to an additional contribution to the atomic light emission. Since two-fold or further ionized target species have a much lower density, the contribution of recombination to the ionic light emission is rather small (see Section 3.2). Furthermore atoms are excited by secondary electrons as well. At high pressures this excitation has a large contribution to the light emission due to the very short range of the secondary electrons at those pressures.

It is interesting to see that the strongest spectral line of argon, the line at 696.54nm becomes the weakest of the selected lines at lower pressures. Here the strongest atomic line is at 750.39nm. Other than the lines at 738.40nm or 750.39nm the transition of the 696.54nm line ends on a level with no transition to the ground state. In fact the lower level of the transition of the

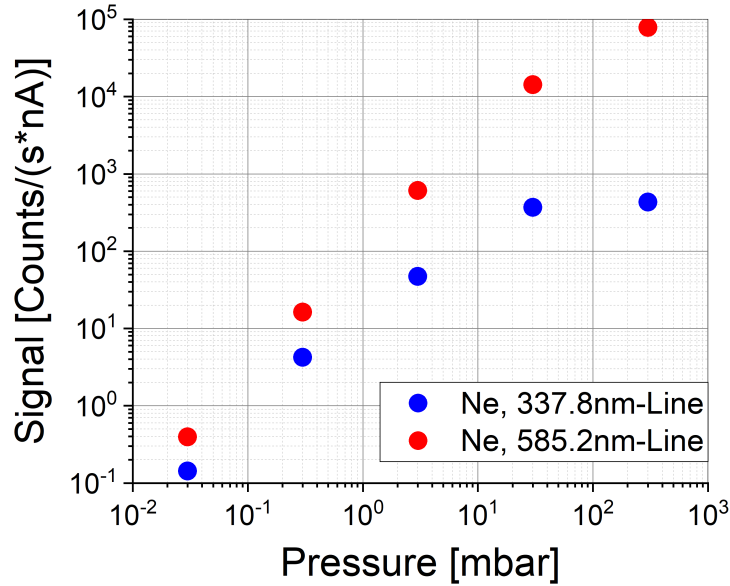


Figure 3.14: Signal from the main ionic and atomic lines respectively plotted versus pressure. The behavior is similar to the one observed in argon (see Figure 3.13). The ionic line is suppressed at higher pressures due to quenching.

738.40nm and 750.39nm lines is a resonance level.

Figure 3.14 shows the Signal versus pressure for neon for one atomic line (585.25nm) and one ionic line (337.82nm). The diagram shows the same behavior with pressure as in the case of argon.

Bending of the intensity curves is observed in the case of the ionic emission lines. This bending is due to the larger cross-section of the ions for collisions. In those collisions the radiationless de-excitation of the excited ions can occur, which results in the quenching of the ionic light emission. Quenching due to collisions requires higher particle densities in order to have a significant effect on the light emission, therefore, this effective quenching is observed for pressures above 1mbar.

### 3.1.2 Spectroscopic results with electron beam excitation

The work of A. Ulrich in [12] and especially the excitation cross-sections shown in Figure 3.1 inspired the idea to simulate the secondary electrons with a custom-built electron gun manufactured by excitech GmbH (see section 2.7). Here, wavelength spectra of the light emission in both target gases argon and neon were also recorded using electron beam excitation for comparison. This was done to verify the interpretation of the pressure de-

pendence of the excitation mechanisms given in section 3.1.1. The electron gun was mounted in the target chamber and the spectrometer was used with the identical settings as in the case of ion beam excitation. The recorded spectra could then be directly compared to the spectra with ion beam excitation. This is shown in Figure 3.15 and 3.16.

Figure 3.17 and 3.18 show a zoom into the respective wavelengths regions. The same is shown in Figure 3.19 and 3.20 for argon as target gas.

For demonstration purposes the wavelength of the electron beam spectra were shifted slightly in wavelength in the 300mbar spectra, so that the spectral lines are visible next to each other instead of being hidden behind.

With decreasing pressure both target gases show the same behavior: at 300mbar both spectra match well with each other. The light emission in the case of the ion beam excitation has its origin almost exclusively in the excitation by secondary electrons. Thus, the excitation mechanisms are the same as for electron beam excitation. This leads to the essentially identical wavelength spectra for both types of particle beams. Smaller differences at certain lines are due to fluctuations of the beam current of the ion beam.

When decreasing the pressure to 3mbar changes start to show. Secondary electrons from the ion beam largely leave the bulk of the beam. Therefore relatively more of the light emission comes from excitation by heavy ions and so differences in the region of the ionic lines become visible: the lines remain much stronger than in the case of electron beam excitation. This effect intensifies when the pressure is further decreased to 0.03mbar. In case of the atomic lines which are excited both by heavy ions and electrons, the spectra remain very similar throughout the complete pressure range from 300mbar to 0.03mbar. Altogether the intensity of the atomic lines decreases strongly with decreasing pressure.

In order to determine the real profile of the ion beam it seems to be more convenient to look at the ionic emission lines, since those are not excited by secondary electrons and hence map the actual ion beam much better. The atomic lines, however, are excited by heavy ions as well. Indeed the intensity decreases strongly (stronger than for the ionic lines) with decreasing pressure but some lines remain comparably as strong as the strongest ionic lines at low pressure (i.e. 585.2nm-line in neon).

The problem of an artificial broadening of the beam, due to secondary electrons, does not exist at low pressures ( $< 10^{-2}$ mbar), since the range of the electrons is getting much longer. This will be discussed in greater detail in Chapter 3.3.

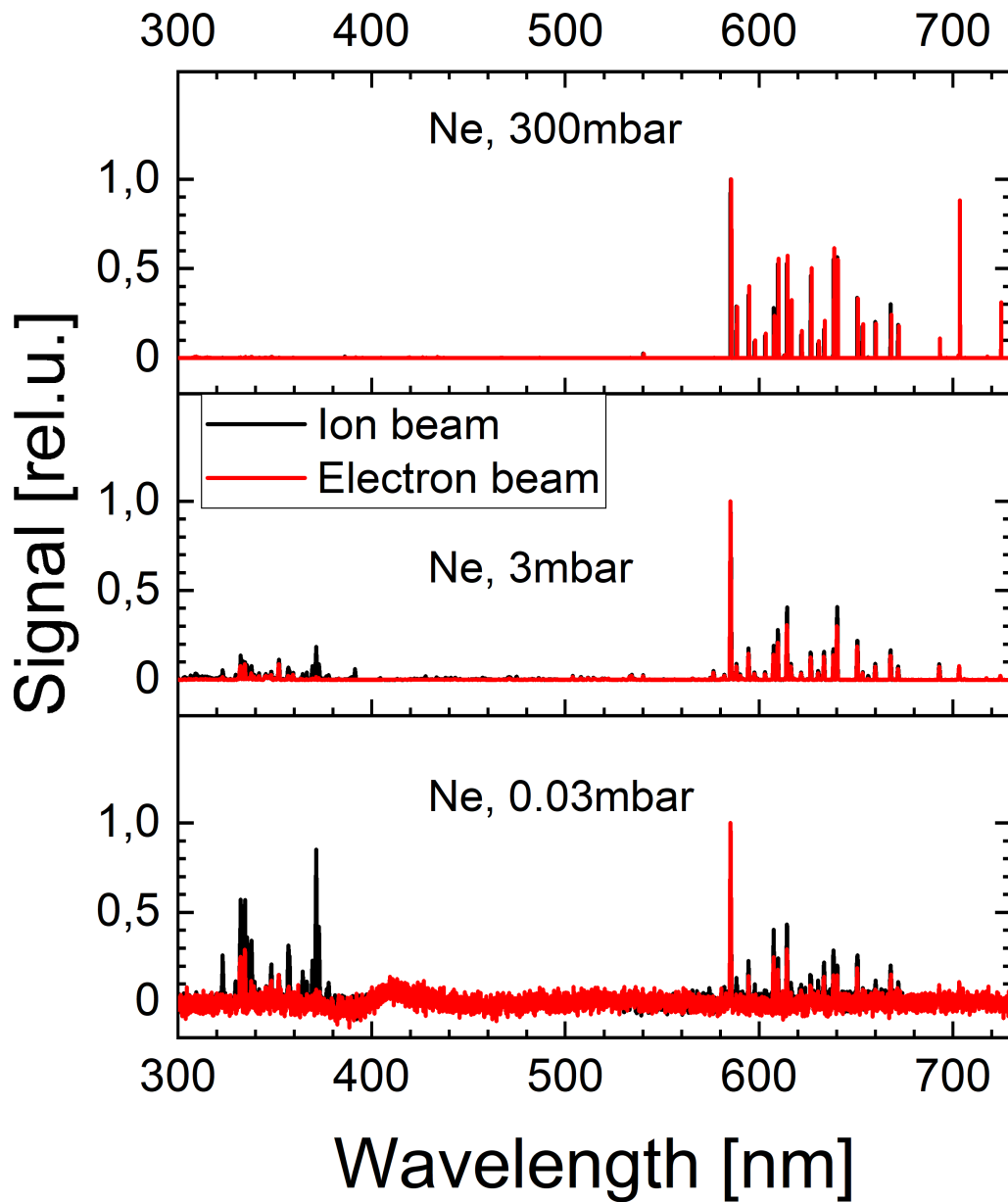


Figure 3.15: Wavelength spectra of the light emission induced by a 87MeV sulfur ion beam compared to the light emission induced by a 10keV electron beam. The spectra were recorded with neon as target gas.

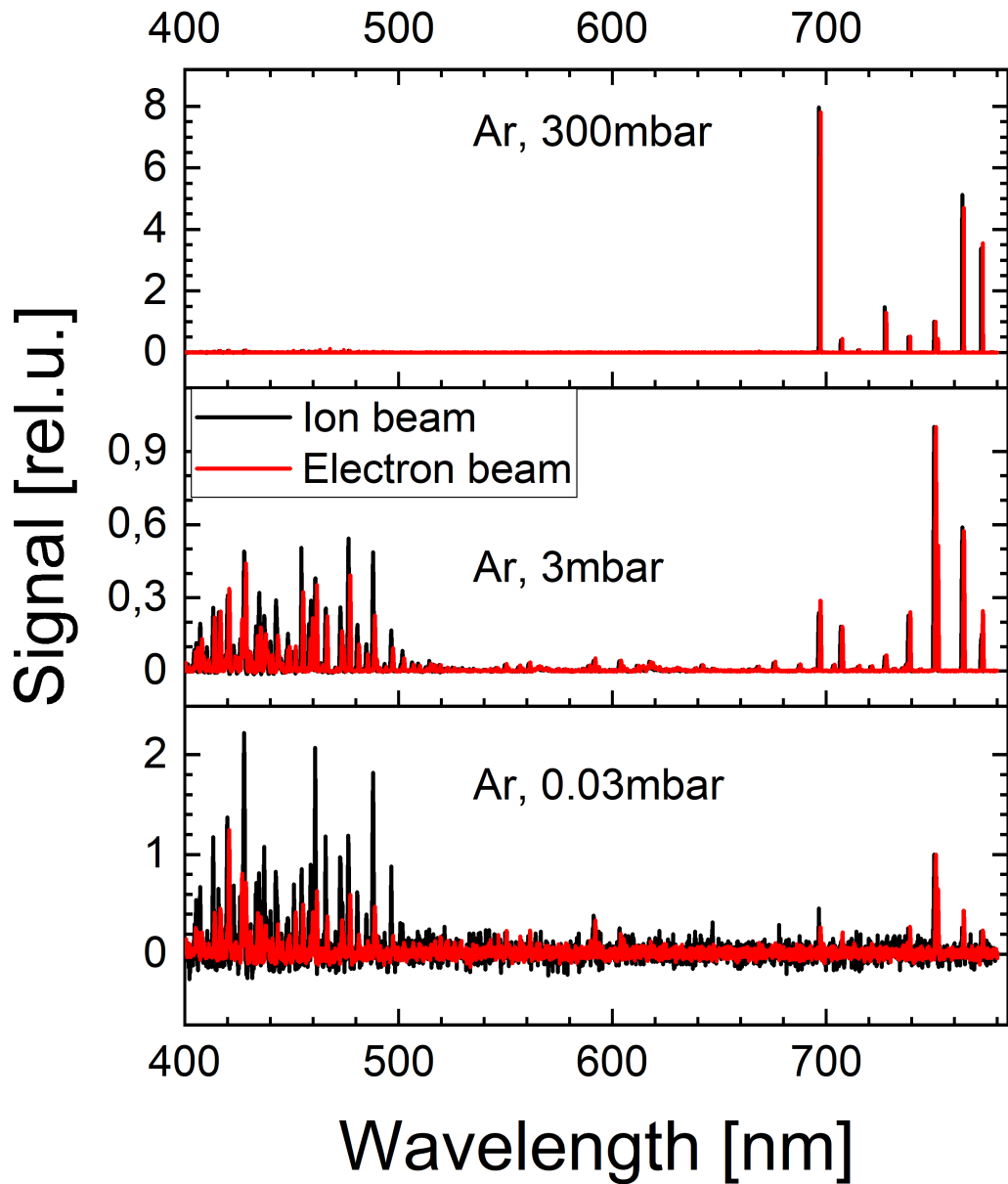


Figure 3.16: Wavelength spectra of the light emission induced by a 87MeV sulfur ion beam compared to the light emission induced by a 10keV electron beam. The spectra were recorded with argon as target gas.

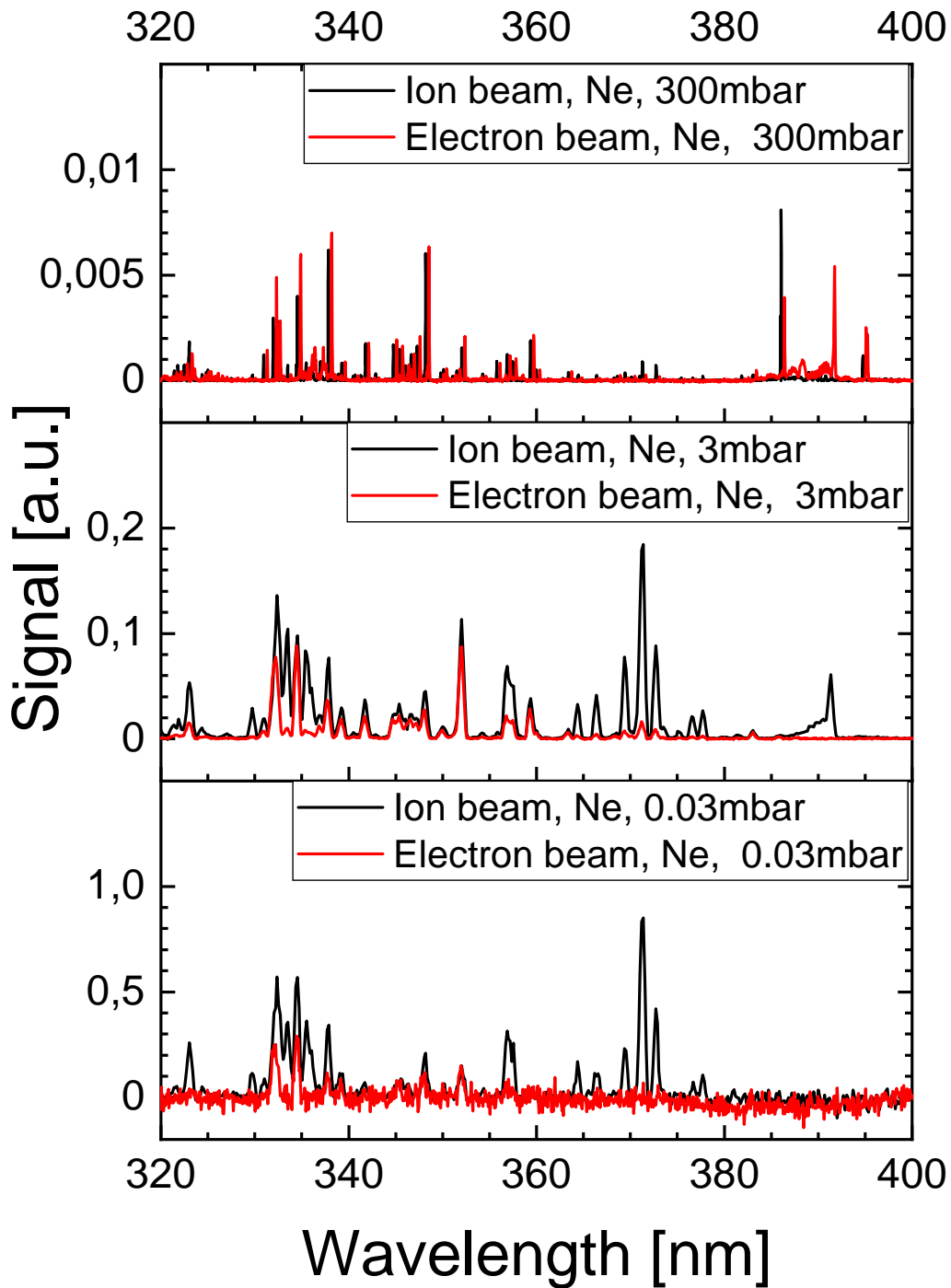


Figure 3.17: Same wavelength spectra as shown in Figure 3.15 for neon but zoomed closer into the regions of interest for the ionic emission region.

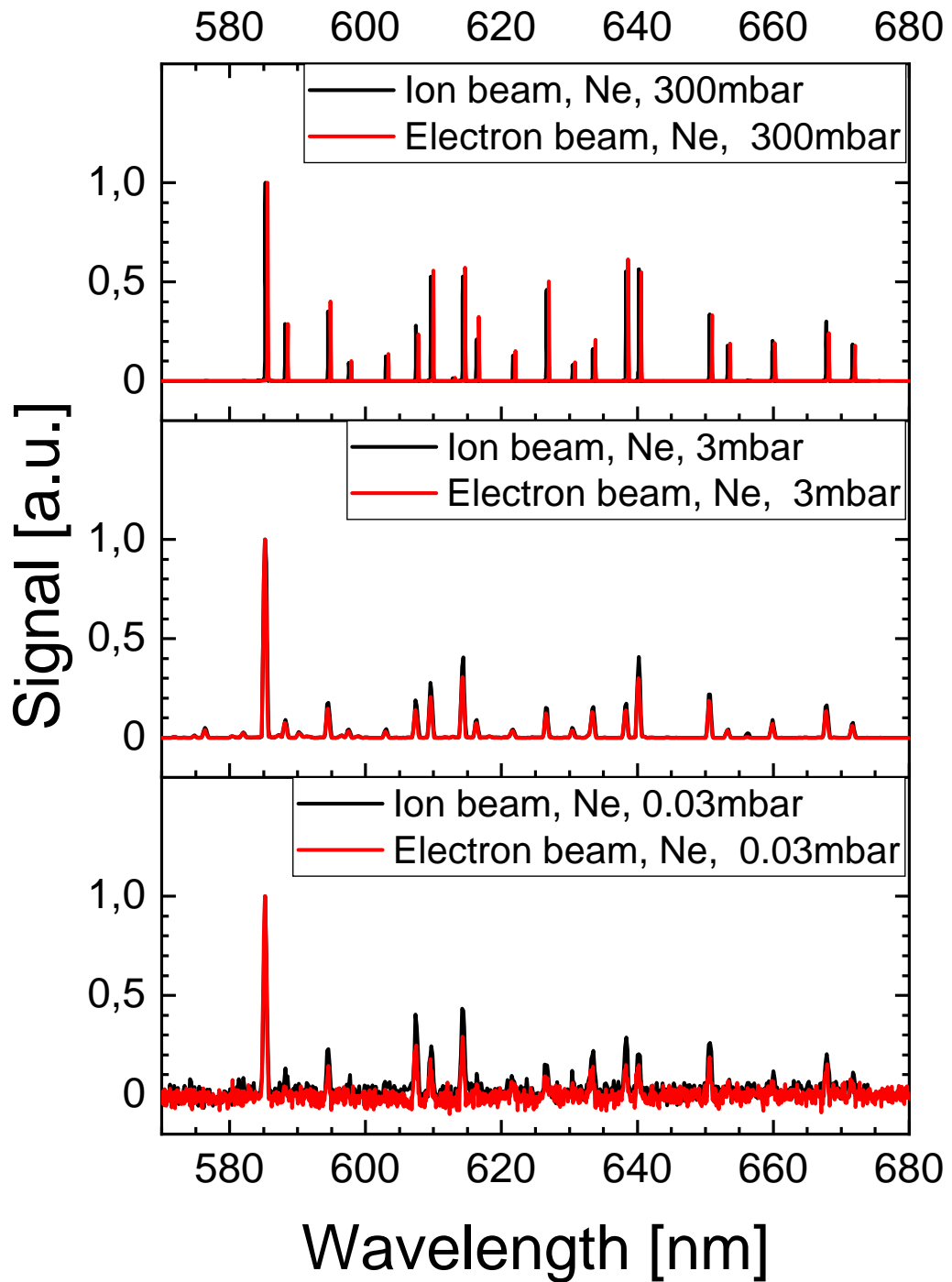


Figure 3.18: Same wavelength spectra as shown in Figure 3.15 for neon but zoomed closer into the regions of interest for the atomic emission region.

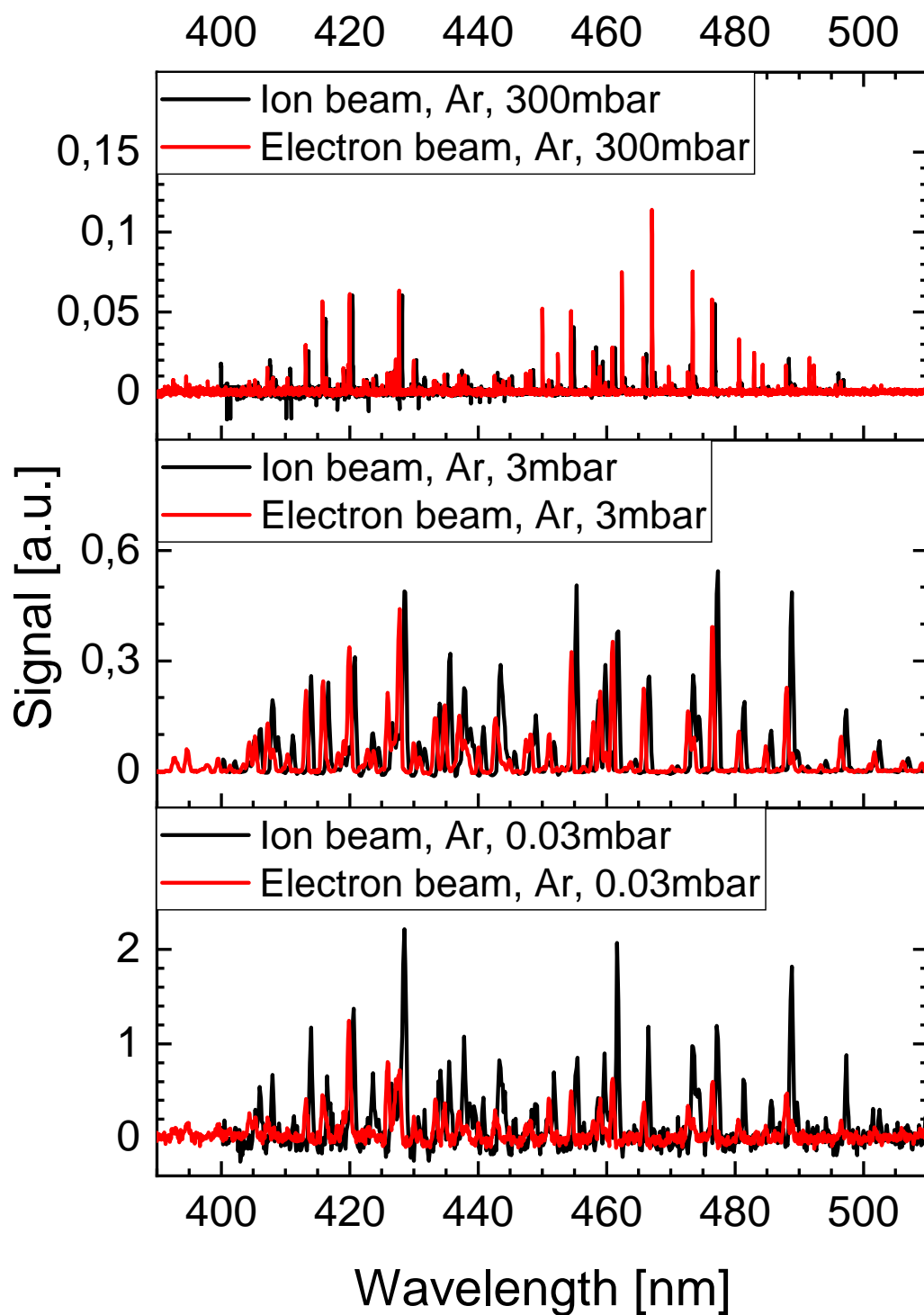


Figure 3.19: Same wavelength spectra as shown in Figure 3.16 for argon but zoomed closer into the regions of interest for the ionic emission region. For display purposes the wavelengths of the electron beam induced spectrum are slightly shifted, so that the lines are visible and not hidden behind each other.

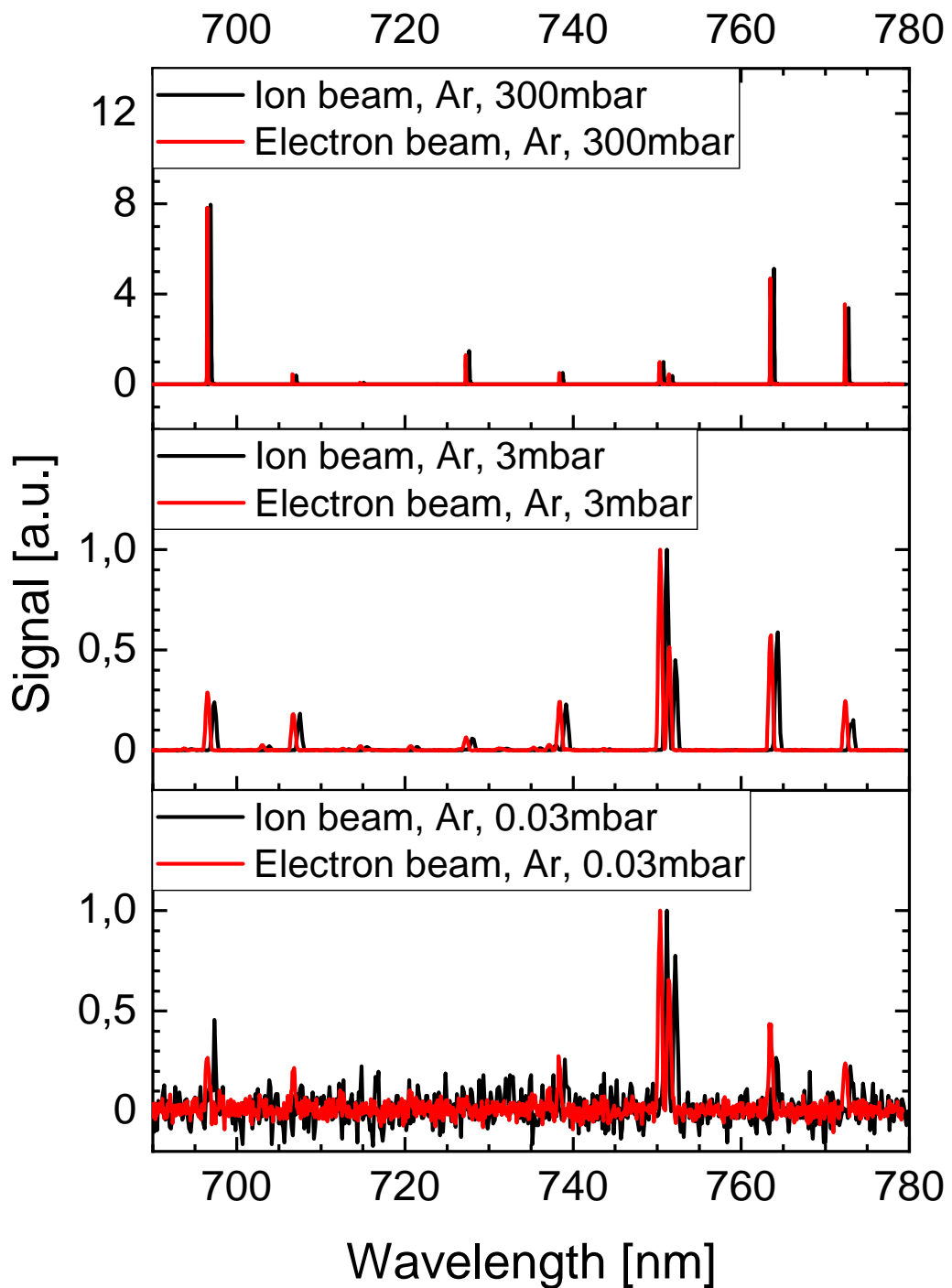


Figure 3.20: Same wavelength spectra as shown in Figure 3.16 for argon but zoomed closer into the regions of interest for the atomic emission region. For display purposes the wavelengths of the electron beam induced spectrum are slightly shifted, so that the lines are visible and not hidden behind each other.

### 3.1.3 Choice of bandpass filters

Two bandpass filters were chosen for each target gas, argon and neon, respectively: one for an ionic line and one for an atomic line. The bandpass filters have a FWHM of 10nm.

Filters with the central wavelength (CWL) of 473nm and 740nm were chosen for argon. The 473nm-filter is for the 476.5nm line, which is one of the strongest ionic lines and remains well visible at low pressures. The 740nm-filter is for the 738.4nm line. In the region of the atomic lines the 696.5nm line appears to be convenient since it is extremely intense at high pressures. But this line almost completely disappears at low pressures. Alternatives are the lines at 738.4nm and 750.4nm, which both and especially the latter remains well visible even at low pressures. The lower levels of both corresponding transitions are resonance levels. The advantage of choosing the 738.4nm line is that it stands alone in the spectrum and thus it is the only line recorded with the according bandpass filter.

For neon the chosen filters have a CWL of 337nm and 589nm, since the lines at 337.8nm and 585.2nm are both at low pressures and at high pressures among the strongest lines in the respective wavelength region. The filters were described in more detail in section 2.6.7.

## 3.2 Time resolved measurements

Different de-excitation mechanisms might result in light emission with the same wavelength (see Figure 3.1). For example in dc-experiment it is not possible to determine from wavelength spectra if there was recombination taking place, under which circumstances and what ratio of the light emission has its origin in recombination. However, recombination followed by de-excitation is a process that requires some time: The incoming projectiles from the heavy ion beam ionizes atoms in the target gas resulting in free electrons drifting through the target gas. On their way through the gas those secondary electrons can get caught by ions. However, this does not occur if the electrons are still too hot, i.e. the electrons are too fast to be trapped by the ions. Hence, recombination is a process that occurs on a microsecond scale. When the ion catches a free electron it turns into an excited atom, which then de-excites either radiationless in collisions or de-excites under the emission of a photon. This photon emission can be detected by the spectroscopic setup.

Time resolved spectra were recorded using a pulsed sulfur ion beam chopped to a puls width of 320ns. The monochromator was kept constantly at the

wavelength of the spectral line that was to be studied. The photons were detected by the same PMT and timed by the CFD. Data taking was performed using a MCS6A-2 multiple-event time digitizer (see Ref. [46]). The MCS6A-2 records spectra measuring the time between the “Start” and the “Stop” signal. The “Start” signal is given by the accelerator (with a certain delay) whenever an ion beam pulse is sent. The “Stop” signal is received from the PMT via the CFD when a photon is detected. The MCS6A-2 is able to process a high rate of incoming signals (10GHz per input channel) for several microseconds before any events are lost.

Figure 3.21 and Figure 3.22 show the results in case of the 696.5nm atomic emission line and the 476.5nm ionic emission line in argon, respectively. The peak at around 10 $\mu$ s shows the prompt light emission induced by the ion beam. Recombination sets in after a cooling time: Once the pulse hits the target gas new electrons are produced and the already existing free electrons in the target gas are heated up as well. Due to the high velocities of the electrons they are much less likely to be caught by ions to recombine. After cooling down, recombination occurs at a much higher rate and the signal increases strongly in the case of higher pressures. This effect is very prominent in the case of the atomic light emission and much smaller in the case of the ionic emission, since the density of singly ionized target atoms is much higher than of further ionized atoms. With further decreased pressure the collisions of electrons with ions occur at a much lower rate resulting in much less recombination.

This result shows that recombination is an important mechanism to be considered and one of the main reasons for the greatly enhanced light emission from atomic transitions compared to ionic transitions as it was observed in section 3.1. Recombination in heavy ion beam induced plasma has been studied and modeled in detail by G. Ribitzki [35]

### 3.3 Beam profiles

It was described in section 2.2 that the ion beam enters the target chamber through a circular hole (diameter 1.0mm) in a tantalum aperture. For pressures of 1mbar and below the pressure in the target chamber is kept constant via differential pumping. This approach reaches its limits at about 1mbar. Therefore, a titanium entry foil is inserted for measurements at 1mbar and above in order to separate the beam line from the target chamber.

Images of the light emission of the ion beam are taken by the cameras. An example is shown in Figure 3.23, with the region of interest (ROI) marked

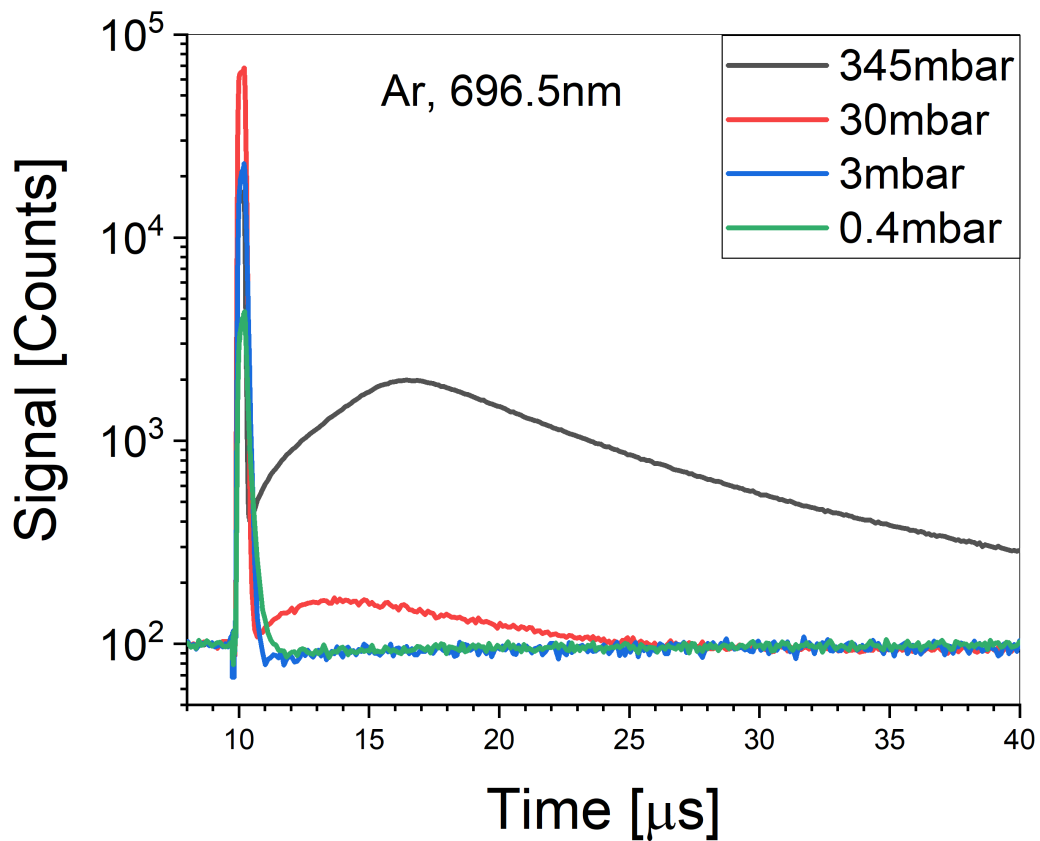


Figure 3.21: Time resolved measurement of the light emission of the Ar I (atomic) emission line at 696.5nm. The initial peak at 10 $\mu$ s shows the pulse of the ion beam. Recombination is observed for pressures of 343mbar and 30mbar (black and red curve, respectively). It shows as a broad increase of the light emission in the microseconds following the pulse of the ion beam.

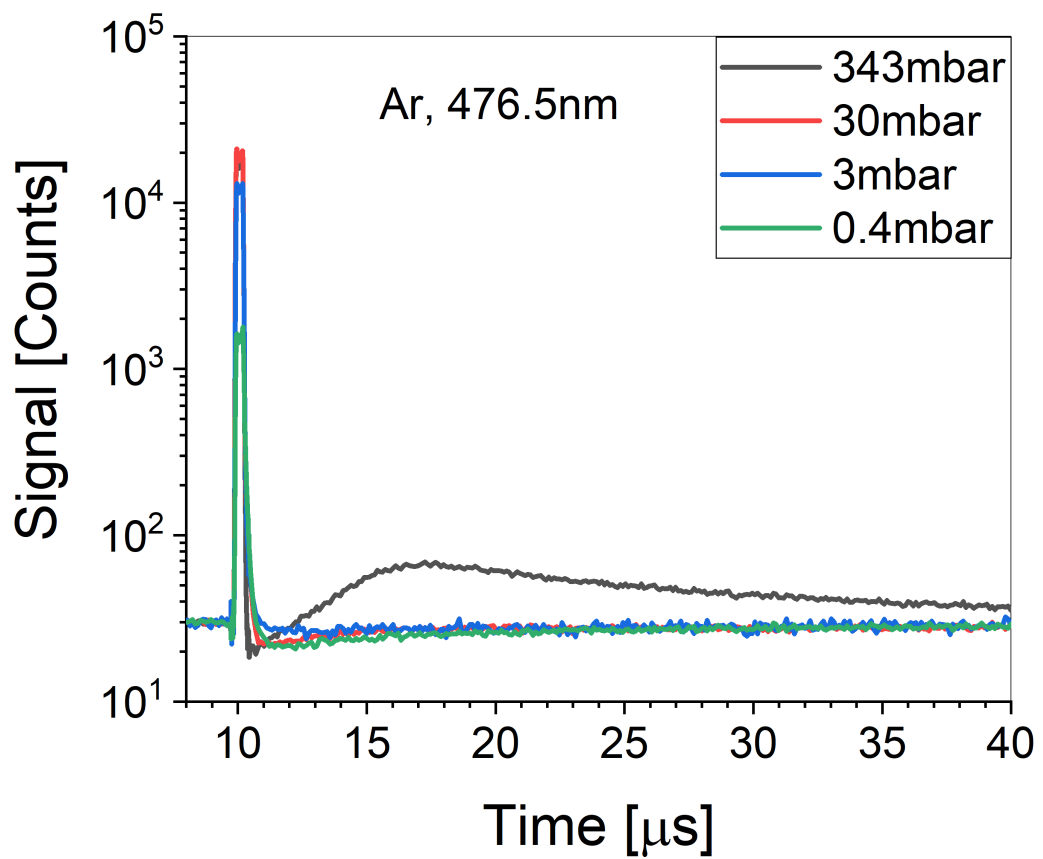


Figure 3.22: Time resolved measurement of the light emission of the Ar II (ionic) emission line at 476.5nm. In comparison to the time spectrum of the atomic line (see Figure 3.21) recombination is not as strong in the case of ionic light emission. Only at a pressure of 343mbar and strong contribution to the light emission is observed (black curve).

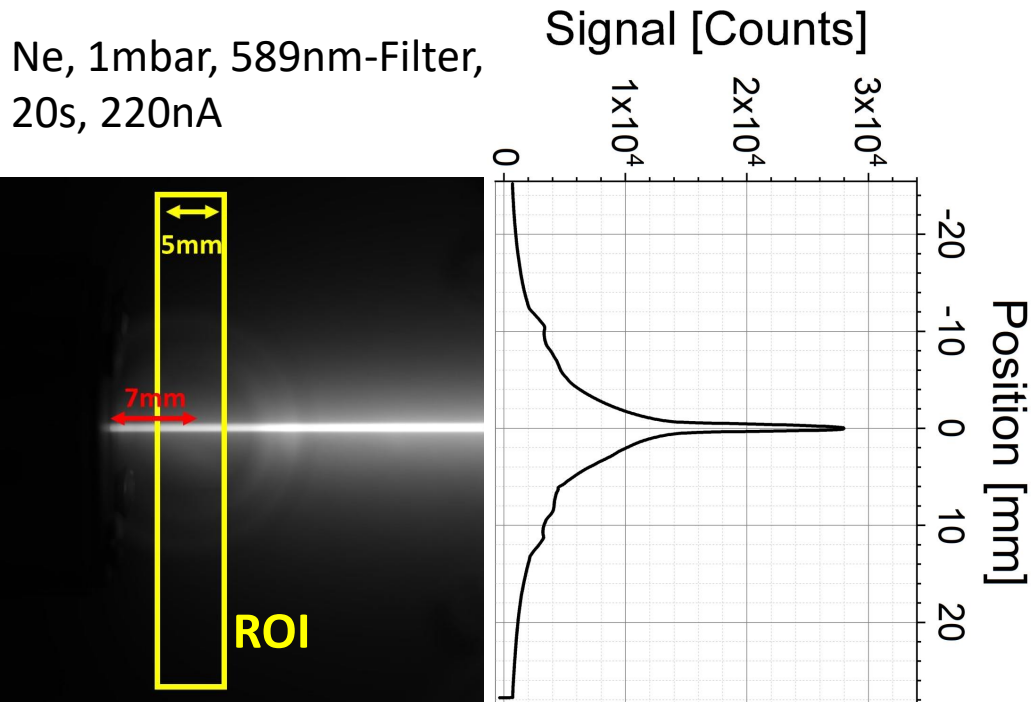


Figure 3.23: Example of an image of the ion beam in neon at 1mbar taken through a 589nm-Filter (left). The region of interest (ROI) is marked by the yellow rectangle. The profile is plotted perpendicular to the beam (right). It has to be noted that the plotted profile is the profile of the projection of the beam into a plain. The values along the position-axis are averaged over the 5mm horizontal direction.

by a yellow rectangle and a plot of the profile. The plot of the profile is a projection of the radial light emission into a plain parallel to the camera sensor plane. An exemplary Abel Inversion of the projection of the beam profile is shown in Figure 3.24. The Abel Inversion reverses the projection of the beam profile if the light emission is azimuthally symmetric and shows the radial beam profile. The algorithm is taken from [41] and slightly edited for the present purpose.

Especially in Figure 3.25, where the peaks are scaled to equal heights, it can be seen that the radial distribution of the light emission is much sharper than its projection. This seems surprising at first glance but can be understood with simple geometrical considerations.

Quite often the beam is cut by the entry aperture and thus not radially symmetrical and thus an Abel Inversion is not constructive especially since it is not necessary for the application. It might be of interest for the accelerator operation to apply an Abel Inversion for the final setting of the beam to obtain the radial beam profile. In the following only the projections of

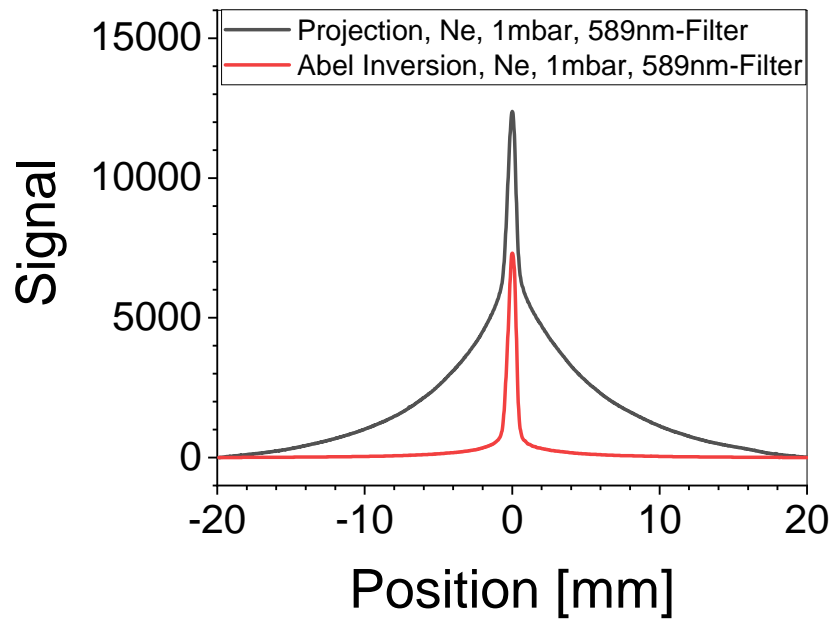


Figure 3.24: Comparison between the projection of the beam profile and the respective Abel Inversion. The Abel Inversion leads to a much thinner original beam profile than the projection suggests.

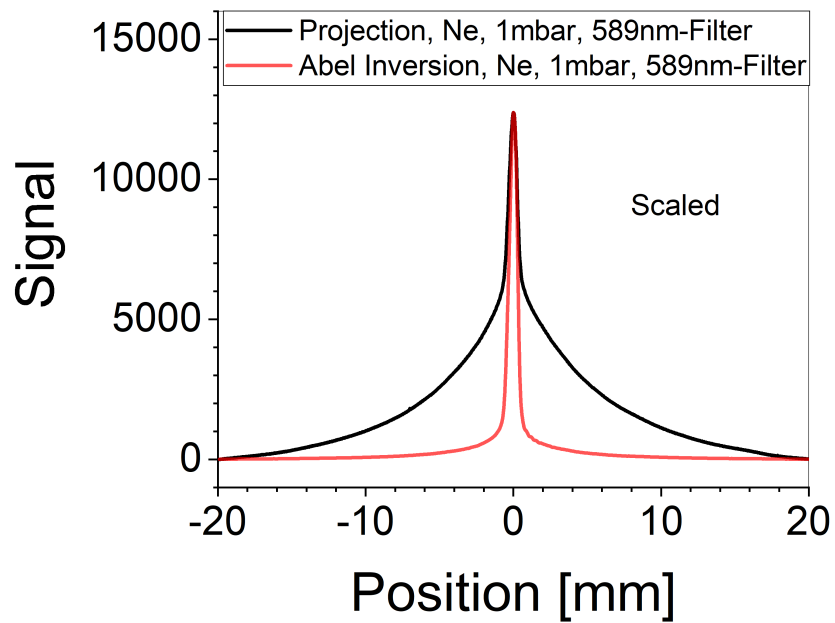


Figure 3.25: Comparison between the projection of the beam profile and the respective Abel Inversion. The profile of the Abel Inversion is scaled to the same peak height as the projection for comparison purposes. The Abel Inversion allows to calculate the radial profile from the projected profile for a circular beam.

the beam profiles will be considered while the Abel Inversion will not be of greater importance.

Figure 3.26 and 3.27 show the beam profiles for both ionic emission lines and atomic emission lines for six different pressures in the target gases argon and neon respectively. The profiles are scaled to a value of 1 at maximum height and the background is subtracted. At higher pressures ( $p > 50\text{mbar}$ ) the profiles match very well. This is the case for 10mbar as well. But especially in the case of neon the atomic light emission shows a slight widening. At 3mbar (neon) and 1mbar (argon) this widening is most prominent and exhibits some kind of a halo around the actual beam profile. At further decreased pressures the halo gets wider and moves outwards, the bulk of the beam shows a sharp profile again, similar to the profile of the ionic emission line. In the pressure region of  $10^{-3}\text{mbar}$  the halo disappears essentially and the central profiles match again.

There is a clear difference between the spatial distribution of the light emission of the ionic transitions compared to the light emission of the atomic transitions. As already stated in section 3.1.1 and described in reference [12], ions are almost exclusively excited by ion beams in single collisions and rarely by electrons, while atoms are excited efficiently by electrons as well. Stepwise ionization and excitation by secondary electrons might be possible for very intense ion beams in higher rates.

Part of the energy of the ion beam is transferred via electronic stopping. The secondary electrons produced in this process move through the target gas with various ranges depending on the pressure and their energies. The energy of those recoiling electrons depends on the velocity of the ions and thus on  $E/m$ . The electron energy distribution is characteristic for the primary ion beam projectiles and the energy deposition by these secondary electrons has to be modeled. According to calculations by M. Toulemonde and A. Himpsl for secondary electrons in liquid argon equation (3.1) applies for the radius within which 66% of the energy is deposited [40] [42]. It will be called ‘‘Himpsl-Radius’’ in the following.

$$r_{E_{depo}}(Ar, liquid) = 4.88nm \cdot \left( \frac{E/MeV}{m/u} \right)^{0.52} \quad (3.1)$$

Scaling this equation to gaseous argon at a temperature of 293K and a pressure of 1mbar leads to

$$r_{Himpsl}(Ar, gas, 293K, 1mbar) = 4.15mm \cdot \left( \frac{E/MeV}{m/u} \right)^{0.52} \quad (3.2)$$

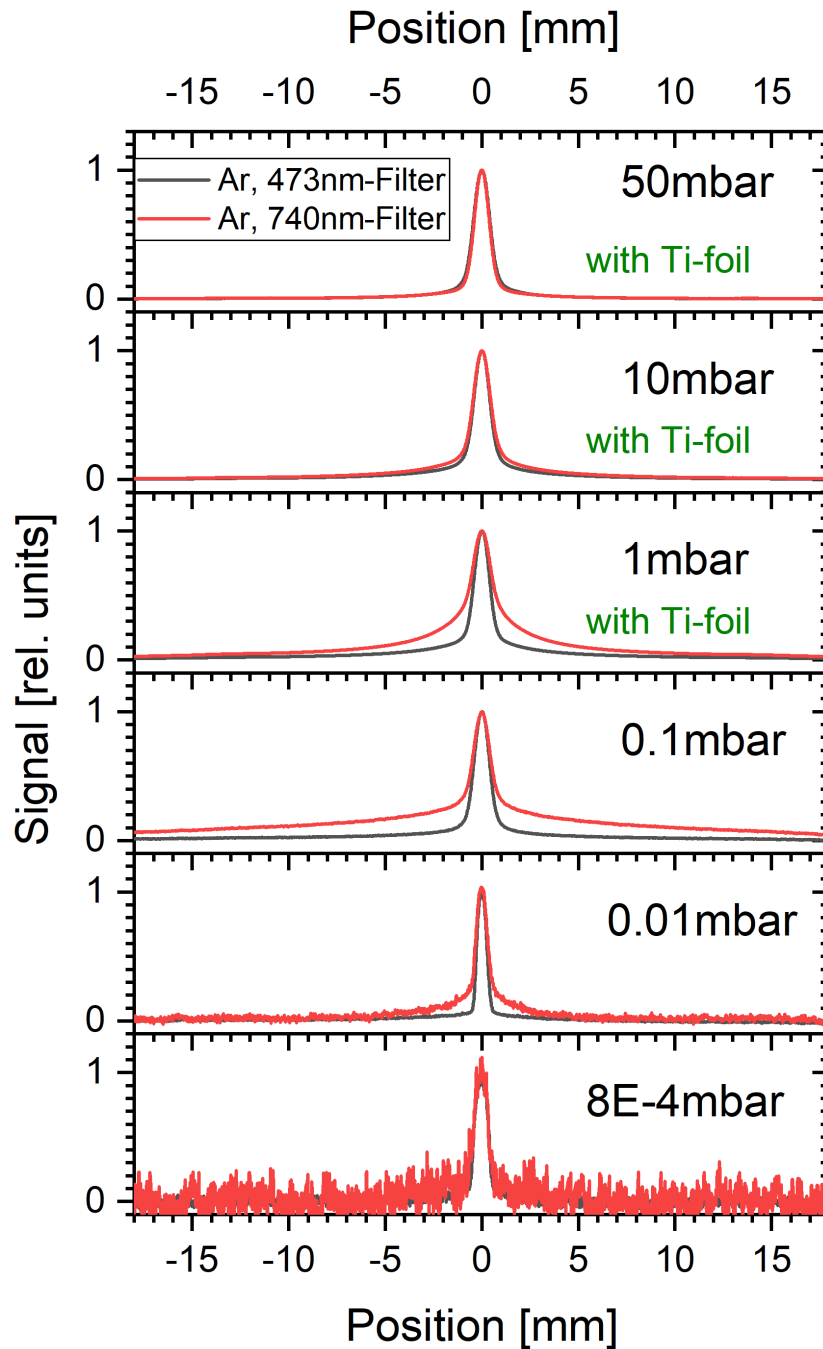


Figure 3.26: Comparison of the beam profiles in argon at various pressures. The sulfur beam has an energy of 87MeV before entering the target chamber. For pressures of 1mbar and above the beam enters the target chamber through an aperture of 1mm diameter and a  $1.1\text{mg}/\text{cm}^2$  Ti entry-foil. The beam energy behind the entry-foil is 74MeV (see 2.1). For pressures below 1mbar the entry-foil is removed and just the aperture remains. The beam profile from the ionic light emission is shown in black, the one from the atomic light emission in red.

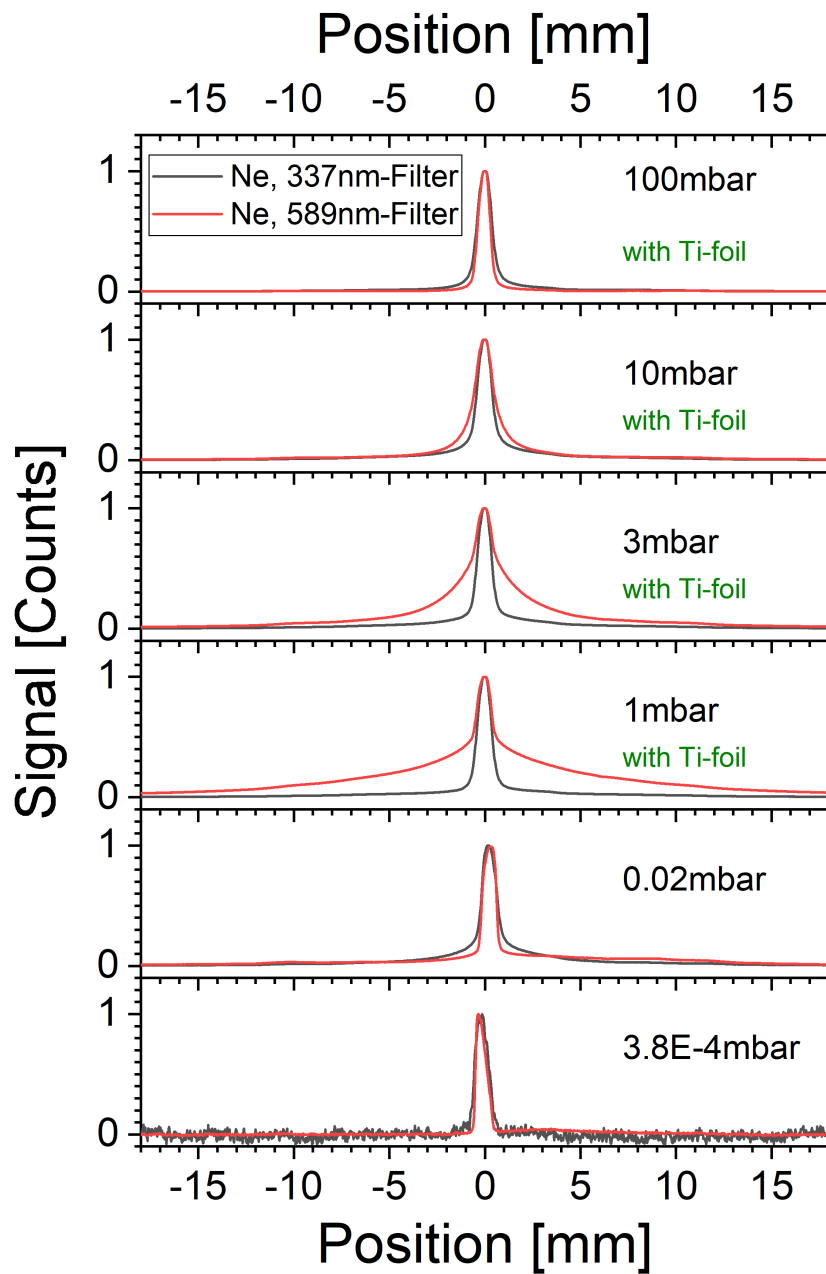


Figure 3.27: Comparison of the beam profiles in neon at various pressures induced by a sulfur beam of 87MeV before entering the target chamber through an aperture of 1mm diameter (through an additional Ti entry-foil for 1mbar and higher). The beam profile from the ionic light emission is shown in black, the one from the atomic light emission in red.

Scaled to the density of neon the following Himpsl-Radius for neon is obtained:

$$r_{Himpsl}(Ne, gas, 293K, 1mbar) = 7.56mm \cdot \left( \frac{E/MeV}{m/u} \right)^{0.52} \quad (3.3)$$

The energy of the sulfur beam was 87MeV before entering the target chamber. As stated above a titanium entrance foil was used to separate the chamber for pressures of 1mbar and higher. The remaining energy behind the foil was calculated to be 74MeV (see section 2.1).

It is obtained that in argon at 1mbar 66% of the energy of secondary electrons is deposited within a 7mm radius. Thus, a major part of the secondary electrons leaves the bulk of the beam and induces light emission in a halo around the original ion beam. This leads to an enhancement of the full width at half maximum (FWHM) of the beam profile, as can be seen below. Thus, the Himpsl-Radius has an impact on the FWHM of the beam profile. The halo can only be seen in the case of the atomic light emission, since secondary electrons almost exclusively excite atoms.

At 50mbar the calculated Himpsl-Radius is reduced to 0.13mm. At a beam radius of initially  $\sim 1$ mm and a spatial resolution of the camera system of 0.08mm at the position of the beam, this leads to no significant widening of the beam as it can be seen in the plots. At  $8 \cdot 10^{-4}$ mbar however, the Himpsl-Radius is 8.8m, which means that almost all electrons leave the beam by far and lead to no light emission in the observed volume. Similar observations are made with neon as target gas, while here the Himpsl-Radius is larger by a factor of 1.8. Therefore, the halo appears already at slightly higher pressures.

In Figure 3.28 and 3.29 the FWHM for both the ionic and the atomic light emission is plotted with respect to pressure. Both plots show a maximum of the FWHM in the mbar region. As expected the maximum of the FWHM for the atomic emission is shifted to higher pressures in neon, due to its lower density. The width of the original beam also depends on the focusing of the beam and its steering through the aperture into the target chamber. This results in FWHM of less than 1mm at lower pressures ( $< 10^{-2}$ mbar) and higher pressures ( $> 100$ mbar). Throughout the experiments the beam focus and steering was kept constant, making it possible to compare the FWHM under different circumstances.

Those observations can be put in relation to the observations from the comparison of the wavelength spectra with ion beam with respect to the electron beam excitation in section 3.1.2:

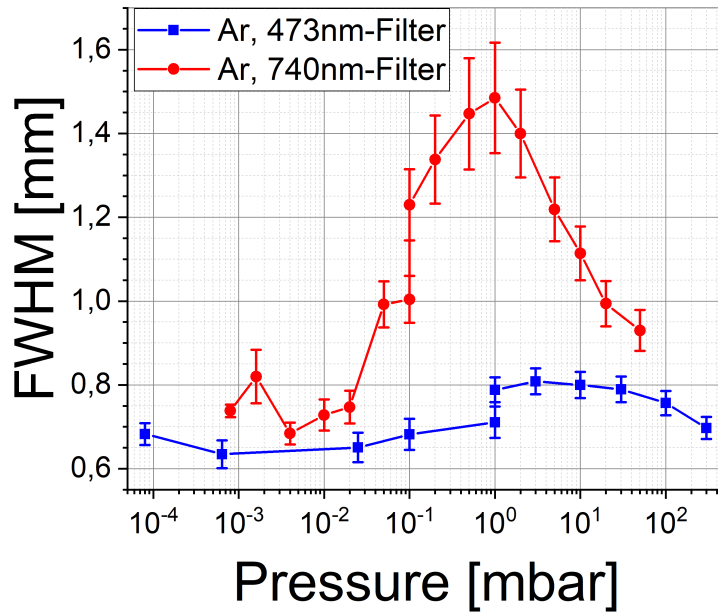


Figure 3.28: Full width at half maximum (FWHM) plotted versus pressure in argon. The halo induced by secondary electrons leads to a widening of the atomic light emission of the beam with a maximum at  $\sim 1$ mbar. Beam straggling leads to an additional widening of the beam the beam enters the target chamber through the Ti foil (here at pressures of  $p \geq 10^{-1}$ mbar for the atomic light emission and for  $p \geq 1$ mbar for the ionic light emission). The ionic light emission of the beam is on a roughly constant level.

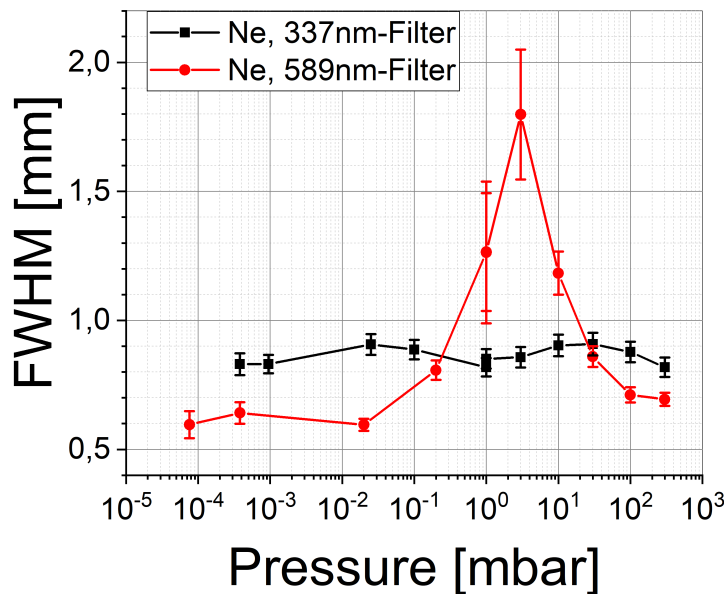


Figure 3.29: Full width at half maximum (FWHM) plotted versus the pressure in neon. Here the halo has its maximum at  $\sim 3$ mbar. The ionic light emission of the beam is on a roughly constant level between 0.8mm and 0.9mm.

At higher pressures in the region of  $\sim 100\text{mbar}$  the secondary electrons have a much shorter range and thus deposit almost all of their energy within the bulk of the beam. Therefore, the original beam is mapped accurately by the light emission. There is no significant difference between the observed beam profiles with bandpass filters in the ionic wavelength region and in the atomic wavelength region. Only the intensity in the ionic region is roughly 3 orders of magnitude less, since secondary electrons rarely excite ions as stated already above. The intensity is discussed in section 3.4 in further detail and is mentioned here just briefly.

In the  $\sim\text{mbar}$  region the secondary electrons deposit most of their energy within a cm-region. The volume in which the electrons deposit their energy is thus not very large yet leading to an excitation density by secondary electrons that is still large enough to lead to a halo around the original beam and the beam profiles differ distinctively. The ionic beam profile shows the heavy ion induced beam profile which lies completely in the line of the original beam, while the atomic beam profile has a strong contribution from secondary electron induced excitation. Going to even lower pressure ( $p < 10^{-2}\text{mbar}$ ) the secondary electrons have a Himpl-Radius in the meter range and thus mostly leave the original beam by far. Going from a pressure of 1mbar to  $10^{-2}\text{mbar}$  rises the Himpl-Radius by a factor of 100, the “illuminated” volume increases by a factor of  $10^6$ . The excitation density induced by the electrons is negligibly small, hence, their contribution to the light emission in the observed volume is negligible and the direct excitation by the heavy ions beam is almost exclusively responsible for the light emission. Therefore, in the case of those very low pressures, the light emission maps the original ion beam very accurately both in the ionic and in the atomic wavelength region.

### 3.4 Effective emission cross-sections in argon and neon

Different accelerator experiments can have very different parameters: the vacuum in the beam lines can vary by several orders of magnitude. Different particles from electrons over protons up to uranium can be accelerated. Furthermore there are experiments with particle energies in the keV range but also in the MeV, GeV or even TeV range and the beam currents can vary by far as well. To cover all those parameters is not possible in one accelerator experiment. Therefore, in this project it was mainly experimented with an ion beam of an intermediate projectile mass ( $^{32}\text{S}$ ) and an intermediate particle energy of 87MeV (resp. 100MeV). The electrical currents of the

beam were between 50nA and 300nA. One beam time was performed with a proton beam of 14MeV particle energy.

All camera systems used were absolutely calibrated with the help of a Wi17G calibration lamp, which made it possible to calculate the actual absolute light emission from the recorded light intensity. The knowledge of the absolute light emission per time interval in the observed volume, the beam current of the projectile particles, the pressure in the target gas, and the mean charge state allows to calculate effective emission cross-sections. In this work effective emission cross-sections were measured, i. e. emission cross-sections measured on base of the light emission detected by the detector system and the flux of the projectiles. Possible further effects like for example cascades, recombination and collisional de-excitation are not taken into account.

$$\frac{\text{Photon emission rate}}{\text{Volume}} = \sigma n j \quad (3.4)$$

Here  $\sigma$  is the effective emission cross-section,  $n$  the particle density of the target particles and  $j$  the flux of the projectiles. This equation can be solved for  $\sigma$ :

$$\sigma = \frac{\text{Photon emission rate}}{V \cdot n \cdot j} \quad (3.5)$$

### 3.4.1 Charge state of the ion projectiles

The sulfur ions of the ion beam are brought to a charge state of 8+. This is accomplished by the foil stripper of the tandem accelerator. Changes of the charge state in the high vacuum of  $10^{-8}$ mbar in the beam line can be neglected even over the long distance of roughly 60m from the accelerator to the target chamber. The ions enter the target chamber through a Ti foil with a thickness of  $1.1\text{mg}/\text{cm}^2$  for higher pressures ( $p \geq 1\text{mbar}$ , resp.  $p \geq 0.3\text{mbar}$ ). The initial energy of the ions is 2.7MeV/u from which an equilibrium mean charge of 13.5+ is obtained as can be seen in Figure 3.30. This charge state of the ion beam remains the same on the way through the target gas, since it is also the equilibrium state.

### 3.4.2 Region of interest and image processing

The region of interest (ROI) from which the data for the light emission (and also the beam profiles) is taken, is kept the same throughout all the images and different camera systems. In Figure 3.31 an example image is shown with the ROI drawn as yellow box. The ROI is located centrally in front of

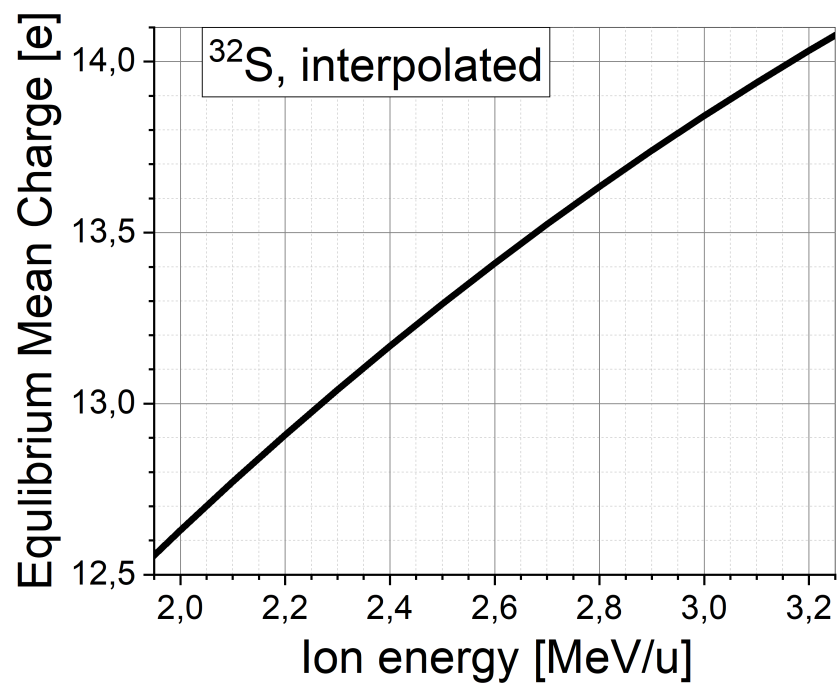


Figure 3.30: Equilibrium mean charge of the sulfur ion projectiles behind the Ti foil in dependence of the incident energy of the beam. In this experiment mostly a beam energy of 87MeV was used, which translates to 2.7MeV/u for sulfur ions. Hence, the equilibrium mean charge is 13.5. The diagram shows an interpolation of values tabulated in [43, p. 184] for ions with  $Z=16$ .

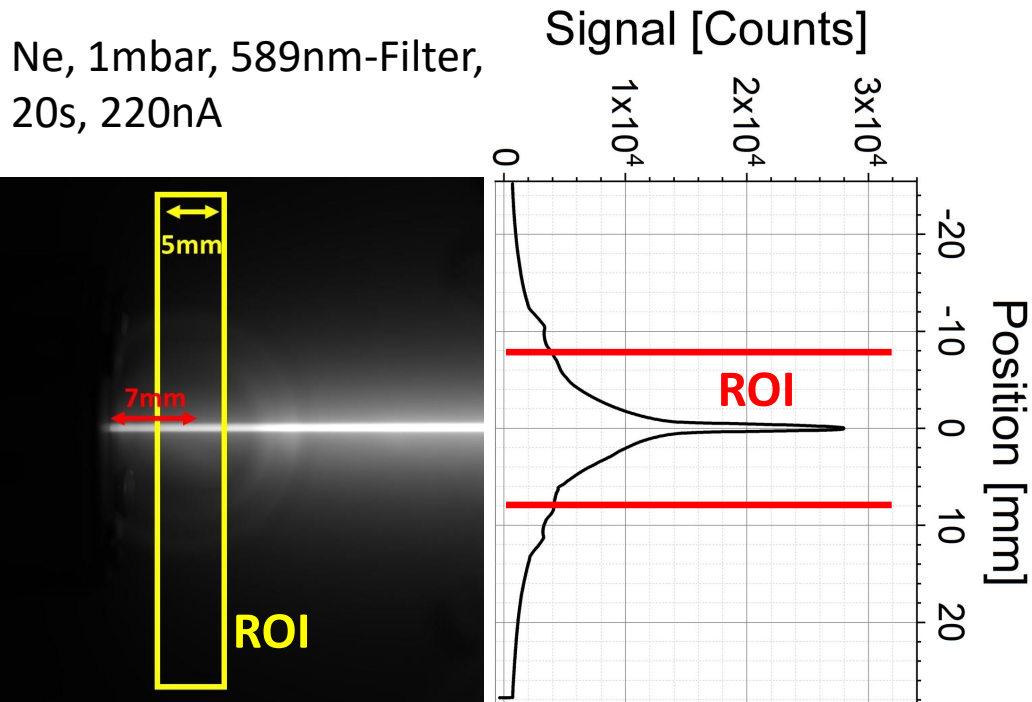


Figure 3.31: Example of an image of the ion beam in neon at 1mbar taken through a 589nm-Filter (left). The region of interest (ROI) is marked by the yellow rectangle. The profile is plotted perpendicular to the beam (right). The values of the signal are averaged over the 5mm width of the ROI and thus denote the mean value in one pixel. The region of interest for the integration of the Signal is marked by the red bars in the diagram on the right side.

the  $MgF_2$ -window that leads towards the spectrographic setup. Since said  $MgF_2$ -window is low reflective the background from reflections is assumed to be very small and thus negligible. On the right side of Figure 3.31 the profile plot of the image is shown. Reflections from the flange mounting the  $MgF_2$ -window are visible in the profile plot. The ROI for the data analysis of the profile plot is within the red bars. The values of the signal are averaged over the 5mm width of the ROI and thus denote the mean value in one pixel. In order to obtain the total light emission the integral over this ROI is taken. The background was subtracted beforehand.

### 3.4.3 Absolute light intensity measurement

The integral under the profile plot is the light emission that is detected by the camera system in a certain solid angle and within a certain exposure time. The integrals are calculated as described in the previous section and

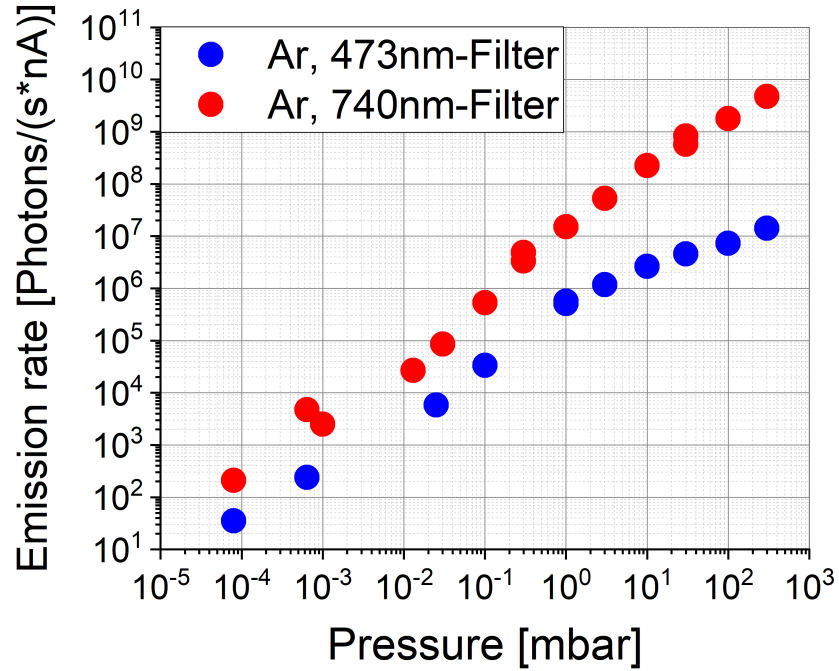


Figure 3.32: Photon emission per second and nA electrical current in dependence of pressure with argon as target gas. The photons are emitted from a volume described in Figure 3.31. Since the signal is averaged over the pixels in one horizontal line, the volume has an effective width of the width of the image of a pixel at the position of the beam (here 48.4 $\mu$ m).

divided by the exposure time and the electrical beam current. The beam current was measured in the evacuated target chamber. The modification of the charge state in the entrance foil was taken into account (see section 3.4.1). Furthermore, it is scaled to the full  $4\pi$ sr solid angle. With the help of a Wi 17/G calibration lamp the grey value (or counts) from the images can be translated into the number of emitted photons by the beam along a unit length of the beam in the target gas. The absolute calibration is described in section 2.6.4. The absolute values for the light emission per second and  $nA_{el}$  (unit nA electrical current, in comparison to  $nA_{part}$ : nA particle current) over the full sphere solid angle is obtained. Figure Figure 3.32 and Figure 3.33 show the photon emission rates for neon and argon, respectively over a very wide pressure range. Excitation was achieved with a 87MeV  $^{32}\text{S}$  ion beam. In red the values recorded through the 589nm-filter are plotted, which lets pass mainly the 585.2nm atomic emission line. In blue the emission recorded through the 337nm-filter is shown, especially the 337.8nm ionic emission line.

Below a pressure of  $10^{-2}$ mbar the emission rates are comparable. As already discussed in section 3.3 in this pressure region direct excitation by the ion

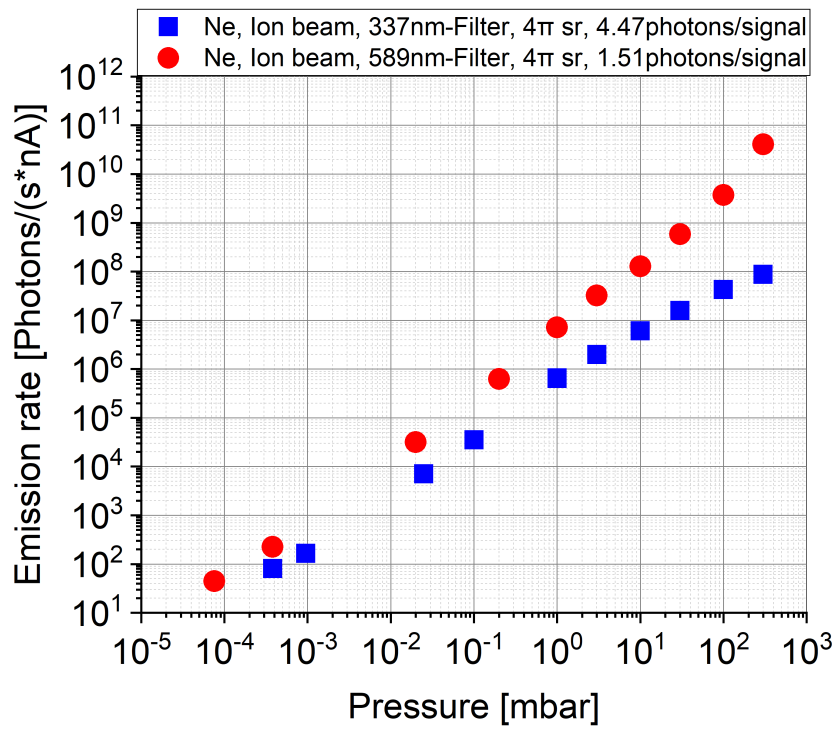


Figure 3.33: Photon emission per second and nA electrical current in dependence of pressure with neon as target gas. The photons are emitted from a volume described in Figure 3.31. The size of the emitting volume was calculated using the reproduction scale between the source and the camera taking the pixel size into account.

beam in the bulk of the beam takes place almost exclusively, while secondary electrons have long ranges and leave the bulk of the beam by far. Since the ion beam excites both ions and atoms the emission rates are similar for the ionic compared to the atomic emission. This depends obviously on the type of transition that leads to the light emission.

When the pressure is raised, the emission rates of the atomic lines increase stronger, since then the secondary electrons contribute to the light emission due to the shorter range. A further increase of the emission rates happens for 30mbar and upwards due to more efficient recombination. Meanwhile the emission from the ionic lines is suppressed due to quenching.

### 3.4.4 Calculated effective emission cross-section

In the beginning of this chapter, equation (3.5) for the calculation of the effective emission cross-section was already mentioned. This equation has to be slightly modified in order to apply it to the measuring parameters of the experiments.

$$\sigma = \frac{\text{number of emitted photons}}{I \cdot t} \cdot \frac{q \cdot A}{N_T} \quad (3.6)$$

$A = \pi \cdot (0.5\text{mm})^2 = 0.785\text{mm}^2$  is the cross-sectional area of the beam.  $N_T$  is the number of target particles in the volume  $V = A \cdot l_{\text{Pixel}}$ , with the pixel width  $l_{\text{Pixel}}$ , the width of the image of a pixel at the position of the beam. The values for the pixel width are listed in Table 2.2 for each camera system. The charge of the ions is  $q$ , the electrical beam current is  $I$  and the exposure time is  $t$ .

The results for the effective emission cross-sections at different pressures are shown in Figure 3.34 and 3.35. A wide pressure range was covered over 8 orders of magnitude from  $10^{-5}$ mbar up to  $10^3$ mbar. As stated before, the necessity of using a Ti entry-foil for higher pressures leads to an enhanced charge state of the ions of the beam as well as to an energy loss in the foil. The displayed diagrams show the data without any scaling due to a higher charge state or lower energy. The green arrow shows for which pressures the Ti foil was used. At the pressure at which the foil was inserted two measurements were conducted: one without foil and one with it. It can be seen that a higher charge state of the ion projectiles result in higher interaction cross-section.

Three different regions can be observed: the low pressure region below  $10^{-2}$ mbar, the intermediate pressure region between  $10^{-2}$ mbar and 10mbar and the higher pressure region around  $\sim 100$ mbar.

#### Low pressure region ( $p < 10^{-2}$ mbar)

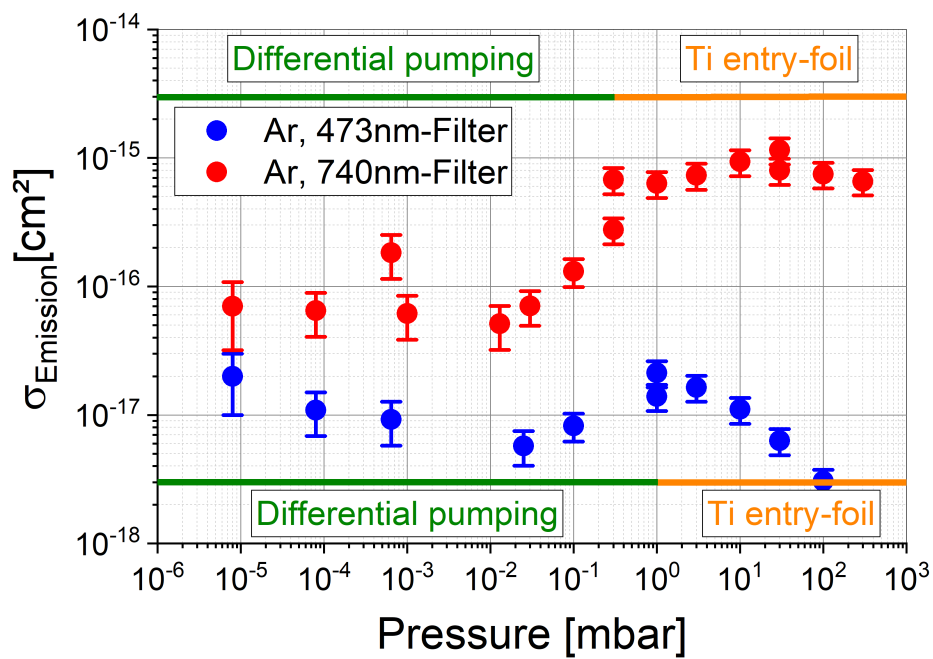


Figure 3.34: Measured effective emission cross-section of with a  $^{32}\text{S}$  ion beam with an initial particle energy of 87MeV in argon as target gas. The measurement were performed in two different beamtimes. Therefore differential pumping was done in one case from 0.3mbar downwards (atomic lines, red) and from 1mbar downwards in the other case (ionic line, blue).

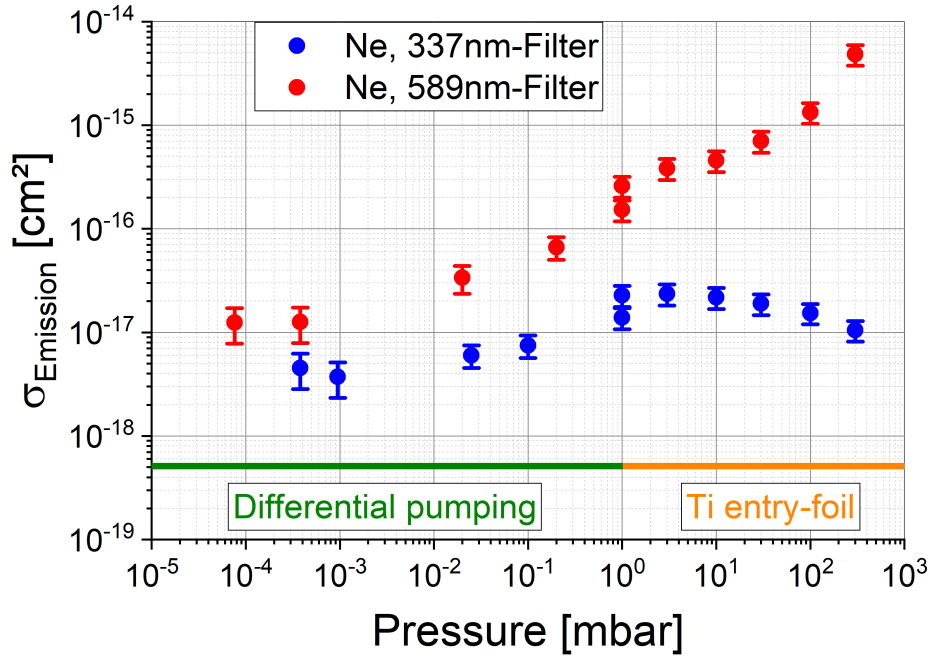


Figure 3.35: Measured effective emission cross-section of a  $^{32}\text{S}$  ion beam with an initial particle energy of 87MeV in neon as target gas.

This region is of special interest for determining the effective emission cross-sections. At this pressure recombination is not efficient and leads to only a negligible light emission as well as emission via secondary electrons. Thus, only direct collisions of ion projectiles with the target atoms occur and the effective emission cross-section is expected to be the emission cross-section of the light emission induced by direct collisions and from cascades in the atoms and ions. Table 3.3 shows the mean values of the measured emission cross-sections in this pressure region for both target gases argon and neon. Both the ionic and the atomic light emission show a similar behavior. However, the emission cross-sections in the atomic case is larger by a factor of 7 (argon) and a factor of 3 (neon) respectively. Due to the higher cross-sections argon is the better choice for an optical beam profile monitor at very low pressures in a beamline system.

#### Intermediate pressure region ( $10^{-2}\text{mbar} < p < 100\text{mbar}$ )

In this pressure region the Himpls-Radius reaches the cm to mm region. Light emission induced by secondary electrons are becoming a more and more significant fraction of the total light emission, hence, the effective emission cross-section increases in the case of the atomic light emission. A small rise is also observed in the case of the ionic light emission. This is due to

Gas	Filter [nm]	Main emission line [nm]	Transition	$\sigma_{Emission}$ [cm <sup>2</sup> ]
Ar	473	476.49	$4p \rightarrow 4s$	$(1.3 \pm 0.6) \cdot 10^{-17}$
Ar	740	738.40	$4p \rightarrow 4s$	$(9.5 \pm 5.9) \cdot 10^{-17}$
Ne	337	337.82	$3p \rightarrow 3s$	$(4.1 \pm 1.6) \cdot 10^{-18}$
Ne	589	585.25	$3p \rightarrow 3s$	$(1.3 \pm 0.5) \cdot 10^{-17}$

Table 3.3: In all cases a  $^{32}S$  ion beam with an energy of 2.7 MeV/u was used. The charge of the ions was 8+ and no entry-foil was used. All values are determined from target gas pressures below  $p < 10^{-2}$ mbar.

an increased mean charge state in the gas around 1mbar. However, the secondary electrons do rarely excite the ions of the target gas and thus, lead to no significant further increase of the emission cross-section. Furthermore, the mean charge is 13.5 for the higher data point at 1mbar and the data of the higher pressure due to the insertion of the entrance foil. This leads to a higher dE/dx and thus to an increased interaction cross-section. On the other hand the energy is decreased in the foil to 2.3MeV/u this leads to a slight enhancement of the dE/dx by about 5% (see Appendix A).

### Higher pressure region ( $p \geq 100$ mbar)

The mean charge is 13.5 and thus the dE/dx is higher for all values in this pressure region. Additionally, recombination becomes more efficient and results in a significant rise of the emission cross-section in the atomic case but not in the ionic case. Since singly ionized atoms are much more abundant than further ionized ones recombination leads mostly to light emission from atomic transitions.

### Longpass filter

Additional to the bandpass filters a longpass filter was purchased. The cut-on wavelength was 540nm, i.e. it has a high transmission above 540nm and a low transmission for wavelengths shorter than 540nm [44]. With this filter the whole bunch of atomic emission lines of argon was imaged. Taking images without a filter and then subtracting the images with the 540nm filter gives an image of the whole bunch of ionic emission lines, i.e. the image that could be recorded using a shortpass filter with a cut-off wavelength of 540nm. Effective emission cross-sections for the total ionic and atomic fraction, respectively, were calculated. This was done for the two lowest possible pressures. The results are added to the diagram in Figure 3.34 and is shown in Figure 3.36.

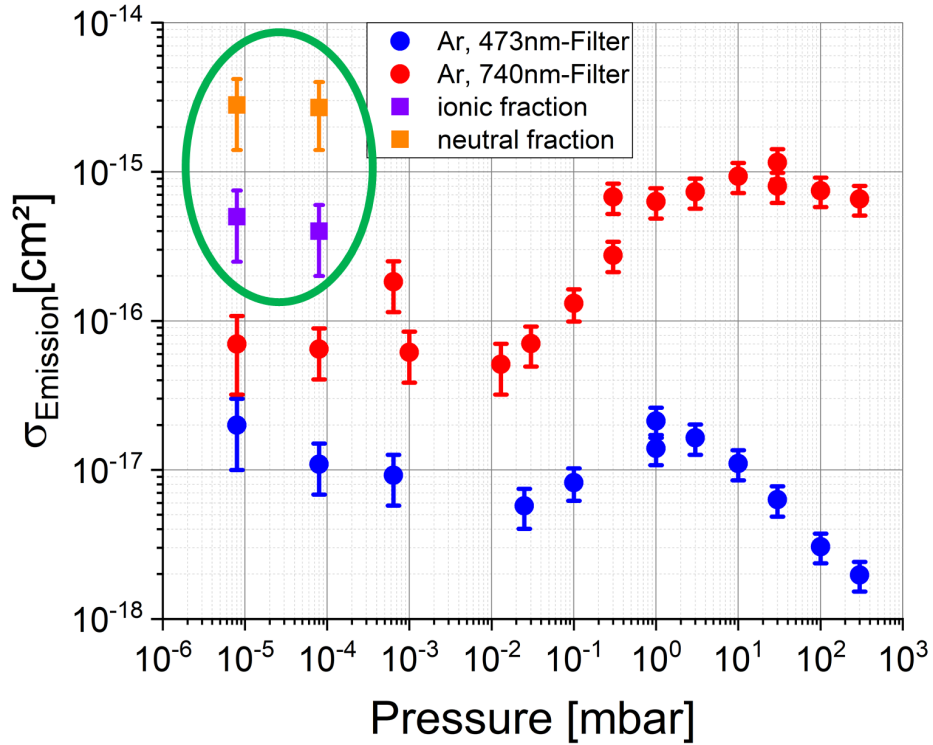


Figure 3.36: Same diagram as in Figure 3.34. But here the effective emission cross-sections of the ionic (purple) and atomic (orange) fraction of emission lines are added to the plot. The ionic fraction is calculated from the light emission from all emission lines below 540nm. The atomic fraction is calculated from the light emission from all emission lines above 540nm. To measure this a longpass filter was used with a cut-on wavelength of 540nm.

This measurement shows the possibilities when using a shortpass filter: not only selected ionic emission lines would could be recorded but whole spectrum below 540nm. This would result in a detected emission rate one order of magnitude higher than with bandpass filters, while still cutting out the atomic emission lines.

### 3.4.5 Effective emission cross-sections in nitrogen

For the application in accelerator experiments nitrogen is not desired as a target gas for the gas jet at CERN [45]. Furthermore, nitrogen is very efficiently pumped by ion pumps and therefore leads to a coating of the cathode material saturating the pump very quickly. This might be a problem for many accelerators that use mainly ion pumps to maintain the vacuum in the beamline. However, measurements were still performed with nitrogen for

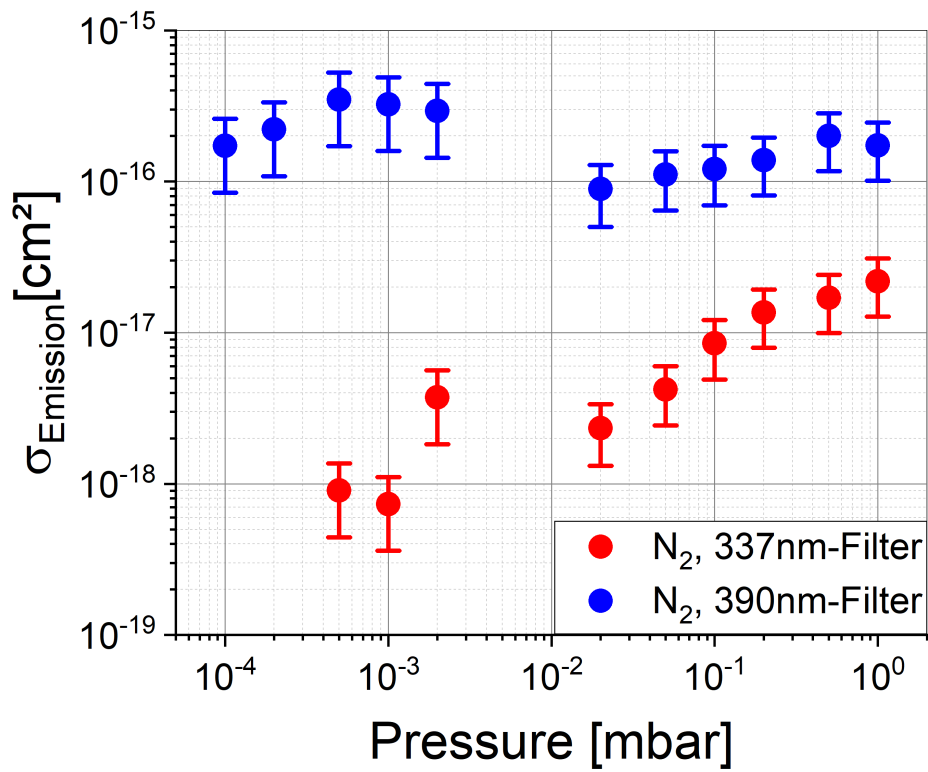


Figure 3.37: Effective emission cross-section for sulfur ion beam (particle energy: 87MeV) excited nitrogen gas. In blue cross-sections of the ionic emission from  $\text{N}_2^+$  (391nm) is shown for various pressures, in red cross-sections of the neutral molecular emission (337nm).

comparison. The results shall be shown here in the following.

The beam was imaged using the bandpass filters with center wavelength (CWL) of 337nm and 390nm, respectively. With those filters the light emission from the 337nm and the 391nm emission bands in nitrogen was imaged. These emission bands were already shown in Figure 3.7 in section 3.1.1. The 337nm-band has its origin in the excitation of  $N_2$  molecules, while the 391nm-line is an ionic emission band from  $N_2^+$ .

The effective emission cross-section for the 391nm ionic emission is roughly constant within the error bars throughout the complete pressure range from  $10^{-4}$ mbar up to  $10^0$ mbar. The mean value is  $(2.0 \pm 0.9) \cdot 10^{-16} \text{cm}^2$ .

For the atomic emission at 337nm a similar behavior as above with the atomic emission from argon and neon is observed: towards a pressure of  $10^{-1}$ mbar the effective emission cross-section rises, due to the already discussed reduction of the range of secondary electrons. For pressures below  $10^{-3}$ mbar the effective emission cross-section appears to remain constant, which the two lowest values show as well. The mean of those two values is  $(8.2 \pm 4.5) \cdot 10^{-19} \text{cm}^2$ .

### 3.5 Effective emission cross-sections with a proton beam

Proton beams are used in many accelerator experiments for example in the LHC at CERN, in the Tevatron at Fermilab or in HERA at DESY. The FAIR accelerator facility at GSI plans for proton beams in the future as well. Of great interest are proton-antiproton collisions for the research of physics beyond the Standard Model. Furthermore proton beam therapy is a medical application of growing interest.

The Munich Tandem accelerator can provide a proton beam of up to 30MeV particle energy. One of the beamtimes in this project was dedicated to experiments with proton beams. Due to beam stability reasons the particle energy was set to 14MeV. Radiation protection issues restricted the beam currents to  $\sim 5$ nA in the target chamber.

The images were processed the same way as described above in the case of a sulfur beam. Target gas was neon. The images were recorded using the ProEM+ 512B camera. This was the only beamtime that camera was used. The results for the effective emission cross-sections can be seen in Figure 3.38. The ionic emission could not be observed for pressures below  $10^{-2}$ mbar with a reasonable exposure time of a few hours. The stronger atomic emission was observed down to  $10^{-3}$ mbar. The mean value for the effective emission

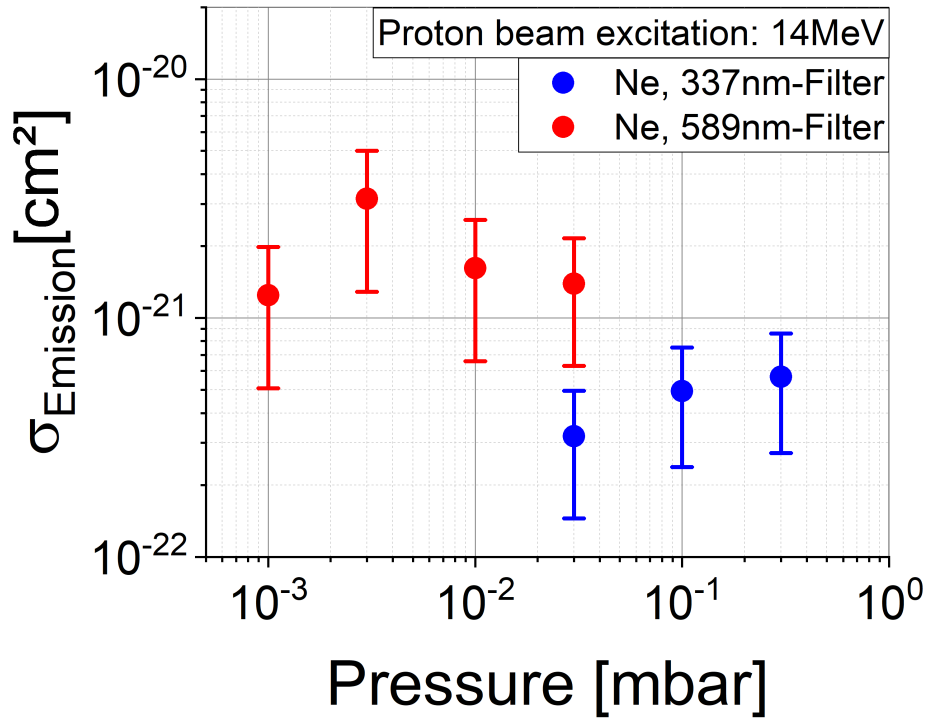


Figure 3.38: Results for the effective emission cross-sections of a proton beam in a neon gas target. Two different bandpass filters were used: through the 337nm-filter mainly the 337.82nm ionic emission line and through the 589nm-filter mainly the 585.25nm atomic emission is imaged. In blue the results for the ionic emission is shown, in red the results for the atomic emission.

cross-section of the ionic line (337nm-filter) is  $(4.6 \pm 2.9) \cdot 10^{-22} \text{cm}^2$ . The effective emission cross-section of the atomic line (589nm-filter) was measured with a mean value of  $(1.9 \pm 0.9) \cdot 10^{-21} \text{cm}^2$ .



# Chapter 4

## Conclusion

The spectral results show the difference in pressure dependence between ionic emission lines and atomic emission lines. While atomic emission lines totally dominate the light emission at higher pressure ( $\sim 100$ mbar) and the contribution of the ionic emission lines is nearly negligible, this changes towards lower pressures. For applications in accelerator beamline experiments much lower pressures are of interest: Most beamlines have a high vacuum between  $10^{-7}$  and  $10^{-9}$ mbar or even lower. A gas jet as target gas for monitoring the beam profile would not have a higher pressure than  $10^{-6}$ mbar in order to prevent the vacuum in the beamline from deteriorating or saturating ion pumps. In the target chamber used in the experiments described here it was not possible to reach a pressure of  $10^{-6}$ mbar or below. However, the tendency towards such low pressures is clear.

In the pressure region of  $10^{-2}$ mbar and lower both ionic and atomic lines are comparably strong. Thus, both types of lines appear to be a good option.

Besides excitation of atoms, and ionization and excitation in single collisions by heavy ion projectiles there is also excitation by secondary electrons. In experiments using an electron gun to simulate excitation by secondary electrons the difference compared to heavy ion excitation was studied. As expected secondary electrons very rarely ionize and excite target atoms in single collisions, thus, leading to much weaker ionic lines in the wavelength spectra of the light emission.

This knowledge together with the beam profiles recorded by a camera and the calculated radius within which the secondary electrons deposit 66% of the energy leads to a better picture about the mechanisms involved. For pressures around  $\sim 100$ mbar the radius within which the electrons deposit 66% of their energy is well below the beam diameter of 1mm, for pressures below  $10^{-2}$ mbar this radius is in the meter range. Therefore, in the higher pressure range most secondary electrons remain within the original ion beam and for

lower pressures most secondary electrons leave the beam by far. For both higher and lower pressures the profiles of the light emission match the profile of the original ion beam. This is not the case for intermediate pressures around 1mbar: here a halo from the light emission induced by secondary electrons is visible and widens the apparent profile of the beam. Since secondary electrons almost exclusively excite atoms the ionic light emission is not influenced by this effect and shows the original beam profile for all pressures.

After absolutely calibrating the camera systems the effective emission cross-section were determined from the images recorded of the light emission from the heavy ion beam. For pressures below  $10^{-2}$ mbar the effective emission cross-sections stay roughly constant in all target gases studied (Ar, Ne,  $N_2$ ). At those pressures the contribution of secondary electrons and recombination to the light emission is negligible as stated above. Only collisions of heavy ion projectiles with target atoms contribute significantly to the light emission. Thus, the effective emission cross-section are expected to remain on a constant level for lower pressures and can therefore be used to calculate emission rates in various experiments with the mentioned target gases.

The highest effective emission cross-section was measured for the ionic emission from nitrogen at 391nm. However for monitoring an ion beam in a beamline nitrogen is not the desired target gas for the technical reasons mentioned before.

For both argon and neon the cross-sections of the atomic emission lines are higher than for the respective ionic emission lines. The effective emission-cross-section of the 738.40nm line of argon is roughly 5 times higher than of the strongest neon line at 585.25nm. It has to be mentioned that the 738.40nm line of argon is not even the strongest line in argon: at low pressures the 750.39nm line with its neighboring line at 751.47nm (both atomic lines) appear to be a better choice.

Another important topic to be discussed with respect to applications in accelerator experiments for beam profile monitors are exposure times. In order to have an efficient beam profile monitor the exposure times should not exceed 1s. That way steering of the beam would be possible essentially in real time.

The most promising camera with respect to exposure times of the three cameras tested is the PI-Max4 1024f. In Figure 4.1 and Figure 4.2 two images recorded with said camera and the 473nm bandpass filter are shown. The first image has an exposure time of 20s. With the right adjustment and image processing, the beam is fairly visible and its position can be determined. The second image was taken with an accumulated exposure time of 1000s.

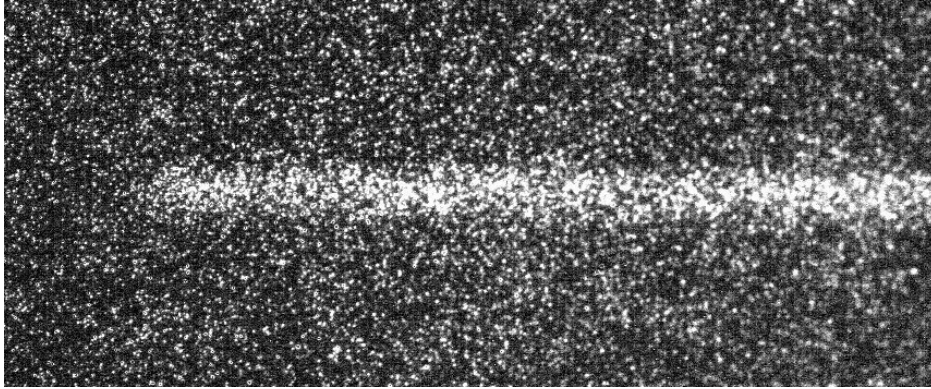


Figure 4.1: Image of the heavy ion beam in the target chamber with argon at a pressure of  $10^{-4}$  mbar and with an exposure time of 20s. The 473nm-bandpass filter was used. The beam is visible in the center of the image with proper adjustments of brightness and contrast. The position of the beam can be well determined.

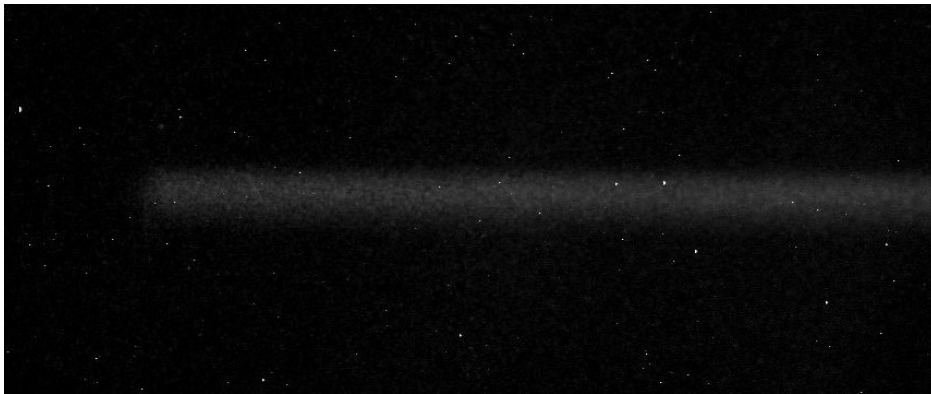


Figure 4.2: Image of the heavy ion beam ( $^{32}\text{S}$ , particle energy: 90MeV) in the target chamber with argon at a pressure of  $10^{-4}$  mbar and with an exposure time of 1000s. The 473nm-bandpass filter was used. The beam is clearly visible in the center of the image. The position of the beam can be well determined. Furthermore, even the slight asymmetric shape of the beam is visible.

The beam is very well visible and not only the position of the beam can be determined but also the shape of the beam. The images were recorded at a pressure of  $10^{-4}$ mbar in the target gas (argon) and with a particle current of the beam of roughly 200nA. In a possible application the pressure of the gas jet through the beamline would be somewhere in the range of  $10^{-7}$ mbar. This is three orders of magnitude lower than in this experiment. However, with a much higher particle current exposure times in the range of 1s and below would be possible.

In order to improve the signal and to shorten the exposure times a filter that lets a wide range of wavelength pass is a good possibility. The measurements performed with such a filter with argon as target gas showed a signal improved by more than one order of magnitude.

Finally the exposure time needed to require good enough images for the desired purpose naturally depends on the ion projectile used in the experiments. Different projectiles have different effective emission cross-sections. From the cross-sections measured in this experiment with the given parameter scaling to other projectiles will be possible if appropriate atomic physics processes are implemented.

# Appendix A

## Energy loss in the Ti-foil and the target gas

A titanium entrance foil was used to separate the target chamber from the beamline. This was necessary for pressures above 1mbar, since then the differential pumping setup was not able to effectively keep the pressure in the beamline below  $10^{-7}$ mbar. The heavy ion beam can enter the target chamber through a Ti foil of  $1.1\text{mg}/\text{cm}^2$  thickness but the beam current had to be kept well below 100nA in order to prevent the foil from destruction by the beam. However, there is an energy loss in the foil due to collisions of the ion projectile with the atoms in the foil. The energy loss was calculated using ATIMA, a program that calculates various physical quantities of collision processes with proton or heavy ion projectiles [16]. The calculations are based on precalculated tables from the FORTRAN code.

In the first experiments the particle energy of the sulfur beam was set to 100MeV or 3.12MeV/u. The calculated exit energy of the beam after passing through the foil is 2.72MeV/u or 87.2MeV. In later experiments without the Ti foil the particle energy of the sulfur beam was set to 87MeV from the start and was not changed after reinserting the Ti foil. Keeping the particle energy of the beam at 87MeV with and without the entrance foil has two great advantages: since the particle energy of the incident beam was kept at the same energy there was no need for new steering and focusing of the beam that takes a long time and usually changes the shape of the beam. Furthermore, particle energy of 87MeV requires a lower acceleration voltage that is easier for the accelerator to maintain resulting in a more stable beam throughout the experiment. Downside is that the particle energy of the beam inside the target chamber changes if there is an entrance foil. After passing through the Ti entrance foil the sulfur beam with originally 87MeV (2.71MeV/u) has a particle energy of 73.4MeV (2.29MeV/u).

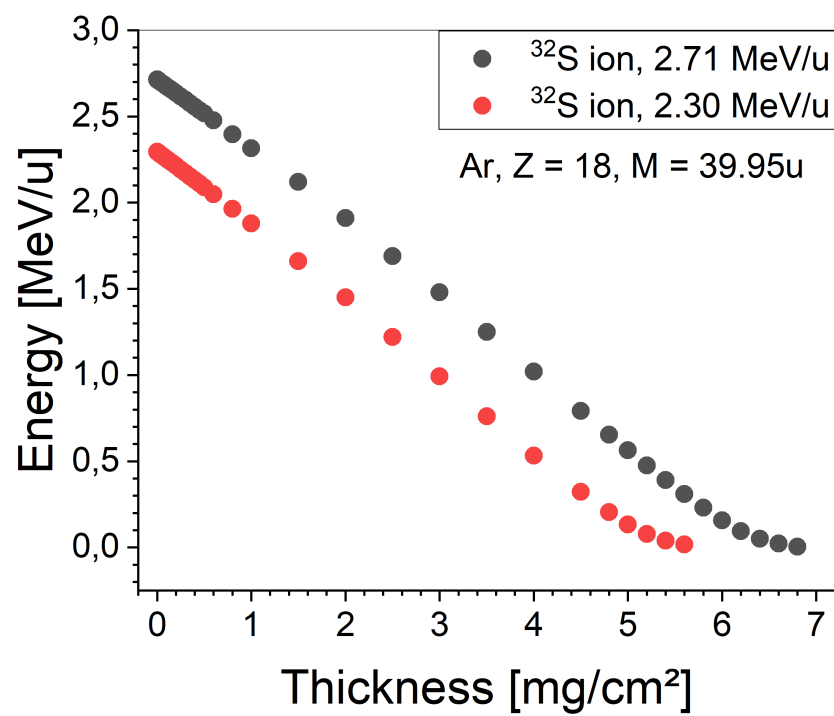


Figure A.1: Particle energy of a  $^{32}\text{S}$  ion on its way through gaseous argon. The initial energies are shown: 2.71MeV/u (black) and 2.30MeV/u (red). The data was calculated using ATIMA [16].

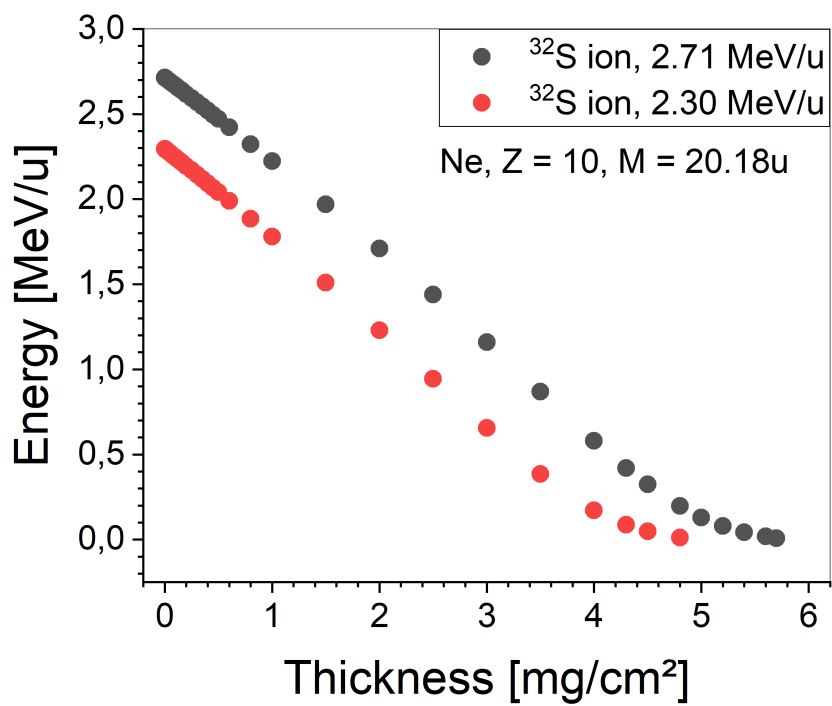


Figure A.2: Particle energy of a  $^{32}\text{S}$  ion on its way through gaseous neon. The initial energies are shown: 2.71MeV/u (black) and 2.30MeV/u (red). The data was calculated using ATIMA [16].

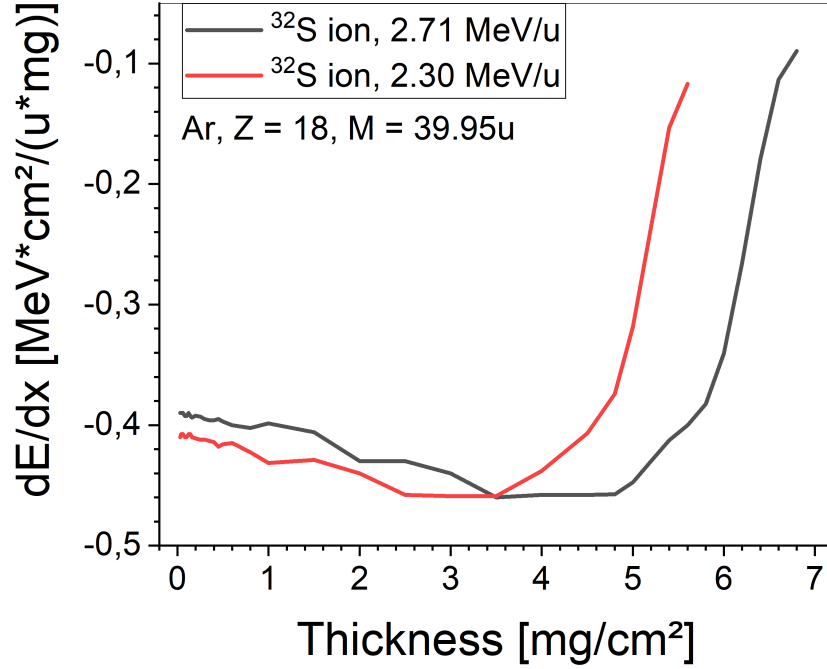


Figure A.3: Energy loss per unit length in gaseous argon for  $^{32}\text{S}$  ions with the initial energy of 2.71MeV/u (black) and 2.3MeV/u (red), respectively. Data shows the derivative of energy curves in Figure A.1.

Figure A.1 and Figure A.2 show the particle energy of the projectiles in dependence of the thickness of the gas in argon and neon, respectively. This thickness can be converted into distance from the entrance of the target chamber depending on the pressure. In argon a thickness of  $1\text{mg}/\text{cm}^2$  corresponds to a distance of 2.0cm at 300mbar and to a distance of 6.1km at a pressure of  $10^{-3}\text{mbar}$ . In neon the corresponding distances are even larger (300mbar:  $1\text{mg}/\text{cm}^2 \rightarrow 3.7\text{cm}$ ;  $10^{-3}\text{mbar}$ :  $1\text{mg}/\text{cm}^2 \rightarrow 11\text{km}$ ). As it is described in section 3.4.2 the ROI in the images is well within a distance of 2cm from the entrance foil/aperture. Thus, even at the highest pressure applied (300mbar) the thickness of the target gas does not exceed  $1\text{mg}/\text{cm}^2$ . Figure A.3 and Figure A.4 show the energy loss per unit length ( $dE/dx$ ) in argon and neon, respectively. This is the derivative of the energy curve shown in Figure A.1 and Figure A.2. It can be seen in both gases, argon and neon, that for a thickness below  $3\text{mg}/\text{cm}^2$  the difference in  $dE/dx$  for 2.7MeV/u incident energy compared to 2.3MeV/u is maximum 5%. This difference is much smaller than the uncertainty of the measurements performed during the experiments. This shows that inserting the Ti entrance foil without changing the energy does not change the energy deposition in the gas too much and is still accurate enough.

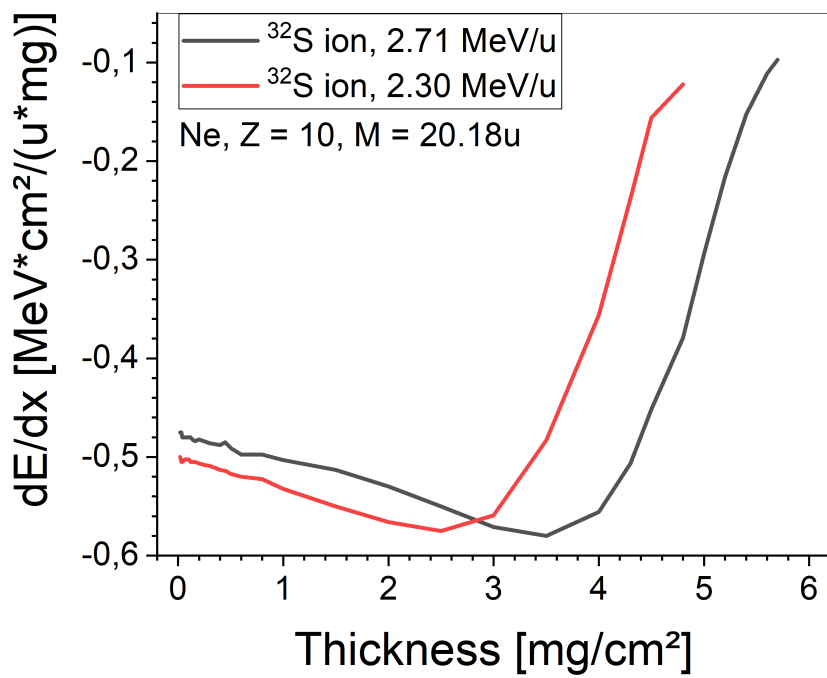


Figure A.4: Energy loss per unit length in gaseous neon for  $^{32}\text{S}$  ions with the initial energy of 2.71MeV/u (black) and 2.3MeV/u (red), respectively. Data shows the derivative of energy curves in Figure A.2.



# Bibliography

- [1] S. Varentsov et al., *Contrib. Plasma Phys.*, **48**, 586 (2008)
- [2] P. Forck, *Minimal Invasive Beam Profile Monitors For High Intense Hadron Beams*, Conf. Proc. IPAC 2010, Kyoto, p. 1261
- [3] F. Becker et al., *Beam Induced Fluorescence - Profile Monitoring For Targets And Transport*, Conf. Proc. of HB 2012, Beijing, p. 798
- [4] C. Andre et al., *Optimization Of Beam Induced Fluorescence Monitors For Profile Measurements Of High Current Heavy Ion Beams At GSI*, Conf. Proc. IBIC 2014, Monterey, p. 412
- [5] S. Udrea et al., *Development Of A Fluorescence Based Gas Sheet Profile Monitor For Use With Electron Lenses: Optical System Design And Preparatory Experiments*, Conf. Proc. IBIC 2017, p. 359
- [6] A. Salehilashkajani et al., *Commissioning Of The Prototype For A New Gas Curtain Beam Profile Monitor Using Beam Induced Fluorescence For HL-LHC*, Conf. Proc. IPAC 2019,
- [7] H. D. Zhang et al., *Development Of Supersonic Gas-Sheet-Based Beam Profile Monitors*, Conf. Proc. IPAC 2019
- [8] A. Ulrich, Schlussbericht BMBF-Projekt 05P15WOFA1, *Grundlegende Studien zur optischen Strahlprofilmessung*, Technische Universität München, 2019
- [9] G. Apollinari, I. Béjar Alonso, O. Brüning, P. Fessia, M. Lamont, L. Rossi and L. Taviani, CERN Yellow Rep. Monogr. **4** (2017) 1. doi:10.23731/CYRM-2017-004
- [10] S. Udrea, P. Forck *Milestone 1.1 Report, CERN e-Lens Project*, GSI Helmholtzzentrum für Schwerionenforschung, 11-25-2016

- [11] F. Becker, *Non-destructive Profile Measurement of intense Ion Beams*, Ph.D. thesis, Phys. Dept., Technische Universität Darmstadt, Germany, 2009
- [12] A. Ulrich, *Lichtemission und Lasereffekt bei Anregung mit ionisierender Strahlung*, Habilitationsschrift, Technische Universität München, 1998
- [13] A. Ulrich, Technische Universität München, *Private Communication*
- [14] G. Dollinger and T. Faestermann, *Physics at the Munich Tandem Accelerator Laboratory* Nucl. Phys. News **28** (2018) no.1, 5 doi:10.1080/10619127.2018.1427405 [arXiv:1802.07057 [nucl-ex]].
- [15] T. Faestermann, Technische Universität München, *Private Communication*, 04.04.2019
- [16] ATIMA GSI, *ATIMA, calculate ATomic Interaction with MATter*, version 1.4, downloaded from URL [<https://web-docs.gsi.de/~weick/atima/atima14.html>]
- [17] SAES getters, *PS4-MT3/15-R/N SPECIFICATIONS*, URL [[http://www.saespuregas.com/Library/documents/s110-243\\_rev\\_\\_528.pdf](http://www.saespuregas.com/Library/documents/s110-243_rev__528.pdf)], 05-22-2002
- [18] A. Morozov et al., *Ultraviolet emission from argon water-vapor mixtures excited with low-energy electron beams* Appl. Phys. Lett **86**, 011502 (2005)
- [19] M. Salvermoser, Dissertation *Untersuchung von Rekombinationslaserschemata bei Anregung mit hochenergetischen Schwerionenstrahlen*, Dissertation Fakultät für Physik (E12), TU München, 02-03-1998, p. 33
- [20] McPHERSON INSTRUMENT, Acton, Massachusetts, USA, *Instruction Manual, Model 218 0.3-Meter Scanning Monochromator*, 1975
- [21] McPHERSON INSTRUMENT, Acton, Massachusetts, USA, *Instruction Manual, Model 788 Scan Controller*, 1975
- [22] R. Hampf, A. Ulrich, J. Wieser, *Sensitivity calibration of 2-dimensional CCD detectors for beam profile monitors for high intensity particle beams*, submitted to EPJ Techniques and Instrumentation
- [23] JENOPTIK Optical Systems, LLC., Jupiter, Florida, USA, *UV-VIS-IR 60mm APO Macro*

- [24] ET Enterprises Ltd, 2007, DS\_9130/350B Issue 2 (05/04/07), *30mm (1 1/8") photomultiplier 9130/350B series data sheet*
- [25] Electron Tubes Limited, 2007, DS\_QL30-04 Issue 1, 5 march 2007, *photomultiplier housing with integral constant fraction discriminator and HV supply QL30-04*
- [26] ATIK cameras, Norwich, United Kingdom, *Atik 383L+ User Manual*, 2015
- [27] ON Semiconductor, Aurora, Colorado, USA, *KAF-8300, 3326 (H) x 2504 (V) Full Frame CCD Image Sensor*, October 2017 - Rev. 3
- [28] Princeton Instruments, Trenton, NJ, USA, *ProEM+ System Manual*, Version 1.A, October 24, 2012
- [29] Princeton Instruments, Trenton, NJ, USA, *PI-Max4 Camera System*, Issue 9, July 3, 2018
- [30] Edmund Optics, *Hard Coated OD 4 10nm Bandpass Filters*, URL [<https://www.edmundoptics.de/f/hard-coated-od-4-10nm-bandpass-filters/13837/>], 08-05-2019
- [31] Edmund Optics, *Traditional Coated 193 - 399nm Bandpass Interference Filters*, URL [<https://www.edmundoptics.de/f/traditional-coated-193399nm-bandpass-interference-filters/12232/>], 08-05-2019
- [32] Edmund Optics, *Traditional Coated 700 - 1650nm Bandpass Interference Filters*, URL [<https://www.edmundoptics.de/f/traditional-coated-700-1650nm-bandpass-interference-filters/13917/>], 08-05-2019
- [33] A.R. Striganov, N.S. Sventitskii, *Tables Of Spectral Lines Of Neutral And Ionized Atoms*, Translated from Russian, IFI/Plenum Data Corporation, New York, 1968
- [34] NIST Atomic Spectra Database Lines Form, [[https://physics.nist.gov/PhysRefData/ASD/lines\\_form.html](https://physics.nist.gov/PhysRefData/ASD/lines_form.html)], 06-03-2019
- [35] G. Ribitzki et al., Phys. Rev. E **50** (1994) 3973
- [36] J. Wieser et al., Rev. Sci. Instrum. **68** (1997) 1360
- [37] T. Dandl et al., Eur. Phys. J. **D68** (2014) 256 and references therein

- [38] A. Neumeier et al., EPL, **109** (2015) 12001 and references therein
- [39] J. Wieser, excitech GmbH, 26419 Schortens, *Private Communication*
- [40] A. Himpsl, *Particle & Energy Dependence of the Near-Infrared to Vacuum-Ultraviolet Scintillation Ratio of a Liquid Argon-Xenon Mixture*, Technische Universität München, 2018
- [41] C. Killer, *Abel Inversion Algorithm*, version 1.5.0.0 (March 7, 2016), downloaded from URL [<https://de.mathworks.com/matlabcentral/fileexchange/43639-abel-inversion-algorithm>]
- [42] M. Toulemonde, et al, *Temperature and pressure spikes in ion-beam cancer therapy*, Physical Review E **80**, 031913 (2009)
- [43] K. Shima, N. Kuno, M. Yamanouchi and H. Tawara, Atom. Data Nucl. Data Tabl. **51** (1992) 173. doi:10.1016/0092-640X(92)90001-X
- [44] Edmund Optics, *O-54 (540nm), 50mm Dia. Longpass Filter*, URL [<https://www.edmundoptics.de/p/o-54-540nm-50mm-dia-longpass-filter/20619/>], 08-22-2019
- [45] S. Udrea, P. Forck, *Milestone 1.6 Report, CERN e-Lens Project*, GSI Helmholtzzentrum für Schwerionenforschung, 09-03-2018
- [46] FAST ComTec GmbH Grünwalder Weg 28a, D-82041 Unterhaching, Germany, *MCS6A-2*, User manual, Version 1.05, July 15, 2013

## Danksagung

Allen voran möchte ich meinem Doktorvater Prof. Dr. Andreas Ulrich danken. Er hat mich zu jeder Zeit während der Arbeit unterstützt, war bei jeder der zahlreichen Strahlzeiten, sowohl bei der Planung als auch bei der Durchführung und der Diskussion der Ergebnisse, aktiv dabei. Sein großes und breites physikalisches Wissen war für mich immer beeindruckend und ist es bis heute noch. So konnte ich im Laufe der Arbeit sehr viel von ihm lernen und mein Wissen erheblich erweitern. Besonders geschätzt habe ich sein offenes Ohr für meine vielen Fragen. Die vielen Besprechungen zur Planung der Versuchsaufbauten und der Planung der Strahlzeiten und Experimente, genauso wie die Diskussionen im Anschluss über die Ergebnisse, haben viel zum erfolgreichen Abschluss der Arbeit beigetragen. Auch nach seiner Pensionierung haben wir uns oft getroffen, den Stand der Arbeit diskutiert, offene Fragen erörtert und unter anderem zwei wissenschaftliche Veröffentlichungen geschrieben. Solch eine intensive und nahe Betreuung, bei der dennoch selbstständiges Arbeiten gefördert und gefordert wird, ist außergewöhnlich und ich bin ihm sehr dankbar, dass ich diese Erfahrung machen durfte.

Als Nächstes möchte ich Dr. Jochen Wieser, meinem Mentor, danken. Auch er war bei allen Strahlzeiten dabei und das bis spät in die Nacht hinein. Beeindruckend waren seine Fähigkeiten als "lebendes Spektrometer", sein Wissen, das weit über die Physik hinaus geht und seine vielen neuen Ideen, was Experimente und Versuchsaufbauten anging. Sehr geschätzt habe ich zudem die vielen Diskussionen über physikalische und auch nicht-physikalische Themen, wodurch die langen und intensiven Strahlzeiten mitunter sehr kurzweilig wurden.

Unsere kleine Forschungsgruppe um Prof. Ulrich war angegliedert an den Lehrstuhl E15 "Experimentelle Astroteilchenphysik" und wurde von diesem unterstützt. Für diese Unterstützung, ohne welche unsere Strahlzeiten und weiteren Experimente nicht möglich gewesen wären, genauso wie für seine Führung und seinen unermüdlichen Einsatz für die Belange des Lehrstuhls, möchte ich Prof. Dr. Stefan Schönert, dem Lehrstuhlinhaber von E15, herzlich danken.

Besonderen Dank auch an Prof. Dr. Lothar Oberauer, der unserer Gruppe mit Rat und Tat zur Seite gestanden ist und immer ein offenes Ohr für unsere Anliegen hatte.

Mein Dank gilt auch den anderen Mit-Doktoranden und Studenten von E15, mit welchen ein häufiger Austausch an Ideen, Unterstützung und sonstigen Gesprächen stattfand. Toll unterstützt wurde der Lehrstuhl E15 zuerst von

Sabine Kaps und danach von Dr. Paola Mucciarelli im Sekretariat. Beide waren meine ersten Ansprechpartner bei den vielen organisatorischen Fragen und waren oft die Rettung im Kampf gegen die Bürokratie.

Sehr wichtig war mir außerdem die angenehme und produktive Atmosphäre innerhalb unserer Gruppe, zu der meine Kollegen und Vorgänger Dr. Thomas Dandl, Dr. Alexander Neumaier und Dr. Andreas Himpsl beigetragen haben. Besonders Andreas möchte ich hier hervorheben, mit dem ich die größten zeitlichen Überschneidungen hatte und der mich in die schon vorhandenen Versuchsaufbauten eingearbeitet, mich bei der Weiterentwicklung der Versuchsaufbauten unterstützt und insbesondere mich in die Welt der Vakuumtechnologie eingeführt hat. Außerdem war er bei fast allen Strahlzeiten von früh bis spät dabei und hat mich sogar während dieser Tage bei sich übernachten lassen, da mein Arbeitsweg viel weiter gewesen wäre.

Der Großteil der Versuchsaufbauten wird selbstentworfen und die Teile dazu in den Werkstätten der Institute gefertigt. Hier möchte ich Fritz Haftlmeier und Georg Obermaier aus der Werkstatt des Maier-Leibnitz-Laboratoriums, Ralf Lang und Michael Klöckner aus der E12 Werkstatt, sowie Harald Hess, Thomas Richter und den anderen Mitarbeitern der E15 Werkstatt danken. Viele Teile mussten gefertigt werden und oft war ein kurzfristiger Umbau oder eine Reparatur notwendig, damit die Strahlzeit wie geplant stattfinden konnte. Sehr häufig kam ich mit einer groben Idee in die Werkstatt und erst durch die Erfahrung der Mitarbeiter dort, wurde aus der groben Idee eine sinnvolle Lösung und dadurch ein funktionsfähiger Versuchsaufbau. Das Wissen und die Erfahrung der Werkstätten, dazu das Geschick in der Fertigung, war für mich besonders beeindruckend. Die offene und hilfsbereite Atmosphäre hat dazu geführt, dass ich immer gerne vorbeigekommen bin, wenn es wieder etwas am Versuchsaufbau zu verbessern gab.

Für Beschleunigerexperimente ist natürlich auch ein Teilchenbeschleuniger notwendig. Danken möchte ich an dieser Stelle dem Maier-Leibnitz-Laboratorium, dass wir unsere Experimente an ihrem Tandem-Van-De-Graaff-Beschleuniger durchführen durften. Dieser Teilchenbeschleuniger ist - in meinen Augen - ein ganz besonderes Stück Geschichte der Physik. Unvergessen die vielen Strahlzeitvergaben, in denen die kostbaren Strahlzeiten verteilt wurden. Es gab immer mehr Interessenten, als Zeit zur Verfügung stand. Dies ist ein untrügliches Zeichen der Wertschätzung dieses Beschleunigers durch die Kollegen der anderen Forschungsgruppen. Natürlich funktioniert so ein Beschleuniger nicht ohne die Mitarbeiter, die diesen täglich am Laufen halten. Dies fängt beim technischen Betriebsleiter

Dr. Ludwig “Luigi” Beck und beim Leiter für Arbeitssicherheit Peter Hartung an, die für die Rahmenbedingungen gesorgt hatten, damit die Experimente durchgeführt werden konnten. Unersetzlich für den Betrieb des Beschleunigers sind natürlich auch die Operatoren Michael Wiesheu, Michael Pelzer und Christian Lenz. Diese haben zusammen mit den Mitarbeitern der Werkstatt durch Wartung, Reparaturen und Instandhaltung den meist störungsfreien Betrieb erst ermöglicht. Zu Beginn der Strahlzeiten haben sie den Strahl eingestellt, und das oft unter erschwerten Bedingungen, wenn wir, wie so häufig, ganz spezielle Strahleinstellungen benötigten. Auch während der Strahlzeit wurden wir jederzeit sehr gut und sehr kompetent unterstützt. Zusätzlich zu den Operatoren erhielt ich auch viel Unterstützung mit Rat und Tat durch etliche Kollegen und weitere zahlreiche, zum Teil ehemalige, Mitarbeiter des Maier-Leibnitz-Laboratoriums. Außerdem auch durch die Sekretärin Christine Singer. Nicht zu vergessen auch das Reinigungsteam, welches immer für saubere Büros und sonstige Räume gesorgt hat. Für all die Unterstützung und das gute vertrauensvolle Arbeitsklima bin ich sehr dankbar und ich werde diese Zeit sehr gut in Erinnerung behalten.

Zum Schluss möchte ich noch meinen Eltern für ihre wunderbare Unterstützung während des gesamten Studiums und auch der Promotion danken. Dieser Rückhalt war mir immer sehr wichtig. Außerdem möchte ich auch meinen Geschwistern und Freunden für die vielen Treffen, Unternehmungen und Gespräche danken. Um erfolgreich eine solche Arbeit zu schreiben, ist es auch wichtig Abschalten zu können, seine Freizeit mit Freunden und der Familie zu genießen und auch ungezwungen die Gedanken schweifen zu lassen. Dabei kommen meistens die besten Ideen.